UNIVERSITÀ DI PARMA

UNIVERSITA' DEGLI STUDI DI PARMA

DOTTORATO DI RICERCA IN
Fisica

CICLO XXXIV

FLUORESCENCE MICROSCOPY FOR TARGETED PHOTOSENSITIZER DELIVERY SYSTEMS

Coordinatore:
Chiar.mo Prof. Stefano Carretta

Tutori:
Chiar.ma Prof. Stefania Abbruzzetti
Chiar.mo Dr. Paolo Bianchini

Dottoranda: Eleonora Uriati

Anni Accademici 2018/2019 – 2020/2021

Ad Artemi e Marco

Abstract

This thesis aims to investigate the design of different delivery systems for the effective transport of photosensitizers towards a variety of biological targets and their potential applications in photodynamic therapy. The introduction of complexes endowed with targeting capabilities is crucial to effectively direct the cytotoxic activity of singlet oxygen towards the desired systems, such as bacterial or cancer cells. Within this work, proteins have been chosen as molecular scaffolds to be combined with different photosensitizers, improving the bioavailability of the latter ones by facilitating their solubility in aqueous solutions. The first protein system to be discussed is based on nitrophorin 7; its natural capability of interacting with negatively charged membranes has been exploited for the transport of hypericin to model and real biological membranes presenting an overall negative charge on the outside.

A next step in the direction of improving the flexibility of these molecular carriers is presented with the second systems studied in this project: a streptavidin-based complex has been indeed introduced as a multifunctional photosensitizing agent. The introduction of targeting capabilities via a biotinylated antibody have allowed the successful targeting of *A. aureus* bacterial cells. A preliminary attempt of using this modular approach for targeting melanoma cancer cells is also presented.

Eventually, the antiviral action of photo-activated hypericin has been investigated on SARS-CoV-2 viral particles. The biophysical studies run on this enveloped virus has led to the conclusion that hypericin would be an effective compound to be used in broad-spectrum treatments against enveloped viruses.

The research activity presented in this work was conducted in collaboration with prof. Alberto Diaspro (Università di Genova, Istituto Italiano di Tecnologia) and Dr. Paolo Bianchini (Istituto Italiano di Tecnologia).

Contents

Chapter 1

1 Introduction

Light has been known as a therapeutic agent in medicine and surgery for centuries, for the earliest known report of sunlight as a healing modality was introduced by the Greeks around 3000 years ago. Despite being a beneficial tool for the treatment of diseases such as vitiligo, psoriasis and skin cancer [1], it was not until the end of 19th century that the full potential of light was rediscovered and introduced again in medical treatments under the name of phototherapy [2]. The first one who demonstrated its medical potential was Niels R. Finsen, who was able to heal a tubercular condition of the skin known as *lupus vulgaris* via the direct use of light on his patients [3]. Thanks to his achievements, he was subsequently awarded of the Nobel Prize in Physiology or Medicine in 1903. Nowadays, phototherapy occupies a significant niche position in medicine, where one of the most active research areas involves studying the effects of light when combined with an administered molecule called photosensitizer (PS). The medical treatment involving the combination of this kind of sensitizing drugs with light is called photodynamic therapy (PDT). Two of its first modern applications took place in the beginning of 20th century. Specifically, O. Raab discovered that exposing to sunlight the unicellular organisms *Paramecium caudatum* previously treated with acridine orange could lead to its destruction, while H. von Tappeiner together with Jesionek observed that eosin, associated with exposure of white light, could have healing effects on skin tumors [4].

PDT is currently considered a promising alternative treatment modality against tumors and other non-infectious diseases, mostly because it is less invasive and it can be easily combined with other medical approaches. Moreover, the efficacy of PDT also against chronic inflammations and drug-resistant bacterial infections has drawn a renewed attention on the treatment, since another of its advantages is that it does not induce drug resistance and can therefore be introduced as an alternative method to antibiotics [5][6]. To complete this scenario, PDT is also effective in the inactivation of mammalian viruses and it has been observed that enveloped viruses are specially sensitive to the photodynamic action [7][8]. This aspect has made PDT extremely relevant again, mainly because the present Covid-

19 global pandemic, caused by the new coronavirus SARS-CoV-2, possessing a membrane, has urgently required the introduction of new methods to prevent and treat the disease [9].

The wide range of biological targets that can be addressed with PDT evidences its great versatility while, despite the differences existing among these approaches, the underlying photo-physical process of the photodynamic action remains essentially the same. The toxicity leading to cell death or deterioration of biological compartments, such as envelopes or organelles, comes from the combined photo-chemical reaction of three components: a PS, as previously mentioned, light of the proper wavelength and molecular oxygen, naturally dissolved in the physiological environment [10]. These three tools are not toxic if considered separately, but when combined they can induce toxic reaction in a biological environment. A photosensitizer is defined as a molecule capable of absorbing light with a specific wavelength. When irradiated, the PS is able to transfer the absorbed energy to a substrate molecule, oxygen in this case, eventually triggering a cascade of photophysical reactions which end up in the production of reactive oxygen species (ROS) and singlet oxygen ($^1O_2$) [5][10]. These reactive species oxidize different types of biomolecules (i.e. nucleic acids, lipids and proteins) in the very close proximity of the target of interest, causing its partial or complete destruction. The optimization of this toxic efficiency is particularly important for an effective photodynamic action [11], indeed the selective and successful damage of the structures of interest dramatically depends upon the distribution of the PS inside the physiological environment. In the case of cancer treatments, it has been observed that tumor cells exhibit significantly greater uptake and affinity for PSs than regular cells [12]. Moreover, from a diagnostic point of view, the administration of porphyrins and their derivatives has also allowed the detection of malignancies, that would be invisible if not, by exciting their red fluorescent emission [13].

The selective accumulation of a PS is crucial for the effectiveness of the therapy; however, in general terms PSs are not provided with specific targeting capabilities and possess poor solubility in watery environments. These aspects hamper the photo-toxic activity of the PS and endanger the integrity of healthy cells or normal biological compartments in the surrounding of the target. In this prospect, the choice of a suitable PS is crucial for a successful treatment as it is the selection of a molecular compound with specific targeting capabilities to assure the correct delivery of the PS. The photodynamic action is enhanced by increasing the specific

PS accumulation in the target and its bioavailability in the environment. In general, the administration of a fluorescent PS proves to be extremely advantageous as it allows to rely on both its imaging and medical properties. Nevertheless, it is not always possible to localize precisely a PS in the cell physiological environment, as it needs to possess specific photo-physical properties. Within this context, the PS called Hypericin represents a promising exception [14] as it is possible to use it in stimulated emission depletion (STED) super-resolution microscopy. On the other hand, the PS curcumin is characterized by a fluorescence emission with a remarkably short lifetime (few hundred picoseconds) [15], which makes curcumin unsuitable for STED. In this case then, the proper localization of the PS can happen only through the introduction of a fluorescent probe suitable for super-resolution.

The delivery of the photosensitizing agent has been accomplished throughout the use of different carriers, ranging from liposomal nanostructures [16]–[18] to proteins [19]–[22], including antibodies [23]. Specifically, protein-based delivery systems have proven to be useful carriers due to their biocompatibility and water solubility. Because the effectiveness of PDT heavily relays on the specific localizing capability of the PS-delivery approach, proteins appear to be interesting candidates. Indeed, specific proteins can be selected in accordance with the environment to be targeted.

Next to the design of an effective delivery system capable of transporting the PS in the area of interest, another crucial aspect regards the possibility to spatially localize the compound inside the environment under investigation. Molecular imaging-based real-time monitoring following the administration of the photosensitizing compound is particularly important to determine its selectivity and effectiveness [24]. This area of imaging presents particular challenges:

- The excitation of a photosensitizer can result not only in a cytotoxic effect, but also in the emission of fluorescence. Its activation is elicited using a wavelength in the visible range (400-700 nm), but ideally it should possess a strong absorption between 650 and 800 nm, for good tissue penetration [25]. Despite being extremely useful in diagnostic imaging, fluorescence emission is often concomitant with the photodynamic effect. More specifically, this prevents the precise localization of the photosensitizing compound in cancer cells, which deteriorate right after. From this point of view, bacterial cells are way more resistant and it has

been shown that they can endure the Hypericin-induced cytotoxic effect in STED measurements [26];

- Spatial localization of fluorescent molecules in biological samples is decisive for addressing the correct functioning of photosensitizing complexes, but it is inherently limited by the achievable spatial resolution of conventional microscopy that makes use of fluorescence [27]. In these terms, super-resolution optical microscopy represented a revolution, which branched in different directions allowing the introduction of novel microscopy techniques to resolve biological structures under 200 nm size [28]. Each nanoscopy method has specific requirements for the fluorescent dyes of choice and for the experimental conditions; therefore it has to be picked wisely.

This thesis presents a set of protein-based delivery systems provided with targeting and imaging capabilities. These compounds have been studied and characterized in *live* and *fixed* cell experiments using two different fluorescence microscopy approaches, i.e. confocal microscopy and super-resolution Stimulated Emission Depletion (STED) microscopy and Fluorescence Correlation Spectroscopy (FCS). These techniques allowed to investigate and follow the interaction of the protein carriers with their targets.

The main contribution of this work lies in the development of novel protein-based carriers possessing enhanced targeting capabilities. A step forward in the design of such types of delivery systems is the introduction of fluorescence as a tool to precisely localize these compounds in the biological environment throughout the use of advanced optical microscopy tools.

An overview about the photophysical processes at the basis of photodynamic therapy is presented in Chapter 2, before a detailed discussion about the rationale behind protein-based delivery systems and what types of protein complexes have been used in this work. To complete the chapter, a complete overview and explanation of the light microscopy techniques used within this framework is presented. The following chapters explore the different protein scaffolds of interest, with a complete description of their structure and targeting features. Each system has a dedicated chapter in which the experimental data are collected and discussed. Specifically, nitrophorin 7 (Chapter 3) is a ferri-heme protein capable of hosting a photosensitizer in its hydrophobic cavity. The system has

been labeled with a fluorescent probe suitable for super-resolution imaging and several measurements have been done in order to assess its selectivity. Then, a multifunctional carrier based on streptavidin-biotin is presented (Chapter 4); ideally, its four biotin-sites offer the advantage of having a customizable scaffold to combine targeting, imaging and treatment. Eventually, the interaction of the photosensitizer hypericin with SARS-CoV-2 particles is explored (Chapter 5). Eventually, a last chapter (Chapter 6) encompasses significant conclusions and future perspectives for this work.

Chapter 2

2 Theory and principles

2.1 Photodynamic Therapy

Photodynamic therapy (PDT) is a little invasive form of therapy used to generate a targeted cytotoxic activity toward specific biological components, such as bacteria, fungi, viruses and cancer cells. The photo-physical process underlying this method is called photodynamic effect and it relies on the combined action of three components [10]:

- A light-sensitive molecule called **photosensitizer** (PS);
- **Light** with a suitable wavelength (ranging from 400 nm to 800 nm, encompassing the visible spectrum and a portion of the near-infrared range);
- Molecular **oxygen** ($^3O_2$), naturally dissolved in the physiological environment.

In PDT, all the relevant photo-physical processes can be initiated with light of suitable wavelength (λ). The relationship between λ and its energy content *E*, is governed by the equation:

$$E = h\nu = hc/\lambda$$

Eq. 1

where *h* is Planck's constant (6.63 x 10^{-34}Js), *v* is the frequency, and *c* is the speed of light in vacuum (2.98 x 10^8 m/s). Each unit represented by *hv* is referred to as a quantum of energy (a photon) for the selected wavelength.

In general, a single quantum of light is absorbed, causing the absorbing molecule to be electronically excited. In the case of a PS, a typical energy level diagram is presented in Figure 2.1. Subsequently the absorption of a single photon, a PS is

promoted from the ground-state S_0 to a short-lived (~ns) singlet excited state, for example S_1.

From S_1, the molecule can undergo different energy pathways: it may relax back to S_0 by non-radiative decay (with consequent generation of heat) or it may emit radiation in form of fluorescence. In addition to these, the PS in the singlet excited state is likely to undergo intersystem crossing (ISC) shifting to an electronically different excited state, such it is the first triplet state T_1. This one is a relatively long-lived (~ms) state since the loss of energy by emission of light from T_1 (phosphorescence) is a spin-forbidden process, as the PS would move between two different quantum states with inverted spin [29].

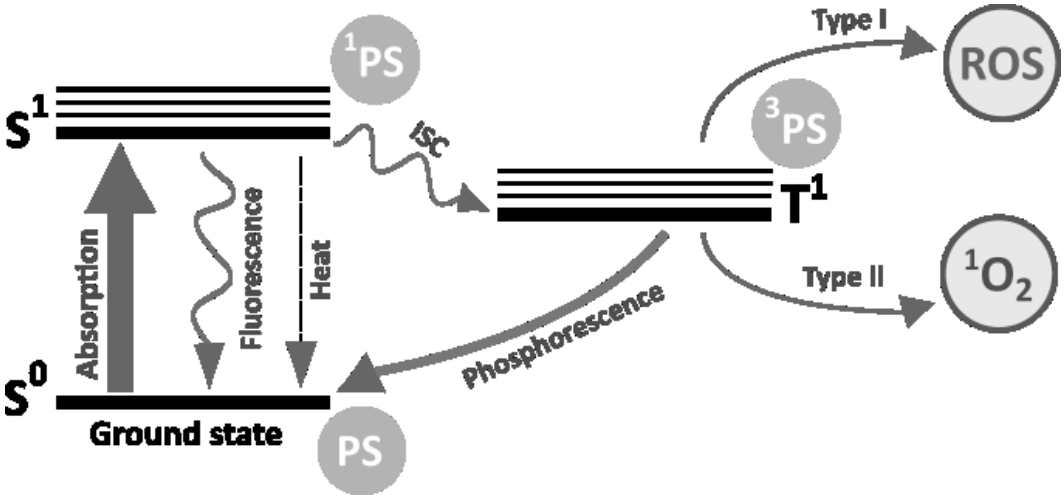

Figure 2.1: *Jablonski energy diagram showing the photochemical mechanisms of PDT. The photosensitizer (PS) absorbs a photon and is promoted to a singlet excited-state (S_1). From there, the molecule undergoes intersystem crossing moving to the triplet excited- state (T_1). From there, either Type I and/or Type II processes can occur, depending on the molecular substrate interacting with the triplet PS and resulting in the generation of reactive oxygen species (ROS) and/or singlet oxygen ($^1O_2$).*

Indeed, because of its long lifetime, T_1 often mediates reactions, that are biologically relevant, by initiating processes that give rise to reactive free radicals or by transferring its energy to the ground state oxygen molecules ($^3O_2$) to give raise to singlet oxygen ($^1O_2$) [24]. These two possible kinds of reactions are named respectively *Type I* and *Type II* (they are schematically depicted on the right side of the diagram in Figure 2.1).

In *Type I* reaction, the PS in the excited triplet state can react directly with a substrate, being it the cell membrane or a molecule, and transfer a proton or an electron therefore forming a radical anion or radical cation, respectively [29].

These radicals may subsequently interact with molecular oxygen to generate reactive oxygen species (ROS), such as hydrogen peroxide (H_2O_2) and hydroxyl radical ($HO^{\bullet}$), that may initiate a cascade of other cytotoxic reactions, provoking extensive cell damage and eventually cell death [2].

Alternatively, *Type II* reactions describe the direct interaction between the triplet PS and molecular oxygen. In this case, the PS energy is transferred directly to triplet ground-state oxygen ($^3O_2$) and it leads to the formation of excited-state singlet oxygen. This one, together with ROS generated from *Type I* reactions, are highly oxidizing agents that can directly react with several biomolecules:

- Amino acid residues in **proteins** are relevant targets of oxidative attack on proteins. Specifically cysteine, methionine, tyrosine, histidine and tryptophan are particularly susceptible to oxidative stress due to the presence of double bonds (high electron density) or sulfur moieties [30];

- **DNA** can be damaged at various levels, including nucleotides modification (among which guanine is the most susceptible to oxidation by singlet oxygen that [31]) and breakage in single strands [32];

- **Lipids** and **fatty acids** are subjects to the oxidative damage resulting from a chain reaction usually involving ROS such as the hydroxyl radical, that can cause extensive cytotoxic damage [29].

The photo-damages induced by the photosensitizing action of both mechanisms can initiate cell death. This disruptive process can take place following two different pathways [2], depending on what cell component has been affected:

- **Apoptosis** ("cell suicide"), is a form of programmed cell death following mitochondrial destabilization. It involves the intervention of crucial morphological and biochemical changes inside the cell environment, followed by the intake of the cellular remains by surrounding cells. In contrast to necrosis, apoptosis is not associated to any inflammatory response;

- **Necrosis** is a form of traumatic cell death. It is not a programmed process and it is usually a response to injurious agents such as infection, physical damages or, as in the case of PDT, excessive accumulation of ROS. In

contrast to apoptosis, it is characterized by the presence of a local inflammatory response.

Type I and *Type II* reactions can occur simultaneously and the ratio between these two kinds of processes is dependent on the photo-physical properties of the PS used and the environment in which PDT is applied (i.e. the concentration of substrates and oxygen) [29][33]. Nevertheless, even if both the pathways play a importan role in disrupting cellular mechanisms, it has been observed that *Type II* photo-oxygenation reaction predominates in the induction of cell damage [2] even though the success of a PS does not strictly depend upon it.

A key aspect is that highly-reactive oxidative action of the singlet oxygen generated through *Type II* process is effective only when $^1O_2$ is produced near the substrate biomolecules. Indeed, the lifetime of singlet oxygen is considerably short, approximately ~3.5 μs, thus limiting its disruptive radius of action to only approximately 150 nm in biological environments [34]. It is significant to point out the fact that this distance can go up to 300 nm when singlet oxygen diffuses in *in vivo* systems [35]. Therefore, PDT directly affects only molecules and structures that are proximal to the areas of PS localization, within a restricted area of hundreds of nanometers.

2.1.1 Photosensitizers in PDT

Ideally, a PS should possess a set of key characteristics which make it suitable for PDT applications. For example, the ability of selectively accumulating in diseased cells or the efficiency in generating cytotoxic species are important properties that determine the PS suitability. More specifically, the most important criteria, that good photodynamic sensitizers should adhere to, are the following [2]:

- In order to allow light deeper penetration in biological samples, a PS should have a strong absorption (i.e. high molar extinction coefficient) in the red/near infrared region (600-850 nm);

- They should possess suitable photo-physical characteristics for effective PDT applications, namely a high quantum yield of triplet formation (Φ_T), a high singlet oxygen quantum yield (Φ_Δ) and a relatively long triplet state lifetime (τ_T~μs);

- A good PS should have a very low dark toxicity and not being cytotoxic in the absence of any irradiation;

- In order to be bio-available, PSs should be soluble in biological media, allowing an easy administration followed by an effective transport to the target of interest. However, when this is not possible, suitable hydrophilic delivery systems should be established for the PS delivery.

The fulfillment of these properties is not easy to reach within a single compound: although certain PS features can be successfully modified, other aspects are not easy to control. Therefore, the design of novel photosensitizers with better properties is still matter of on-going research.

PSs are categorized in different classes, with each group possessing different properties. In general, the first distinction is made between porphyrins and nonporphyrins photosensitizers [36]. Porphyrin-derived PSs can be furtherly differentiated in first, second and third generation PSs. Porphyrin-based PSs belong to the group of tetrapyrroles, compound that possess an heterocyclic macrocycle usually containing a metallic atom. Some examples are hematoporphyrin, chlorins and phthalocyanines. Photofrin, the current benchmark for PDT, is a porphyrin-based PS as well. Second generation PSs have been subsequently developed to solve certain problems of the first generation, such as the poor chemical purity and short absorption wavelengths [37]. However, they remain quite insoluble in water. Second generation PSs combined with delivery systems such as liposomes or antibodies are referred to as third generation photosensitizers and they currently represent the most interesting ones for research studies. [38]. Nonporphyrin-based PSs are characterized by pyrrole rings variability inside macrocycles. Even if their development has lagged greatly behind that of porphyrin-based ones, nonporphyrin-based PSs (which include dyes such as methylene blue and toluidine blue) now subjected to a considerable development, providing interesting new approaches to the field of PDT.

In this work, the PSs used for the design of novel protein-based delivery systems have been Hypericin (Hyp) and Eosin-5-isothiocyanate (EITC), both nonporphyrin-derived compounds.

2.1.2 Hypericin

Hypericin (Hyp) is a, nonporphyrin-based, natural pigment deriving its name from *Hypericum Perforatum*, a genus of flowering plants in which its function might be to defend them against insects and other harmful organisms [39]. From the molecular point of view, Hyp is a quinone (inset in Figure 2.2a) characterized by a wavelength absorbance of 590 nm and a molar extinction coefficient of ~4.5 x 10^4 $M^{-1}cm^{-1}$. Hyp absorption and emission spectra are showed in Figure 2.2.

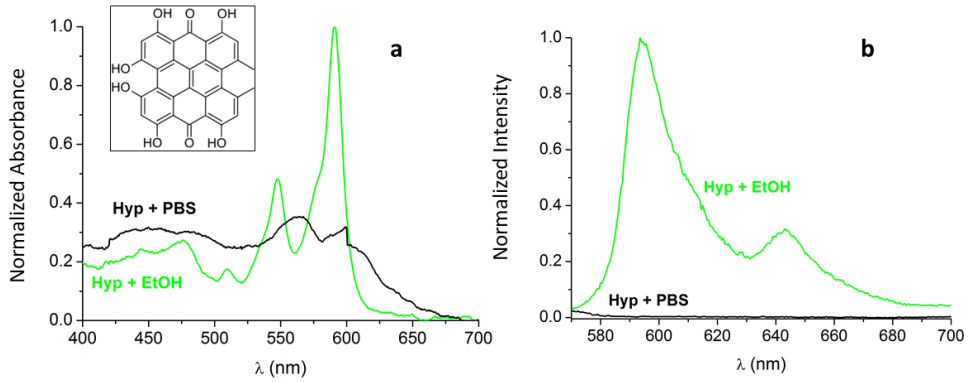

Figure 2.2: *Absorption (**a**) and fluorescence (**b**) emission spectra of Hyp in PBS (black) and ethanol (green). Chemical structure of Hyp is presented in the inset at the top left corner of (a). The fluorescence emission spectra were collected using λ_{ex} = 550 nm.*

While Hyp is insoluble in aqueous solutions, it well dissolves in organic polar solvents such as ethanol (EtOH) or DMSO (dimethyl sulfoxide): when in the latter ones, it shows a bright red color and an intense orange-red fluorescence emission, with a high fluorescence quantum yield (Φ_F ~0.35) [40]. Hyp absorption spectrum (Figure 2.2a, green) is characterized by several bands, with the peak of the lowest-energy electronic transition located at 591 nm. The fluorescence emission spectrum (Figure 2.2b, green) presents two distinct bands at 594 nm and 641 nm. These spectral well-separated bands get totally lost when Hyp is in water: in that case, the molecule tends to form inactive aggregates which dramatically impair its optical and photo-physical properties. The absorption spectrum presents broadened bands (Figure 2.2a, black), while the fluorescence emission spectrum (Figure 2.2b, black) is dominated by a broad and structureless band, which can be considered negligible. When dissolved, monomeric Hyp sensitizes singlet oxygen with high yield (Φ_Δ ~0.32). Interestingly, in aqueous solutions Hyp recovers its photo-physical properties when it binds to structures that avoid its aggregation, such as membranes. Indeed, Hyp proved to be highly advantageous in

fluorescence microscopy applications, since background fluorescence coming from aggregated Hyp in watery environments is completely absent.

2.1.3 Eosin-5-isothiocyanate

The fluorescein (FITC) derivative eosin 5-isothiocyanate (EITC) is a nonporphyrin-derived fluorescent dye with remarkable photosensitizing capabilities that can also used to selectively label amine groups on proteins. Both the absorption spectrum and the fluorescence emission one are presented in Figure 2.3.

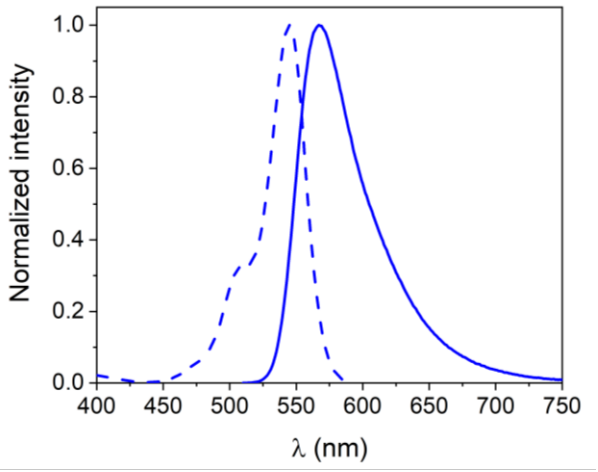

Figure 2.3: *Absorption (dotted) and fluorescence emission (solid) spectra of EITC in ethanol. Its chemical structure is showed in the top-left inset. The fluorescence emission spectra were collected using* λ_{ex} *= 500 nm.*

From a spectroscopic point of view, EITC exhibits moderate fluorescence and good photo-stability as compared to fluorescein. Its chemical structure significantly promotes dissipation of energy from the excited state molecule through intersystem crossing, a peculiarity that makes EITC great generator of singlet oxygen [41] and therefore a good candidate for PDT applications. It possesses and absorption maximum at 526 nm and a fluorescence emission maximum at 545 nm, and it presents a singlet oxygen quantum yield of Φ_Δ ~0.57 [42], with a fluorescence quantum yield of Φ_F ~0.20 in water [43].

Its efficacy as a photosensitizer has been tested in PDT works applied on different microorganisms [44][45]. As a photosensitizer, EITC is also extremely convenient because it can be easily attached to proteins through the conjugation with amine

groups. It can then easily delivered within a carrier system and subsequently activated when in proximity of the target.

2.1.4 Photosensitizing proteins

As already mentioned, the general hydrophobicity of the PSs is a significant limitation for effective applications in PDT. Low water solubility induces the formation of aggregates, hence inducing reduced PS photo-physical properties and low bio-availability in aqueous environments.

Water soluble proteins such as apomyoglobin, bovine and human serum albumins or β-lactoglobulin B (βLG) in recent works have proven to be effective carriers for natural occurring photosensitizers [46]. Specifically, these proteins offer binding sites suitable for establishing hydrophobic interaction with the PS of choice while offering a stable environment to keep it in its monomeric and therefore photoactive state (high Φ_{Δ} and Φ_{F}).

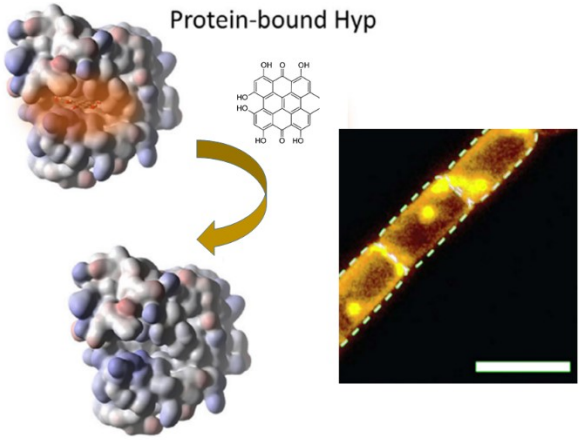

Figure 2.4: *Structural representation of apoMb interacting with Hyp. The PS is transported by the protein thanks to non covalent interactions. On the right, a STED microscopy image of* E. coli *(from [46]).The detected fluorescence signal comes from the Hyp accumulated on the bacterial walls o. Scale bar 2 µm.*

Serum albumins are known to bind a variety of endogenous molecules, including photosensitizers [26], while βLG has been suggested as a candidate for drug delivery as it is able to bind small hydrophobic ligands. In fact, the protein allows multiple PS binding sites having several potential hydrophobic clefts. Myoglobin naturally hosts a heme cofactor inside a hydrophobic cavity but, when this

cofactor is removed, the apo-protein (apoMb) is left with a cavity that can bind different hydrophobic molecules (Figure 2.4). In the context of PDT, this asset has been used to introduce Hyp in the protein cavity, to which it binds with moderate affinity [19][14]. Conversely to βLG, apoMb offers only one binding site that, however, provides an extremely favorable environment to preserve the photo-physical Hyp, since the photosensitizer is very similar to the endogenous prosthetic group (the heme) in terms of hydrophobicity, size and symmetry.

However, all these protein carriers show a weak interaction with the PSs used to assembly a photosensitizing molecule. As an example, Hyp shows dissociation constant values in the order of 1 to 10 μM [46]. Indeed, this detail could hamper the systemic administration of such types of compounds, since Hyp may translocate from the carrier scaffold to other proteins physiologically more abundant [26][47], such as serum proteins, or lipid phases of cellular membranes. Therefore, despite being effective in preserving photo-stability and bio-availability, water soluble molecules transporting PSs through non covalent interactions are likely to download the PS on non-specific cellular components for which the photosensitizing molecule shows a higher affinity. This scenario of protein-based delivery systems would be different if such types of molecular carriers had active targeted interactions with specific cellular components such as membrane receptors.

2.1.5 Targeting and imaging

The research field involved with the emergence of multifunctional nanocarriers for medical applications is known as *theranostic*, a term that defines the strategy of building molecular agents provided with both diagnostic and therapeutic capabilities. In this context, the possibility of introducing molecules with imaging properties would be a great advantage to perform in-depth studies of drug delivery and therapeutic response in the physiological environments. Besides, such multifunctional delivery systems could be furtherly endowed with targeting capabilities, assuring a specific accumulation of the therapeutic agents in the area of interest. A schematic representation of this kind of platform is presented in Figure 2.5a.

In this context, metal-based nanoparticles represent much progress, where different targeting strategies have been introduced using peptides [48], endogenous amino acids [49] or antibodies [50][51]. Intracellular imaging of these nanocarriers can be performed via de detection of the photosensitizers fluorescence, while the photodynamic effect is induced via light irradiation. Indeed, one of the advantages of using nanoparticles for targeted-PDT is that they can be easily customized, being a quite flexible surface. However, their considerably small size may present significant retention problems while their chemical compositions may introduce toxic effects in the physiological environment.

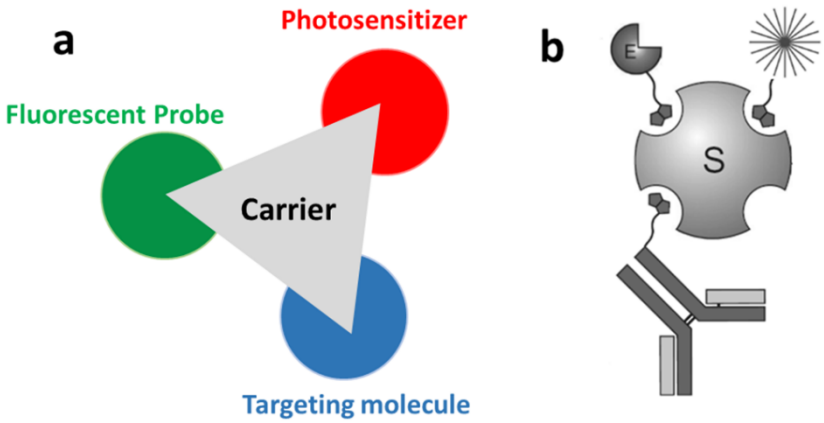

Figure 2.5: *(**a**) Schematic representation of a multi-functional carrier for targeted PDT, endowed with imaging capabilities. (**b**) Design of a multifunctional carrier based on the streptavidin-biotin complex. Special structural features of the system allow customization with different molecules, such as antibodies, fluorescent probes or others. (**b**) is taken from [107].*

Once again, proteins could be suitable building-block for the development of this type of multifunctional delivery-systems. In several studies, the fluorescence emission of photosensitizers has been used in imaging [14], [24], [26], [47] to spatially localize the compounds in the cell environment. With the aim of creating targeting PS-delivery carriers, the coordination of the latter ones with appropriate fluorescent probes suitable for advanced super-resolution optical imaging might embody a key turning-point in the development of protein-based theranostic agents. Indeed, optical microscopy nowadays represents a fundamental tool in the study and characterization of novel protein-based delivery systems within the cell environment. Fluorescence microscopy techniques such as confocal and STED (for super-resolution acquisitions) nowadays represent almost the standard for any biological and biophysical investigation, and they are herein exploited to

thoroughly investigate the behavior of the protein-based PS delivery systems previously introduced.

2.2 Fluorescence Light Microscopy

Optical microscopy encompasses all those techniques that involve the use of microscopes and visible light to generate the magnified image of an object that cannot be seen with naked eye. In order to uncover the spatial arrangement and function of all molecules inside cells, the development of microscopy tools to directly observe those interactions with high spatial and temporal resolutions have become irreplaceable resources for answering lots of biophysical and questions. In particular, fluorescence microscopy is the most popular microscopy method in the life sciences [52], mainly because of two reasons:

- Being a minimally invasive method, it allows to observe a living cell (or a living tissue or a small-sized organism) in all the three dimensions, negligibly damaging the sample;

- It can rely on the introduction of fluorescent probes that can be attached to specific proteins or biomolecules of interest, introducing an *a priori* knowledge that allows the observation of only the desired processes [53].

In such type of microscope, the fluorescence emission of a molecule can be easily separated from the excitation light (Figure 2.6a), since it exists a wavelength-shift between the two due to energy loss. The emitted light is collected via the use of a dichroic mirror (Figure 2.6b), which selectively passes light of a small range of colors while reflecting others. This shift in wavelengths makes fluorescence microscopy extremely sensitive.

The number, variety and complexity of fluorescence microscopy techniques have steadily increased over the last two decades, especially after the introduction of the super-resolution approaches that have quickly shifted the paradigm of microscopy towards the one of nanoscopy [28]. Indeed, this family of new so-called “super-resolution” optical tools allows to overcome the diffraction limit of

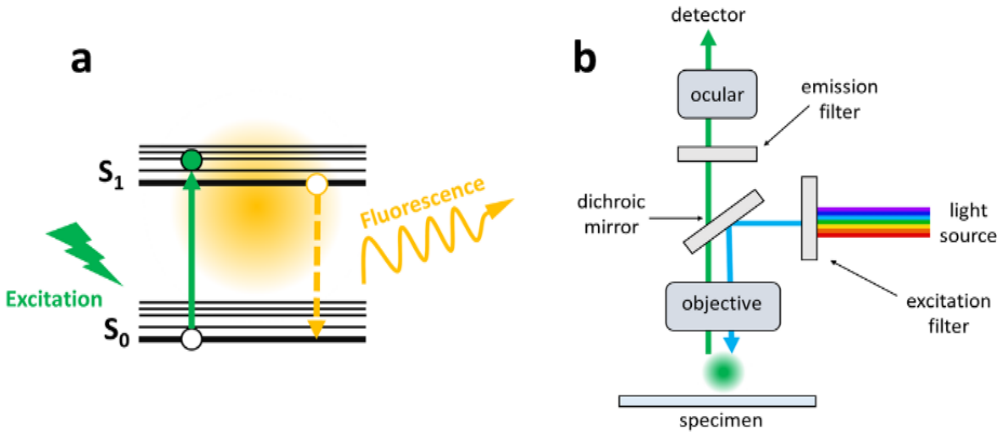

Figure 2.6: *(**a**) Schematic representation of the ground and excited state in a fluorescent molecule: when excited with light of suitable wavelength (green), the molecule absorbs a photon and it is quickly promoted to the excited state. The molecule undergoes energy loss through different vibrational states before quickly relaxing back to the ground state while concomitantly emitting a fluorescence photon of lower energy (orange). (**b**) Basic fluorescence microscopy scheme. The dichroic mirror allows to reflect the excitation light on the sample and to selectively collect the light coming from the fluorescence emission.*

light, which precludes the visualization of details below ~200 nm. With the development of nanoscopy, it is possible to resolve biological objects down to a few tens of nanometers [54].

Nowadays, the choice of a certain fluorescence microscopy technique largely depends on the particular biological question to address, being the microscopy and nanoscopy toolbox so variegated. However, current advanced methods are based on more basic setups, such as widefield or confocal microscopy. The consequent overcoming of the diffraction limit results from the successful combination of optics and chemistry [55].

2.2.1 Resolution in Optical Microscopy

The resolution (or resolving power) of an optical imaging system can be defined in easy terms as the smallest distance between two points for which both these points can be told apart [56]. Resolution's limit is deeply rooted in the physical laws that govern light diffraction; through a careful design of lenses and optics, resolution can be improved only to a certain extent. Therefore, any optical

microscope has a physically limited resolution that is generally referred to as "diffraction limit".

In a fluorescence microscope, the light comes from fluorescent molecules, which act as singlet light emitters and can be considered as point objects. In order to form an image, the fluorescence light must be collected with a lens and, according to geometrical optics; it should be possible to obtain an infinitely small point image. However, due to diffraction this is not true.

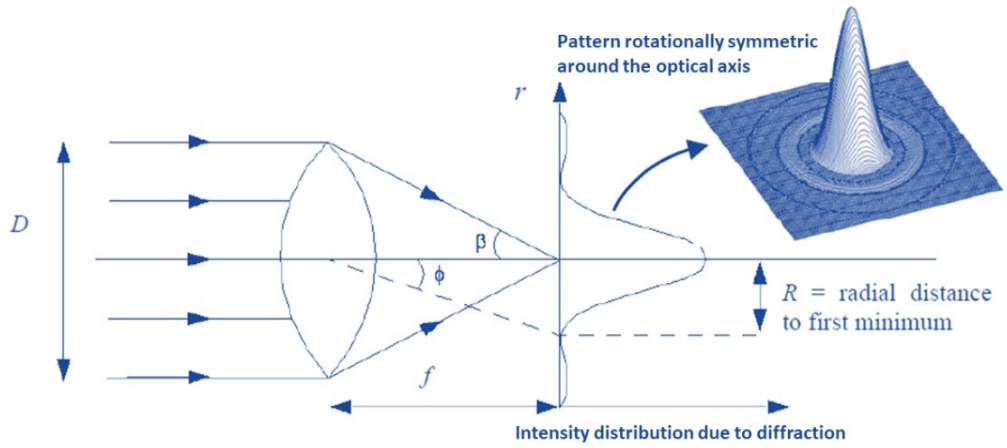

Figure 2.7: *Incoming parallel rays are focused by a convex lens into a one focal length. D indicated the lens diameter, f the focal length and β one-half of the focusing angle. In the image plane, the 2D diffraction pattern is presented; on the right upper corner, the 3D representation is also displayed. The pattern is rotationally symmetric around the optical axis.*

The image of a point-like fluorescence molecule is not a point, but an intensity distribution with a maximum on the optical axis and a number of small secondary maxima around the center, as illustrated in Figure 2.7. From a mathematical point of view, the light intensity distribution in the image plane can be described by the equation:

$$I(r) = \left(\frac{2J_1(v)}{v}\right)^2$$

Eq. 2

where J_1 is a Bessel function of the first order and v is a normalized optical coordinate. When a small angle β is assumed (Figure 2.7), the value of the optical coordinate v is given by

$$v \approx \frac{\pi D r}{\lambda f}$$

Eq. 3

where λ is the wavelength and D, f and r are defined in Figure 2.7. Hence, the intensity is function of only the radial coordinate r, meaning that the intensity pattern in the image plane is rotationally symmetric around the optical axis and it consists of a central maximum surrounded by weaker concentric rings. This pattern is called Airy disk (Figure 2.8) and it is the projected image of a single point object in a microscope.

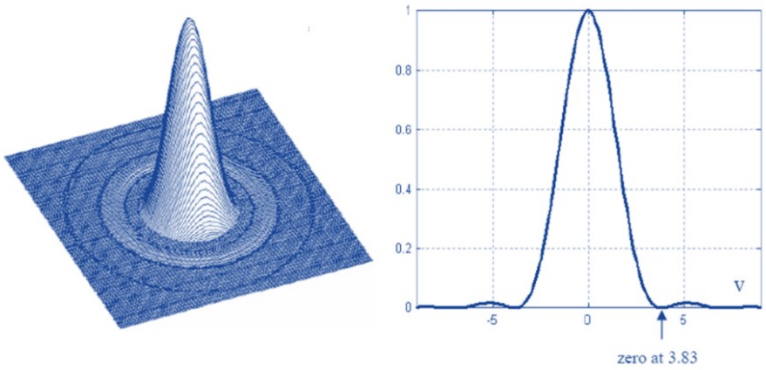

Figure 2.8: *3D representation of the Airy diffraction pattern. On the right side, the profile of the intensity maximum is presented; this peak is called Airy spot and measures 3.83 o.u. (optical units, dimensionless units of length that are used to indicates distances in terms of the numerical aperture of an objective and the wavelength of the light used for imaging).*

The 84% of light intensity is to be found in the central peak (called Airy spot), with a radius v = 3.83 in optical units (the remaining 16% is distributed in the concentric rings). This value of v corresponds to a radial distance of

$$R = 0.61 \frac{\lambda}{sin\beta}$$

Eq. 4

where β is the angle given in Figure 2.7. R corresponds to the radial distance of the first intensity minimum and to obtain a small disk it should be used a short wavelength combined with a lens with a suitable size. This intensity distribution in the image plane when reproducing a point object is called Point Spread Function (PSF) [57].

2.2.2 Rayleigh and Abbe criteria

In fluorescence microscopy, the role of the focusing lens previously introduced with Figure 2.7 can be ascribed to the objective, which is characterized by a specific numerical aperture (NA) described as

$$NA = n \cdot sin\beta$$

Eq. 5

where n is the refractive index of the immersion medium used between the objective and the coverslip protecting the specimen, while β equals one-half of the objective's opening angle (Figure 2.9a). NA literally represents the ability of a microscope objective to focus the light.

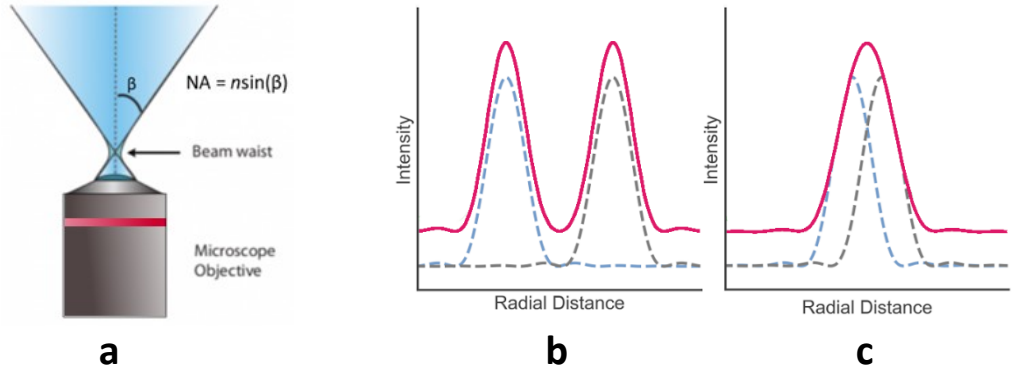

Figure 2.9: *(**a**) Illustration of the numerical aperture (NA) of a microscope objective. (**b**) and (**c**) illustrates the Rayleigh's criterion. In (**b**) the PSFs of two emitting objects are clearly separated, but when the distance between the two objects is such that the first maximum of one Airy pattern overlaps with the first minimum of the other (**c**) they are no more resolvable. As a result, the PSFs combine additively and it is no longer possible to separate the two objects.*

The two most well-known criteria for giving a reasonable estimate of resolution are the Rayleigh's criterion and the Abbe's resolution limit [58]. The first one is based on the minimum separation between the PSFs of two separate objects. When the objects (i.e. two fluorescent molecules) are brought together, their PSFs combined additively and the resulting PSF is what is imaged by the microscope (Figure 2.9b-c).

When the two objects are far apart enough, they are distinguishable and can be observed as two separate entities. In his work [59], Rayleigh defined the resolution

limit as the distance at which the central maximum of an Airy pattern of an object is overlapping with the first minimum of the Airy pattern of the second object, with this distance given as

$$d = 1.22\frac{\lambda}{NA}$$

Eq. 6

Rayleigh himself explained that his criterion does not represent a hard limit to resolution [58], indeed he based his method on the human visual system in order to provide enough contrast for an observer to distinguish two separate objects.

Conversely, Abbe's resolution limit is a well-defined transition from being resolved to being not resolved [60]. He empirically defined the resolution of a microscope in terms of the NA of the objective and wavelength of the observed light:

$$d_{x,y} = \frac{\lambda}{2NA}$$

Eq. 7

$$d_z = \frac{2\lambda}{NA^2}$$

Eq. 8

where $d_{x,y}$ is called lateral resolution and corresponds to the minimum distance in x-y, between two points, that can still be resolved. The axial resolution d_z represents the same concept but in the z-plane. Abbe's limit is based on the image of a grating of lines and it introduces the concept of cut-off frequency, beyond which certain orders of light are transmitted to through the optical system or not [58]. If the illumination angle coincides with the edge of the aperture of the objective lens, the cut-off is $2NA/\lambda$. Despite the differences in the formulation of the resolution criteria, the concept at the basis is what constitutes a sufficient level of contrast between the two imaged objects. Abbe's limit has been set in stone and remained unchallenged for hundreds of years.

2.2.3 The image of a fluorescent molecule

Given the Abbe's resolution limit for the axial and lateral dimensions, the theoretical resolution limit at the shortest practical excitation wavelength

(approximately 400 nm) is around 150 nm in the lateral dimension and approaching 400 nm in the axial dimension when focusing light with an objective having a NA of 1,40. In practical terms, the Green Fluorescent Protein (GFP), a fluorescent molecule of 27kDa size [61] with a length of roughly 4.2 nm and a diameter of about 2.4 nm [62], will result as a big blurred spot with a lateral and axial size of approximately 200 and 500 nm respectively (Figure 2.10).

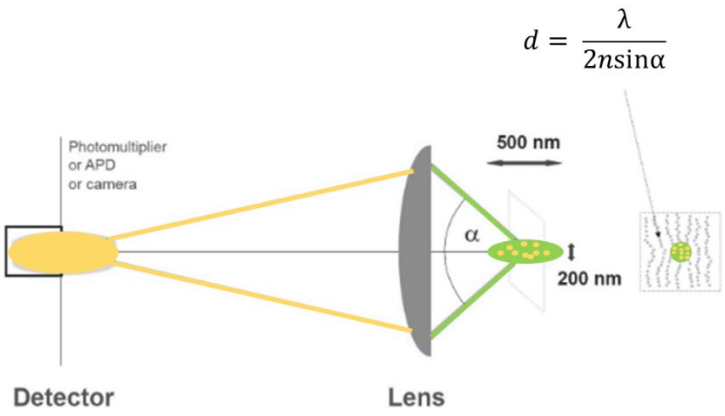

Figure 2.10: *In fluorescence microscopy, all the molecules within the region covered by the main diffraction maximum of the excitation light are concomitantly irradiated and emit fluorescence at the same time. This makes the single emitters completely indiscernible to detect. Image taken from [52].*

This means not only that GFP-like objects will have an image at least 50 times bigger than their real size, but also that fluorescent emitters closer than 200 nm are excited together, they emit together, their emissions diffract together, and are detected together. The key concept that allowed the overcoming of this limitation and the introduction of nanoscopy techniques is to render the fluorescent molecules themselves discernible at a certain time, preventing the simultaneous detection of different molecules within the same diffraction region [55].

However, before diving into super-resolution techniques (i.e. nanoscopy), it is important to start from another microscopy approach that paved the way to Nanoscopy, allowing to approach the theoretical Abbe limit in the everyday imaging: confocal microscopy.

2.3 Widefield and Confocal Microscopy

In a widefield (WF) microscope (Figure 2.11a) the entire specimen of interest is irradiated with the excitation light and the fluorescence emission is collected with a multi-point detector, either a camera or the eyes of an observer at the ocular. This way of imaging is refferred to as conventional or direct, since light coming from the sample is imaged directly by a lens [58].

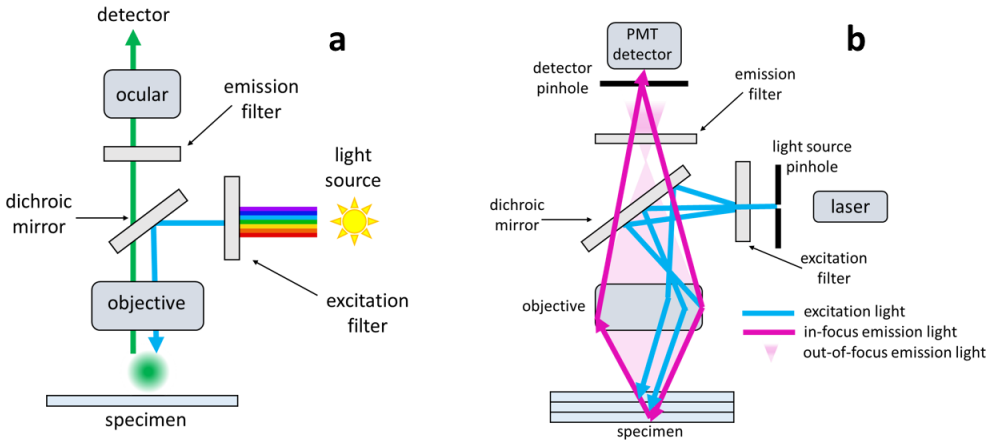

Figure 2.11: *Comparison between a widefield (**a**) and confocal setup (**b**). In the WF illumination scheme, the whole specimen volume is exposed to light. Conversely, in the confocal arrangement, light from the light-source is focused through a pinhole for illumination and subsequently into the sample, resulting in a relatively small volume. The pinhole is placed in the conjugate image plane to the focal point in the sample and it serves to reject the out-of-focus light, which does not reach the detector.*

The main advantages of a widefield arrangement is speed, since the image is directly formed on the camera or the eye. 2D images of a sample can be captured at once on the entire field of view. Therefore, it is extremely advantageous in dynamic situations in case fast temporal resolution is needed. However, WF microscopy is severely limited in terms of image contrast and spatial resolution. As mentioned above, in WF illumination the entire specimen is irradiated with the excitation light and therefore regions above and below the focal plane will also emit a detectable fluorescent signal. In the image plane, it translates in background fluorescence, which leads to an overall decrease in the signal-to-background ratio hence leading to poor contrast. The problem is particularly exacerbated for thicker samples, when the objective does not have sufficient

depth of focus. Thus, the out-of-focus light will strongly contribute to the overall reduction of the spatial resolution.

Confocal microscopy (Figure 2.11b) brings three essential developments over a conventional WF setup:

- The illumination and detection diffraction-limited foci coincide in the sample plane. Such a spot is imaged by the single-point detector [63];

- This diffracted-limited spot must be moved over the entire specimen in order to generate a complete image; it can be said that light emanating from the sample is detected instead of imaged [58];

- During confocal imaging, all the out-of-focus light is rejected and it does not contribute to the image formation, reducing the dimness observed in WF microscopy and providing optical sectioning. This improvement is possible thanks to the introduction of an illumination- and detection-side pinhole [63].

The pinhole is small and usually variable diaphragm placed at the image plane. Since it removes all the fluorescence emission not originating from the focal plane, the pinhole is also referred to as “spatial filter”. The pinhole diameter is a crucial parameter in confocal imaging: indeed, it can be used to increase or reduce the optical sectioning performance, and the lateral resolution [64]. However, changing the size of the pinhole dramatically affects also the signal-to-noise ratio of the final image, since the more closed it is, the less light will pass through it. Indeed, it exists a tradeoff between the light-collection efficiency and the resolution [63]:

- In case of a dim fluorescent signal, the pinhole can be opened to collect more light, improving the image contrast but sacrificing the optical sectioning and lateral resolution;

- Conversely, the resolution can be improved by closing the pinhole at the cost of the signal-to-noise ratio and hence image contrast.

Normally, the pinhole diameter is set in order to transmit the central maximum of the diffraction-limited pattern, i.e. the Airy disk (Figure 2.12). As already mentioned in the previous section, the size of the Airy disk depends on the wavelength λ considered, the NA of the objective and the magnification of the

internal optics of the microscope. Consequently, the optimal pinhole diameter is different for various wavelengths and for different objective lenses.

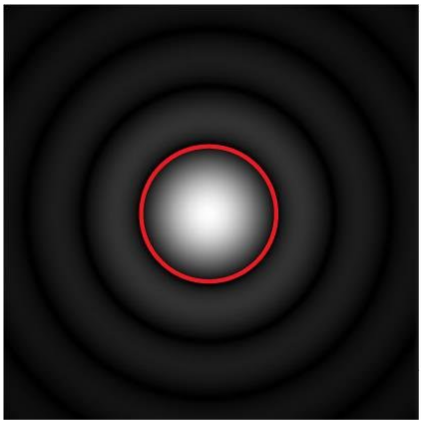

Figure 2.12: *Optimal pinhole diameter (red circle) overlapping the Airy diffraction pattern. The circle indicates a circular pinhole adjusted to 1 AU, where AU stands for "Airy Unit". When the pinhole size is increased, more and more out-of-focus contributions will be detected, reducing the resolution of the image.*

2.3.1 Fluorescence Correlation Spectroscopy

Fluorescence Correlation Spectroscopy (FCS) is an extremely valuable technique for the study and quantification of molecular dynamics. It was firstly implemented with confocal microscopy and soon became a tool for investigations in fields such as biophysics and chemistry [65]. As the name suggests, FCS is based on the analysis of time correlations in fluorescence fluctuations emitted when fluorescent molecules are diffusing in and out of a small observation volume of observation (Figure 2.13a). FCS is often performed in a confocal system (Figure 2.11b), where the observation volume is the smallest diffraction-limited spot achievable with a focused laser beam at a given pinhole size, wavelength λ and numerical aperture NA. It is important to note that in the FCS case, the beam is not scanned over the sample: the diffracted-limited spot is kept in a fixed position during all the time of the acquisition.

FCS is considered a single-molecule technique, since the continue fluctuations of the fluorescent molecules in and out the probed volume [66] can be used to determine the individual properties of one, or several, species in the sample. When a sample of fluorescently-labeled molecules is placed in the focal plane of

the confocal microscope, the intensity trace of the fluorescence emission, called intensity fluctuation *F(t)*, is collected over time (Figure 2.13b): indeed, there is a burst of emitted photons any time one of the molecules passes through the probing volume [67].

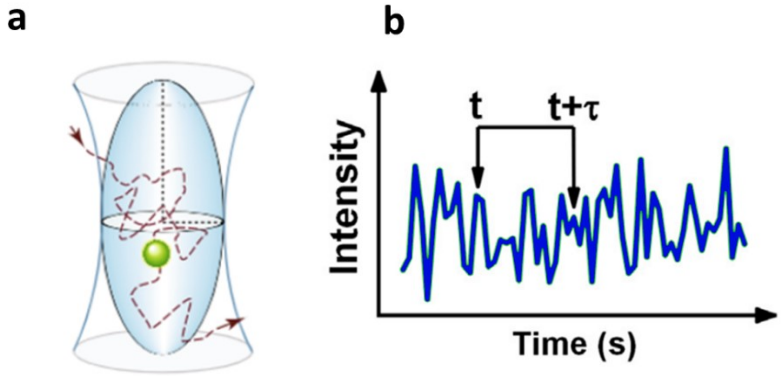

Figure 2.13: *(**a**) Detection scheme of a diffracted-limited FCS volume: molecules diffuse in and out the excitation ellipsoid, at the same time (**b**) a fluorescence intensity trace F(t) is generated collecting the signal from the observation volume in (**a**). (**a**) is from [66], (**b**) from [65].*

If the fluorophores diffuse rapidly the photon burst will be short lived; conversely, if the fluorophores diffuse more slowly, the photon burst will have a longer duration.

In FCS, the time-dependent intensity *F(t)* is analyzed statistically in order to determine the amplitude and frequency distribution of fluorescence fluctuations. More specifically, the intensity at a given time *F(t)* is compared with the intensity at a later time *F(t+τ)*. If the diffusion dynamics is slow, the two intensity values are likely to be similar. On the other hand, if the diffusion is fast, they will be quite different from each other. In short, the FCS statistical analysis consists in the calculation of the correlation between *F(t)* and *F(t+τ)* for a range of delay times τ. The result is an autocorrelation function *G(τ)* in the form of Eq. 9 that contains information on the total number of fluorescent molecules in the probed volume and their diffusion coefficient [65].

$$G(\tau) = \frac{< F(t)F(t+\tau) >}{< F(t) >^2} - 1$$

Eq. 9

Brackets $< >$ represents the temporal average. *G(τ)* is basically the measure of the self-similarity of the fluorescence intensity *F(t)* in time.

Approximating the diffracted-limited observation volume with a 3D Gaussian profile, the autocorrelation function *G(τ)* can be fitted with the three-dimensional diffusion model:

$$G(\tau) = \frac{1}{N}\left(1 + \frac{\tau}{\tau_D}\right)^{-1}\left(1 + \frac{\tau}{\tau_D}\cdot\frac{r_0^2}{z_0^2}\right)^{-1/2}$$

Eq. 10

N indicated the average number of molecules in the detection volume and τ_D is the average time of molecules diffusing through the same volume (i.e. the molecules diffusion time); r_0 and z_0 indicate the lateral and axial radial distances over which fluorescence decay by $1/e^2$ in the lateral and axial directions respectively. In a few words, they represent the lateral and axial dimension of the diffracted-limited observation volume. An example of autocorrelation curve is given in Figure 2.14.

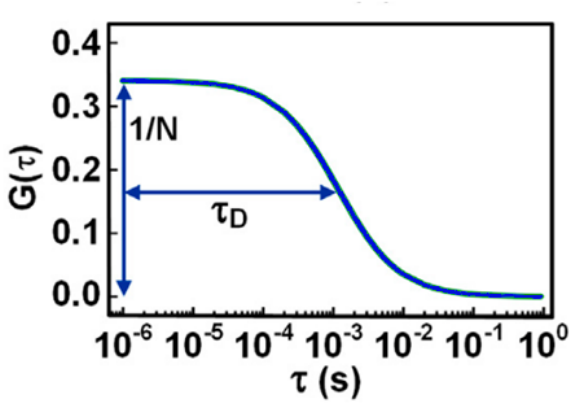

Figure 2.14: *Example of autocorrelation curve calculated with the intensity trace F(t) presented in the previous figure. N represents the number of molecules in the observation volume while τ_D is their average diffusion time. Image from [65].*

Interestingly, the amplitude of the correlation curve *G(0)* is inversely proportional to the average number of fluorescent molecules *N* in the observation volume, *G(0)* $\sim$ *1/N*. Furthermore, the width of the correlation curve $\tau_D = r_0^2/(4D)$ represents the average time a molecule diffuses in and out the waist of the diffraction-limited spot. Hence, on an equal number of freely fluorescent molecules diffusing at different speed, the slow ones will have an autocorrelation curve wider than the

one associated to the fast moving molecules. Eventually, another important parameter that can be obtained is the diffusion coefficient $D = r_0^2/(4\tau_D)$.

Nevertheless, the determination of *D* is possible only if the axial radial distance r_0 is known. Indeed, the diffusion coefficient is interlinked with the average time a molecule needs to diffuse through the confocal volume. In order to determine D it is necessary to calibrate the excitation volume of the FCS setup, i.e. the effective volume (V_{eff}) of the diffracted-limited spot.

2.3.2 The triplet state in FCS measurements

The timescale of translational diffusion for molecules going in and out the observation volume is in the range of milliseconds (ms). In addition to these phenomena, FCS curve allow also to monitor processes that take place on shorter timescales, in the range of micro (µs). Within that time window, the most common process that shows up in the auto-correlation analysis is the excitation of the triplet state. As mentioned before (Section 2.1), the triplet state is a spin-forbidden transition that takes place via intersystem crossing. The excited triplet state is characterized by a longer lifetime ($\tau_T \sim$ µs up to ms) than the excited singlet state. Since the relaxation to the ground state and the concomitant emission of a photon take longer, the triplet state is considered a "dark" state compared to the faster fluorescence emission [68].

In an FCS measurement, the abrupt transition of fluorescence molecules to the triplet state manifests in the initial part of the correlation curve, at the µs timescale. In practical terms, the molecules in the triplet state are not observed, resulting in an apparent reduction of the number of diffusing particles in the detection volume. In general, the theoretical correction for the triplet state can be complex. However, a simplification is possible if $\tau_T >> \tau_D$ and if the diffusion coefficient D does not change because of the reaction [67]. Within this approximation, the autocorrelation function G (τ) can be written as

$$G(\tau) = G_D(\tau)G_T(\tau)$$

Eq. 11

where $G_D(\tau)$, in the case of a probing volume with a 3D Gaussian profile, is expressed by Eq. 10 and it is the term due to diffusion. $G_T(\tau)$ is the additional term due to the triple state and it is given by

$$G_T(\tau) = \left[1 + \frac{T}{1-T} e^{-t/\tau_T}\right]$$

Eq. 12

where T corresponds to the population of molecules in the triplet state and τ_τ, as mentioned before, is the relaxation time for the triplet state [67].

2.3.3 FCS in case of multiple diffusing species

In certain situations, the sample under investigation is made up of two molecules that diffuse in the observation volume at different diffusion time. It could be the case for ligand labelled with a fluorescent probe and a protein that is expected to interact with the ligand. In this case, the ligand will be characterized by a diffusion coefficient D_1 and the protein bound to the ligand by D_2. If the fluorophore attached to the ligand do not undergo any change upon the protein binding, the autocorrelation function describing the two diffusing species is given by [67]

$$G(\tau) = \frac{1}{N^2}[N_1 D_1(\tau) + N_2 D_2(\tau)]$$

Eq. 13

Where N_1 and N_2 are the amount (in terms of number of molecules) of the free fluorescent ligand and the bound one ($N = N_1 + N_2$, is the total number of molecules in the detection volume). The diffusive terms $D_i(\tau)$ are given by Eq. 10, characterized by D_1 and D_2 as diffusion coefficients. Each species contributes to the autocorrelation function.

2.3.4 Calibration of the excitation volume

Significant and quantitative results obtain with FCS experiments completely rely on the size of the confocal volume (V_{conf}), which has to be determined experimentally for the chosen excitation wavelength [69]. Its determination *in situ*

is quite difficult, since it is sensitive to optical alignment and aberrations and optical saturation of the fluorescent molecules. Nevertheless, V_{conf} can be calculated from the effective volume V_{eff}; the latter one correspond to the effective experimental probe volume from which the fluorescence signal of the diffusion molecules is detected. Approximating both the volumes with a 3D Gaussian shape function, the V_{eff} is larger than V_{conf} by a factor of $2^{3/2}$:

$$V_{conf} = \left(\frac{\pi}{2}\right)^{3/2} r_0^2 z_0 = \left(\frac{1}{2}\right)^{3/2} V_{eff}$$

Eq. 14

In general, z_0 is usually expressed in terms of $z_0 = k \cdot r_0$, with k being the eccentricity of the confocal volume. In this work, the effective volume V*eff* (and therefore the confocal volume V_{conf}) has been determined by measuring the correlation amplitude of a sample of known concentration [69]. Using a sample with known concentration, it is possible to calculate the effective volume according to:

$$V_{eff} = \frac{1}{G_0 N_A c}$$

Eq. 15

G_0 corresponds to G(0), c is the sample concentration (in molar units) and N_A is the Avogadro number. This method for the determination of V_{eff} is particularly advantageous because it relies on the value of G_0 which can be extracted without doing any fitting. However, this method also assumes that certain photophysics aspects (like triple states) can be neglected.

Once V_{eff} has been determined, the correct values of r_0 and z_0 can be inserted in Eq. 10 and the FCS autocorrelation curve can be correctly fitted.

2.3.5 Confocal volume calibration using ATTO655

As previously mentioned, the triplet state manifests at microseconds time scales: since, with this method, the value of $G_0 = G(0)$ is needed for the correct evaluation of V_{eff}, (Eq. 15), the fluorescent molecule used for this calibration must possess a low, namely negligible, triplet state contribution. ATTO655 is optimal for this

purpose, due to its spectroscopic properties. Its absorption maximum is λ_{abs}= 663 nm, and its suitable for the calibration of the laser at 635 nm, used for the FCS measurements presented in Chapter 3. The determination of the confocal volume followed the theory previously described and based on the analysis of the fluorescence correlation of different samples of ATTO655 with known concentration. A stock solution of the dye was prepared dissolving ATTO655 in water, with the addition of Tween 0.05% (to prevent surface adhesion), for a final concentration of 100 nM. This stock solution was further diluted to other nine concentrations (50, 25, 10, 5, 2, 1, 0.5, 0.2 and 0.1 nM). For each concentration, a FCS measurement of 5 minutes was performed and the value of G(0) (i.e. the inverse of the number of diffusing particles <N>) was extracted directly from the autocorrelation fitting curve.

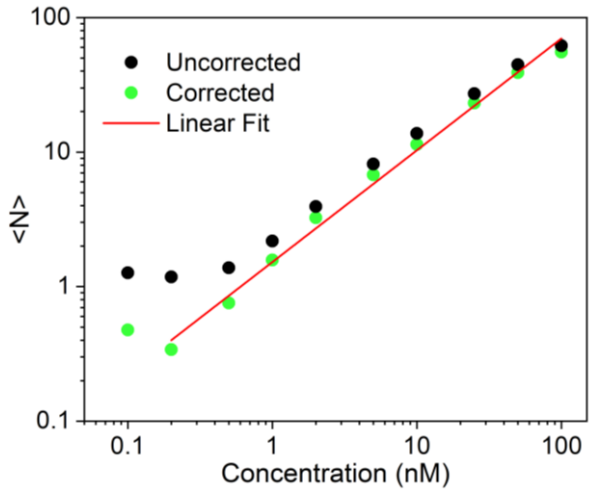

Figure 2.15: *Dilution series of ATTO655 in water and Tween (< 0.05%). The average number of particles <N> without the uncorrelated background correction is represented with black circles. The corrected values of <N> that take into account the background correction are presented as green circles. The linear fit for the latter ones is represented by the red line.*

Given the Eq. 15, $V_{eff,}$ it is evident that it exists a linear dependence between <N> (i.e. $1/G_0$) and the concentration; this means that the effective volume can be interpreted as the slope of this dependency. The obtained <N> value for each ATTO655 concentration is presented in Figure 2.15, black circles (a logarithmic scale is used for both axis).

Interestingly, <N> decreases with decreasing concentrations only in the range of larger concentration values. Indeed, when the concentration is approximately below 1 nM, this trend changes and <N> starts increasing again. This behavior is

due to the contribution of the uncorrelated background signal, which becomes increasingly prominent when the sample concentration becomes lower. Therefore, a correction of these values (black circles) is needed [69]. The effect of the uncorrelated background signal can be taken in consideration via the introduction of the correctional factor χ^2, given by

$$\frac{1}{\chi^2} = \frac{1}{(1 + < b > / < f >)^2}$$

Eq. 16

where $< \mathrm{b} >$ is the average background count rate measured from a sample containing only solvent and $< f >$ is calculated as $< f > = < F > - < b >$, with $< F >$ representing the count rate measured for each concentration value. For both $< \mathrm{b} >$ and $< F >$, the corresponding count rate was obtained from the average of the two FCS detectors count rates. Once the influence of the uncorrelated background is taken in consideration, the average number of particles in the observation volume can be corrected as follow:

$$< N > = \frac{1}{\chi^2 G_0}$$

Eq. 17

The so corrected values of <N> are also represented in Figure 2.15 (green circles), and can now be considered for the linear regression of Eq. 15 (red line in Figure 2.15). The value obtained for V_{eff} via the linear regression is 1.40 ± 0.04 femtoliters. This value represents the effective confocal volume thorough which the molecules diffuses while emitting a fluorescence signal. This V_{eff} can then be inserted as a parameter at the moment of the FCS curves fitting.

2.4 Super-resolution Microscopy

As mentioned before, the resolution limit of light has lied unchallenged since its very first formulation and before the advent of super-resolution microscopy, it seemed impossible to surpass. However, the physical principles for overcoming this limitation were discovered in the 1990s [70], but it was only in the last two decade that the diffraction barrier has been overcome, marking the advent of

nanoscopy. Nowadays, nanoscopy is a mature field that encompasses different imaging techniques.

As explained in the previous section, the concomitant excitation and fluorescent emission of the molecules inside the sample make impossible their distinction within a volume of 200 nm in size and 500 nm in length. The fluorescence signals arrive at the same time on the detector, resulting in a blurred image. The key nanoscopy concept is preventing different molecules within the same diffraction-limited spot from being detected all together [55]. The "trick" resides in the photochemical properties of the fluorescent probes, since the goal is to make fluorophores transiently assume different states and to separate them in the time and spatial dimension [52].

The fluorophores used in super-resolution microscopy applications usually possess molecular *on* and *off* states, in which the molecules differ in their ability to emit light, alternating between a fluorescent and a dark state. One of the first implemented methods was based on the Stimulated Emission Depletion (STED) concept [70], which quickly matured into the homonymous technique that nowadays still allows the study of sub-cellular components.

2.4.1 STED nanoscopy

STED nanoscopy falls under the family of coordinate-targeted techniques: in this subset of super-resolution microscopy approaches, the molecular transition between the *on* and the *off* state is induced at precisely defined positions in the sample [71]. In order to reach this purpose, such types of techniques apply a pattern of light with intensity zeros, which pushes all the fluorescent molecules briefly to one of the two molecular states except for those emitters in the periphery of such pattern. In the case of STED, the molecular transition of choice is the stimulated depletion of the fluorescent state: the *on* (fluorescent) state is depopulated, with the electrons forced to go back to the *off* (dark) ground state (Figure 2.16a) [72].

The excitation of the molecules from the dark state S_0 to the first excited singlet state S_1 ($S_0 \rightarrow S_1$) makes them fluorescent, but the application of another beam with longer wavelength (called STED beam) on the same area switches the dyes ff ($S_1 \rightarrow S_0$).

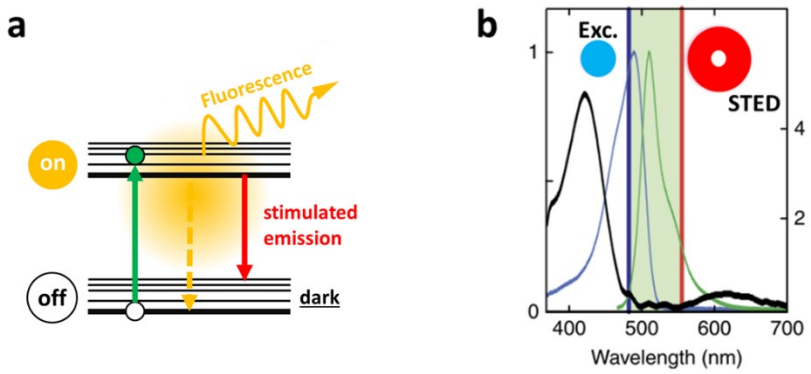

Figure 2.16: *(**a**) Energy diagram summarizing the stimulated emission process. A fluorescent molecule is excited to the "on" fluorescent state; immediately after, red-shifted light is shone on the molecule, which is depleted and pushed back to the "off" ground state. (**b**) Visualization of the spectral shift between the excitation beam (cyan) and the STED beam (red). The last one lies at the tail of the fluorescence emission (green). (**b**) is from [72].*

In its most typical microscopy implementation, the STED beam is doughnut-shaped and it presents a zero-intensity minimum right in the middle. The STED beam stimulates the emission of the fluorescent molecules while concomitantly pushing them back to the ground state: in this way, emitters located at the periphery of the intensity minimum are quenched and the only fluorescence signal detected is the one coming from the sub-diffracted center of the doughnut. In order to efficiently deplete the molecules in the fluorescent state, the wavelength of the STED beam should be red-shifted to the tail of the fluorophores emission spectrum (Figure 2.16b).

2.4.2 Resolution in STED nanoscopy

A typical STED microscope is very similar to a confocal one [27], but it needs at least two co-aligned laser beams: one for exciting the fluorescent molecules and a second one to stimulate their emission (Figure 2.17). The two overlapped beams are raster scanned all over the sample and the image is built as in a conventional point-scanning system (Figure 2.18). The resolution improvement is directly linked to the saturation on the stimulated emission process that depletes the excited state: the key principle is to shrink the diffracted-limited fluorescence spot within the zero-intensity point of the doughnut pattern.

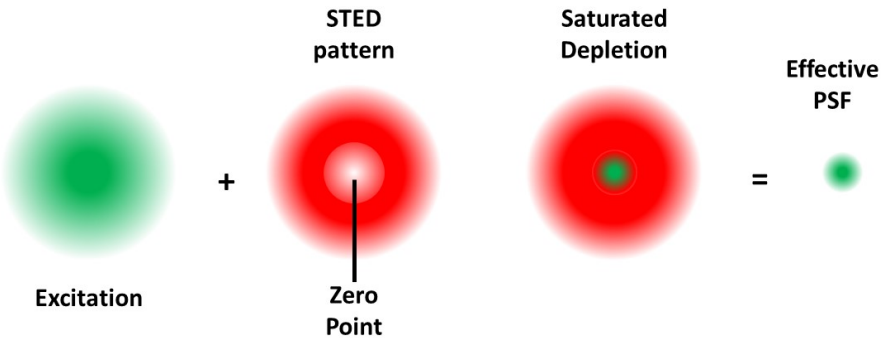

Figure 2.17: *Visual representation of the overlapping between the diffracted-limited fluorescent volume (green) and the doughnut-shaped STED beam (red). The depletion beam presents a zero-intensity point in the center; all the fluorophores in the periphery of the center are quenched, and the only detected fluorescence is the one coming from the sub-diffracted, shrunk fluorescent volume at the center of the doughnut.*

In this way, fluorescence is sharply confined into a sub-diffracted region with a diameter *d:*

$$d \ll \frac{\lambda}{2NA}$$

Eq. 18

The right side of Eq. 18 corresponds to the Abbe's resolution limit in the lateral plane (Eq. 7). Within *d*, the molecules are on.The separation of the *on* and *off* state by means of a modulated light pattern *I(x)* with a zero-intensity in a specific position allows the reformulation of the Abbe's resolution limit as

$$d \approx \frac{\lambda}{2NA\sqrt{1 + I/I_{sat}}}$$

Eq. 19

where *I* represents the maximum intensity of the STED beam. I_{sat} represents the saturation intensity of the specific fluorophore in use and it represents the intensity required by the STED beam to quench 50% of the spontaneous fluorescence emission. The scheme of a typical STED setup is displayed in Figure 2.19a. As already mentioned, the spatial profile of the STED beam has to feature a zero-intensity point at its center. To achieve such type of pattern in the lateral plane, the most used approach involves the use of a vortex phase plate [73].

It is extremely important to stress the fact that in this case, the shrinkage of the fluorescence diffracted-limited volume and the consequent improvement in resolution happen only in the x-y dimensions of the focal plane.

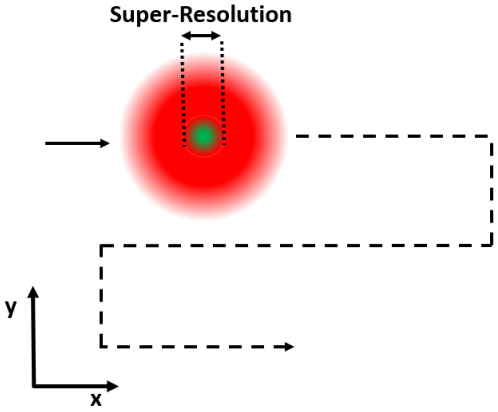

Figure 2.18: *Visual representation of the emission and STED beam line profiles. The two beams are overlapped and scanned all over the sample.*

If the resolution improvement is required along the z direction, then a bottle depletion profile made with an axial phase plate [74] is necessary. The mentioned profile of the STED beam are presented in Figure 2.19b. Generally, combining both profiles gives access to much more flexibility in terms of customization of the axial and lateral resolution.

Besides the widespread applications of one color STED, a step forward in the development of such techniques is definitely the possibility of detecting a second fluorophore. The approach is named multicolor STED imaging and it is a well spread, for it is relatively simple to implement. In the case of only one STED beam at disposal, the two-color STED approach can be reached by adding a second excitation beam and choosing the fluorescent molecules so that they do not possess the same excitation spectrum but a similar emission tail [75]. Indeed, in this case, the same STED beam could be used for both. Another approach for multicolor STED demands the combination of two excitation beams and two STED beams. In this case, it is possible to select the fluorophores more suitable for each depletion beam implemented [76]–[78]. An example of two-color STED image is provided in Figure 2.20.

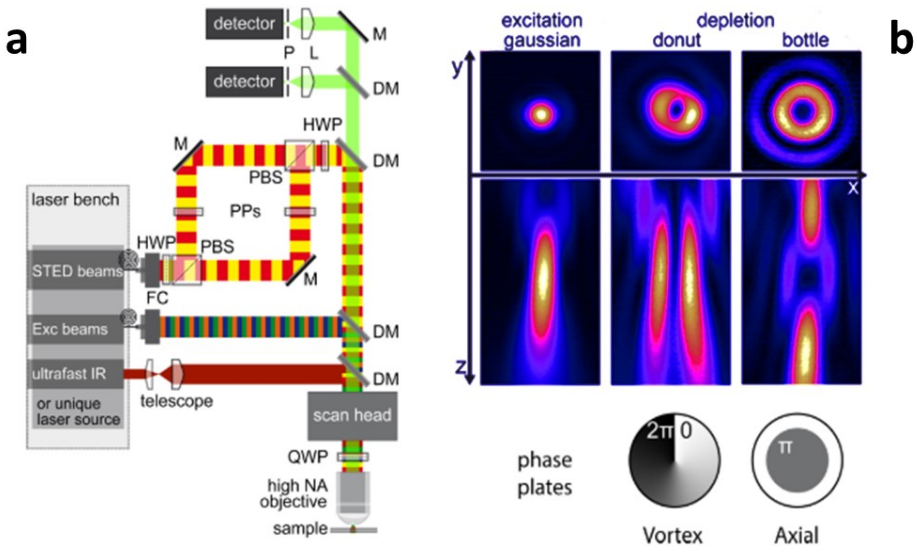

Figure 2.19: *(**a**) Scheme of a generalized STED set-up for achieving super-resolution along the latera and axial directions. Several laser beams are shown for taking into account also the multi-color STED setup and point out the possible combinations. A polarizing beam splitters separate the STED laser into two different paths, each one for a phase plate. This approach allows to evenly distribute the laser power on the two profiles and to adjust the resolution to the need. (**b**) Beam profiles as they appear at the focal plane and the respective phase plates. Figure from [27]. (*Exc *excitatory,* IR *infrared,* NA *numerical aperture,* HWP *half wave plate,* QWP *quarter wave plate,* PBS *polarizing beam splitter,* PPs *phase plates,* M *mirror*¸ DM *dichroic mirror,* L *lens,* P *pinhole).*

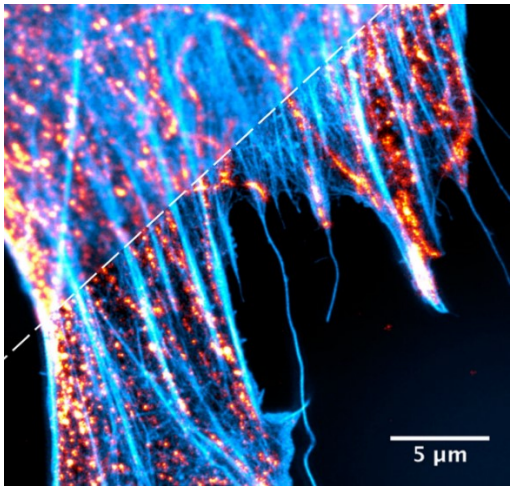

Figure 2.20*: Example of confocal (top left) and STED (bottom right) multicolor images. The sample is a 3T3 cell in which actin filaments have been labelled with Alexa Fluor 488 phalloidin (cyan) and tubulin with Abberiror Star 635p (red). Image from [27].*

2.4.3 STED by continuous-wave lasers and time-gated approach

In general, the typical implementation of a STED set-up involves the use of pulsed excitation and depletion beams [74]. The reason lies in the fact that, as explained in the previous section, a great flux of photons within a very short time-window (1-5 ns) is needed to efficiently quench the fluorophores in the fluorescent excited state, before their emission happens. Within this configuration, the STED pulse follows the excitation pulse immediately, where the depletion pulse should be shorter than the fluorescence lifetime of the fluorophore of choice (< 250 ps).

However, it has been demonstrated that STED nanoscopy can be implemented also using a continuous-wave (CW) laser as the depletion beam [79]. This arrangement is less complex to implement, since no pulse scheme elaboration is needed) and it expands the versatility of the microscope, since CW lasers provide any wavelength in both the visible and IR region [27]. The limitation with the CW laser is given by the lower peak intensity reached by the STED beam compared to the pulsed implementation. This drawback can be overcome via the introduction of a time-gated detection scheme, in the implementation called gated CW-STED (gCW-STED) and that is based on the detection of fluorescence after a certain time T_g (time delay between fluorescence excitation and collection) from the excitation event. This detection approach is based on the evidence that the probability of not detecting a fluorescent molecule increases if the fluorescence signal is collected after a certain delay from the excitation moment [27].

The proper inhibition of fluorescence through stimulated emission is dependent on the number of stimulating photons shone on the molecules in the fluorescent excited state. The detection of the fluorescence photons after a time $>T_g$ from their excitation ensures that the collected fluorescence signal comes from those fluorophores that have resided in the excited-state for at least a time interval $>T_g$ and have been exposed to the STED beam at least for the same amount of time. Basically, this implementation allows to discard early fluorescence photons ($< T_g$). In practical terms, the longer T_g the bigger is the guarantee that the fluorescence collected comes mainly from the fluorescent molecules located in the zero-intensity center of the doughnut beam. In this STED implementation, signal-to-noise ratio may suffer a bit from the introduction of T_g, since the imposition of this time interval is basically cutting out photons, imposing a limit in the choice of this time delay. However, different solutions have been successfully implemented to push this limit forward [80] [81].

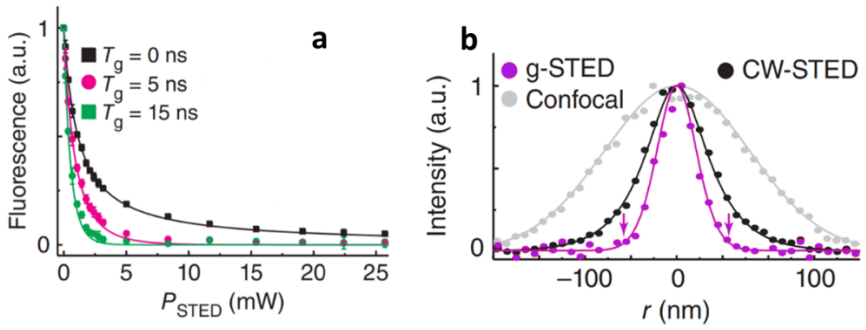

Figure 2.21: *(**a**) Normalized fluorescence detected from a fluorescent nitrogen vacancy color center in diamond, as a function of the STED laser power P_{STED} at different time gates T_g. (**b**) Comparison between normalized intensity profiles for the same structure in (**a**) . Images from [80].*

In terms of other drawbacks, the main limitations of STED microscopy is related to the high laser powers needed to efficiently switch off the excited molecules. In order to make the process $S_1 \rightarrow S_0$ statistical relevant, a large number of depletion photons must be shone on the sample. A typical I_{sat} for a fluorescent molecule is $\sim 10^4$ kW/cm^2, meaning that the average STED beam laser power is in the order of $\sim$ MW-GW/cm^2. Such high laser power may induce photo-toxic effect in living cell experiments and could induce extensive photo-bleaching. However, in the past decade the development of resistant fluorescent probe has come a long way, improving the image quality of STED images. In general, STED is still considered one of the super-resolution technique of choice for investigating molecular details in the range of 20-40 nm. Fast scanning, optical sectioning and the possibility of performing multi-color experiment set this nanoscopy approach one of the best choice.

Chapter 3

3 Nitrophorin 7

In recent years, the growing of multidrug resistance among bacteria with pathogenic activities has spread worldwide. The main causes are the prolonged use and misuse of antibiotics in the agriculture, the hospitals and the community in general, where antimicrobial resistance (AMR) has supported the selection pressure that provided a thriving environment for mutated strains, much more difficult to treat [82]. Between the 1930s and the 1960s, scientists have given rise to many antibiotics at a pace that could not be maintained for long, because of the emergence of resistant pathogens [83].

Nowadays, AMR poses a global threat to governments that eventually will bear its cost, unless coordinated action is not taken. With the available antibiotics becoming less effective and the risk of treatments becoming higher, a report on AMR envisions that up to 10 million people could die each year by 2050, at a total economic cost of 100 trillion USD [6]. Together with regulations for limiting the indiscriminate use of antibiotics, different investigations of novel, alternative treatments are today in the spotlight [84]. In fact, the development of methods that do not rely on antibiotics or detergents are of enormous interest because no AMR can arise from them.

An alternative and innovative approach to this problem is presented by light-activated molecules such as photosensitizers (Chapter 2, Section 2.1.1), which produce non-specific antimicrobial effects without the risk of developing any pathogenic resistance [85], circumventing conventional defense mechanisms against oxidative stress (associated to PDT). This approach goes under the name of antimicrobial photodynamic therapy (APDT) and in the recent years has gained significant attention due to its advantages for pathogen resistance and its being minimally invasive [86][87]. In general, the photosensitizer is administered to the target of interest where, after a certain incubation time, light irradiation at a specific wavelength induces the photoactivation described before. However, the low solubility and weak specificity of conventional photosensitizers against bacteria [88] encourages the exploration of new delivery systems with binding

capabilities for increasing specific cell accumulation and bioavailability, therefore enhancing the photodynamic action.

In this part of the project, a novel carrier based on the protein nitrophorin 7 (NP7) for the delivery of the photosensitizer Hyp is presented. NP7 is a protein naturally targeted to negatively charged membrane surfaces thanks to the presence of a highly positively charged cluster of lysine residues [89][90]. Since bacterial cells carry a negative charge [91][92], NP7 offers and interesting opportunity to develop a delivery system endowed with selectivity towards bacterial strains showing this feature. The hydrophobic pocket normally hosting the heme inside NP7 has served as a binding site for Hyp: the ApoNP7-Hyp complex self-assembly and its targeting properties have been tested and studied in a series of FCS measurements (Chapter 2, Section 2.3.1), where negatively charged and neutral liposomes respectively have been used as model membranes. Hyp properties on being a good photosensitizer have been already discussed (Chapter 2, Section 2.1.2). In order to provide this molecular platform not only with photosensitizing properties but also with imaging capability, NP7 has been covalently linked to the fluorescent dye Atto647N-cadaverine via a zero-length crosslinking method, a molecule suitable for super-resolution imaging experiments. The effectiveness of the labelled NP7 to establish an interaction with negatively charged membranes has subsequently been tested on liposomes using a STED microscope (Chapter 2, Section 2.4.1).

3.1 NP7 and anionic membranes

Nitrophorins (NPs) are a set of NO-carrying ferriheme-proteins which can be found in the saliva of the so-called “kissing bug” *Rhodnius prolixus*, a blood-sucking insect distributed in South and Central America and a principal vector of Chaga’s disease [93][94]. This class of proteins takes part in the storage, carrying and release of nitric oxide (NO) from the insect to the victim’s blood stream upon biting. NO is reversibly bound to the iron heme center when in the acidic saliva (pH 5-6) of the animal. After being injected into the tissue of the victim, the proteins experience a substantial pH change (∼pH 7.4) which triggers a conformational transition facilitating the rapid release of NO in the physiological environment [95]. Two of the most significant effects of NO are vasodilation and inhibition of platelet aggregation, both processes that facilitate the insect feeding

process. The NPs structure is characterized by the lipocalin fold, which is dominated by an antiparallel β-sheet closed back on itself to form a β-barrel [96].

This highly symmetrical protein structure encloses an hydrophobic cavity in which the heme cofactor is located, with the heme iron stable in the ferric form Fe(III) and coordinated to a proximal histidine residue (Figure 3.1a). In facts, the affinity of NO is reduced when interacting with the ferric iron, promoting the release of the gaseous ligand in physiological conditions [97].

NPs are individually designated with a number, from NP1 to NP7 in order of their relative abundance in the insect glands, and some of them have been expressed and characterized in detail. More interestingly, among this set the isoform NP7 presents peculiar properties. In particular, it exhibits notable differences in its primary sequence compare to NP1-NP4 structures [98]. This divergence is a direct consequence of the presence of a cluster of 27 lysine (Lys) residues (out of 185 residues) located mostly on the protein surface (Figure 3.1b), right at the side opposite of the heme pocket. This structural difference sets NP7 apart from the other members of the family, providing it with the ability to bind negatively charged phospholipids membranes with high affinity [99].

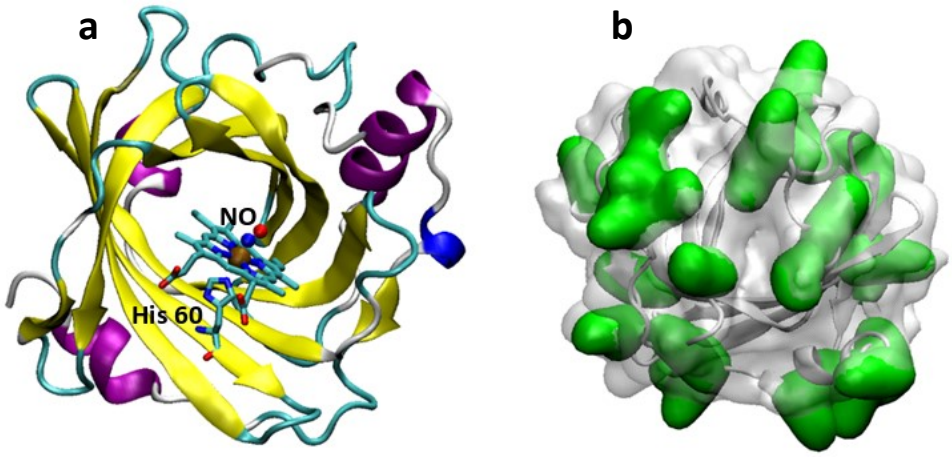

Figure 3.1: *Structural representation of NP7 relevant features. (**a**) Representation of the X-ray structure of NP7 (PDB entry 4XME) where it is shown the position of the histidine residue coordinating the heme group. The iron atom (in brown) is shown in close proximity to a NO molecule (VMD). (**b**) The surface representation of NP7 shows the lysine residues (green) located at the back of the heme cavity.*

This electrostatic feature is necessary to inhibit normal hemostasis in the insect victim. Indeed platelets, activated after the injury caused by the bite, present an overall negatively charged exterior surface that is essential for the coagulation process. Because of the presence of the Lys residues cluster, the injected NP7 is

able to target the membrane of the activated platelets. The concurrent NO release due to the change in pH then inhibits platelet aggregation, facilitating the insect feeding process. Molecular dynamics simulations of NP7 interacting with a phospholipidic bilayer (Figure 3.2) have shown [100] how the established electrostatic interaction induces the concentration of negative charge on the surface in the NP7 location. This translocation of charges is likely to have significant effects on platelets, which might not be able to establish a correct docking with other proteins related to the coagulation process. Therefore, acting as an anti-hemostatic agent, NP7 guarantees sufficient blood flow [89]. Eventually, compared to NP1, NP2 and NP4, the pH-dependent release mechanism of NO presents a higher pH-sensitivity in NP7 isoform, showing unique tuning capabilities [97].

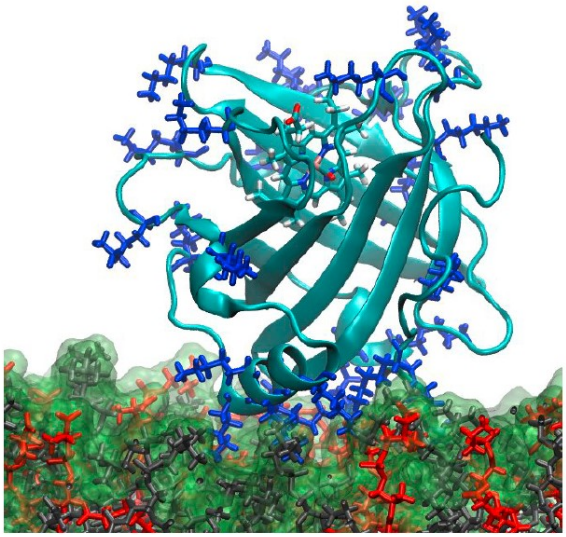

***Figure 3.2**. Molecular dynamics simulation of NP7 interacting with a phospholipidic bilayer. Lysine residues are represented in blu. Two different phospholipids, L-α-phopshatidylcholine (PC) and L-α-phosphatidyl-L-serine (PS), are shown in grey and red respectively. Image from [99].*

3.2 Physical properties of NP7

NP7 is a hemoprotein that hosts a b-type heme deep in one end of its β-barrel. Heme is made up of a porphyrin ring composed of four pyrrole subunits; in its center, the complex coordinates an iron (Fe) atom (Figure 3.3b), which is involved in reversible oxidation-reduction reactions necessary to keep or release NO in this

case specifically. In order to function, NP7 heme must be stabilized in the ferric Fe(III) state, where NO release is favorable and no other gaseous ligand (e.g. CO or O_2) can bind the iron atom. On the other hand, the ferrous Fe(II) state disfavors NO release and therefore enhances the binding of the ligand [101]. The absorption spectrum of protein NP7[Fe(III)] (Figure 3.3a) presents a Soret peak at 404 nm and also a small bump at around 640 nm due to the presence of a water molecule coordinated by the iron heme and having a hydrogen bond with the distal histidine. Only one Q-band is visible and it is located at 504 nm, typical of a five-coordinate Fe(III) [102]. This spectrum profile is distinctive of the protein when put in water [97].

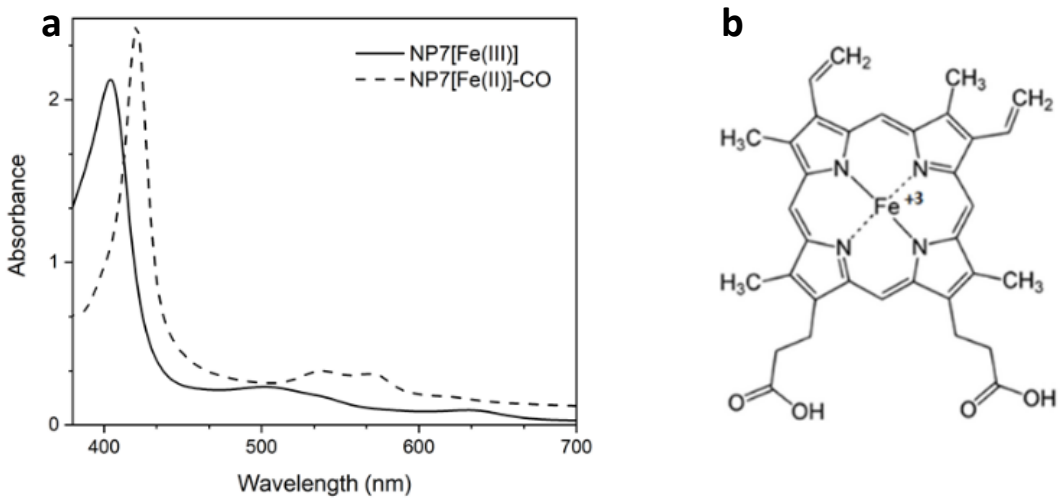

Figure 3.3: *(**a**) Optical absorption spectra of ferric (solid line) and ferrous-CO (dashed line) of NP7. The Soret band, typically found at around 402 nm in the ferric state, is shifted in the ferrous state to 421 nm. The two bands between 570 nm and 540 nm shows the coordination of the heme group with the model ligand CO. (**b**) Schematic representation of the heme group with the iron atom in the ferrous state.*

The effective binding capabilities of NP7 with a ligand can be assessed using CO as a model, since it is easier to use for studies of rebinding kinetics. The reduction from NP7[Fe(III)] to NP7[Fe(II)] can be promoted introducing the reducing agent sodium dithionite (SDT) in the protein aqueous solution. In this way, NP7 iron-heme is converted from the ferric state to the ferrous state, causing a shift from one species to the other. Once the Fe(II) species of NP7 has been obtained, the effectiveness of the CO-binding has been performed by introducing the gaseous compound with a CO laboratory air-pump. The optical absorption spectrum of NP7[Fe(II)] was acquired right after. The measurement shows a red-shift of the Soret band to 421 nm, while the same band is also narrower compared to the

Fe(III) one (Figure 3.3a). In addition to this, the effective bounding of CO is evident due to the presence of the two bands located near 570 nm and 539 nm. This spectral profile can be explained with the introduction of the sixth coordination site of the ferrous iron with the CO molecule [103], disfavoring the release of the ligand.

3.3 NP7 as a targeting PS-carrier

The self-assembly of nanostructures has been of great interest for the design of drug delivery systems with specific targeting and therapeutic capabilities. In particular, in the pursuit of creating effective carriers, water-soluble proteins have proven to be promising delivery systems mostly because of their high biocompatibility and suitability for the environment to be targeted. Such type of complexes have been studied in depth as solid platforms for the administration of the naturally occurring photosensitizer Hyp in both APDT applications [19][26][22] and PDT against cancer cells [14] (Chapter 2, Section 2.1). In this encouraging perspective, the NP7 structural property of hosting a heme group in a hydrophobic cavity makes the protein a potential delivery system for Hyp, once removed the prosthetic group and created the space to allocate inside the photosensitizing molecule. Considering also its ability to interact with negatively charged membranes, ApoNP7 is then an ideal candidate for the delivery of Hyp towards bacterial walls.

3.3.1 The ApoNP7-Hyp complex on model membranes

In NP7, the positively charged region made up of lysine residues represents a binding motif proved to be effective for negatively charged surfaces [91]. With the aim of creating a compound suitable for the delivery of the photosensitizer towards anionic membranes, the complexation of Hyp with apoNP7 (apoNP7-Hyp) has been studied in a set of experiments with FCS, fluorescence correlation spectroscopy (Chapter 2, Section 2.3.1).

It is well known that Hyp is largely insoluble in water, while it easily dissolves in organic compounds such as ethanol (EtOH) or dimethyl sulfoxide (DMSO) [40];

when dissolved, the molecule presents fluorescence emission properties (Figure 2.4) along with strong photosensitizing activity.

All these peculiarities are lost when Hyp is in water, where it tends to form aggregates and shows weak fluorescence emission, with poor photosensitizing efficiency. As mentioned before, an interesting aspect of Hyp is that spontaneously binds to superior molecular structures such as liposomes [104] and proteins through hydrophobic interactions. This binding avoids the aggregation of the molecule and it helps restoring its spectral properties (Figure 3.4).

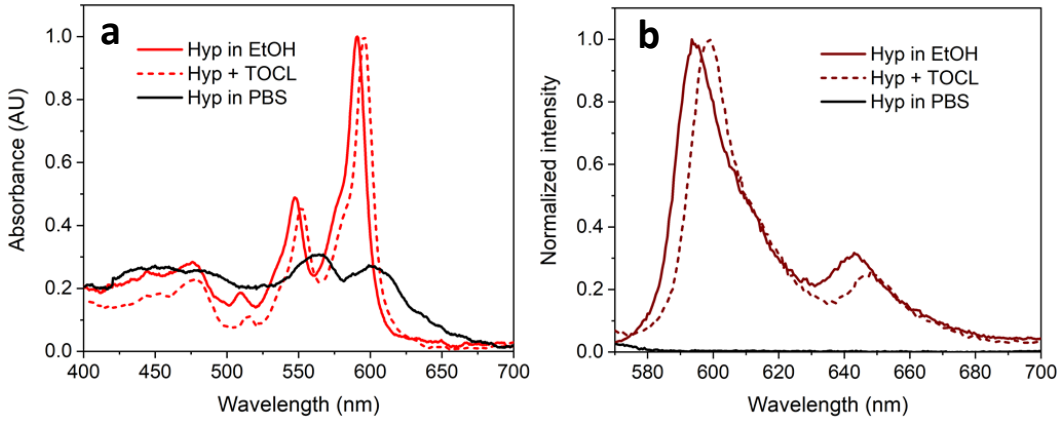

Figure 3.4: *(**a**) Normalized absorption spectra of Hyp in EtOH, in a solution of liposomes (TOCL, tetraoleyl cardiolipin) and PBS. (**a**) Normalized emission spectra of Hyp in EtOH, in liposomes and in PBS (excitation wavelength 550 nm).*

The fluorescence signal of Hyp can therefore be exploited in FCS experiments to determine the diffusion kinetics of molecular structures Hyp binds to. From this point of view, FCS offers valuable insights on the diffusion behavior and absolute concentration of the fluorescent particles present in its observation volume. In this work, the specificity of apoNP7-Hyp complex for negatively charged membranes has been tested using this technique. The model membranes chosen for assessing the effective selectivity of apoNP7-Hyp were liposomes, separately made up with two different types of phospholipids:

- Phosphatidylcholine (POPC), a neutral phospholipid with no overall electrical charge (0) and largely used for mimicking the cell membrane;

- Tetraoleyl cardiolipin (TOCL), a phospholipid carrying two (-2) negative charges. It is an important component of the inner mitochondrial membrane and it is also found in the membranes of most bacteria.

In general, liposomes are possess a spherical shape and their sizes can range from tens of nanometers to several micrometers.

A set of three different experiments have been run for each type of liposomes:

1. **ApoNP7-Hyp** (complex alone): ApoNP7-Hyp diffusion has been studied in a PBS buffer solution without the addition of any lipid substrate;

2. **Hyp + liposomes** (None apoNP7): liposomes (negatively charged and neutral ones) with the addition of Hyp in solution have been studied in two distinguished sets of experiments. Measurements have been helpful also to assess the dimension of the diffusing liposomes using the Stokes-Einstein raidus equation (Eq. 15);

3. **ApoNp7-Hyp + liposomes**: apoNP7-Hyp has been studied and characterized in solution with both negatively charged and neutral liposomes. This last kind of experiments has led to significant conclusions on the effective selectivity of the PS carrier towards only one of the two types of lipid bilayer (e.g. the negatively charged one).

Experimental results and corresponding fitting functions are shown in Figure 3.5.

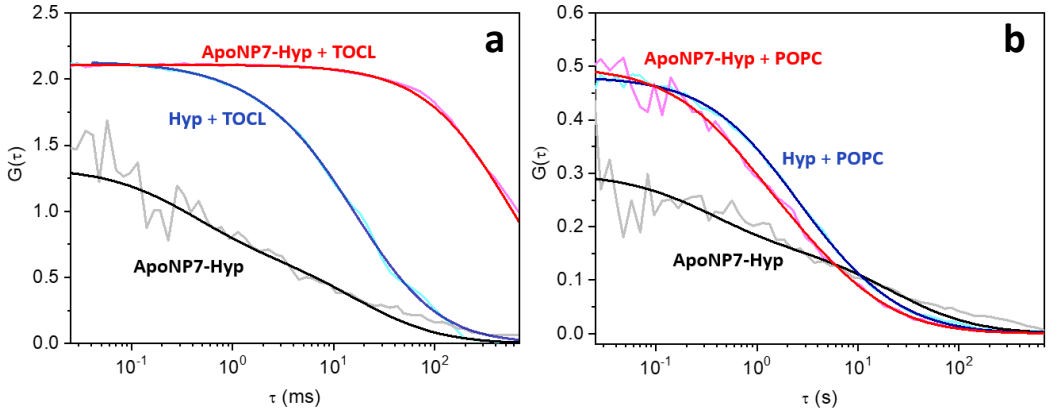

Figure 3.5: *Not normalized FCS measurements performed using apoNP7-Hyp alone and together with two types of liposomes: (**a**) negatively charged, TOCL and (**b**) neutral, POPC. In each case, the autocorrelation function G(τ) is plotted with the corresponding fitting curve. I both (**a**) and (**b**) the Hyp fluorescence emission has been used for the FCS fluctuation intensity trace. A visual inspection of (**a**) and (**b**) allows to appreciate the selectivity of apoNP7-Hyp toward anionic liposomes, since a remarkable increase of τ_D in the case of TOCL (**a**) is distinguishable.*

Diffusion coefficients calculated from each G(τ) are shown in Table 3.1, while results are discussed below for each case of study.

TOCL			POPC		
	D_1	D_2		D_1	D_2
ApoNP7-Hyp (alone)	90 ± 22	1.9 ± 0.5	ApoNP7-Hyp (alone)	100 ± 25	1.5 ± 0.4
Hyp + TOCL	29 ± 7	2.1 ± 0.5	Hyp + POPC	17.2 ± 4.3	2.5 ± 0.6
ApoNP7-Hyp + TOCL	0.06 ± 0.02	-	ApoNP7-Hyp + POPC	100 ± 23	11 ± 3

Diffusion coefficients units: $\mu m^2/s$

Table 3.1: *Diffusion coefficient values calculated from G(τ) curves: cells are color-coded in accordance with the legend in Figure 3.5.*

- **ApoNP7-Hyp (without liposomes)**
  The typical diffusion coefficient for a protein of ~20 kDa size like NP7 is roughly ~80 $\mu m^2/s$ [105]. The data analysis run for the FCS measurements from Figure 2.5 display the existence of a diffusion coefficient D_1 within a compatible range, slightly bigger than expected. However, the values obtained can be considered reliable. The introduction of a second diffusing species in the fitting model (D_2) was based on the observation that few aggregates might have been present in the sample under investigation. However, it is clear by looking at the FCS curves and considering the width

of *G(τ)* that apoNP7-Hyp nicely reflects the behavior of a freely diffusing small protein.

- **Hyp + liposomes**
  The spontaneous interaction of Hyp with lipid bilayers through hydrophobic interaction previously shown in Figure 2.4 is confirmed in FCS experiments. Upon binding, Hyp fluorescence emission is restored. The diffusion coefficients in both cases represent the diffusion kinetics of freely diffusing liposomes in solution. Also in this case, the inclusion of a second species D_2 in the fitting model allows the distinction of larger species that, both in TOCL and POPC, still does not sensibly affect τ_D. Conversely, D_1 values (29 ± 7 and 17 ± 4 $\mu m^2/s$ for TOCL and POPC respectively) show the existence of diffusing objects with a size of about 10 nm. A reliable estimate of liposomes dimension using Stokes-Einstein equation is presented later on.

- **ApoNP7-Hyp + liposomes**
  The selective interaction of apoNP7-Hyp with negatively charged liposomes becomes evident when looking at the FCS curves collected in presence of TOCL and POPC liposomes respectively. In the case of POPC liposomes with apoNP7-Hyp, D_1 (100 ± 23 $\mu m^2/s$) is comparable with the diffusion coefficient of apoNP7-Hyp alone (100 ± 25 $\mu m^2/s$). On the other hand, the protein complex with TOCL shows a completely different diffusion kinetics clearly visible in Figure 3.5a: in this case, the dynamics is predominated by a single, big, diffusive species with a D_1 of 0.06 ± 0.02 $\mu m^2/s$. The remarkable difference between D_1 in the case of TOCL liposomes with Hyp and D_1 in the case of the same liposomes with apoNP7-Hyp might be explained with the membrane instability due to the electrostatic interaction of the complex with TOCL liposomes. This could induce the formation of big aggregates in the volume of investigation.

In conclusion, the FCS experiments run on different types of liposomes prove the existence of NP7 targeting properties towards anionic membranes.

3.3.2 Stokes-Einstein radius

One way to characterize the size of liposomes freely diffusing in a solution is determining the Stokes-Einstein radius, also called hydrodynamic radius R_H. Assuming liposomes being spherical objects diffusing through a viscous liquid characterized by a certain dynamic viscosity η and a diffusion coefficient D, their radius can be calculated via the equation:

$$R_H = \frac{k_b T}{6\pi\eta D}$$

Eq. 20

where k_B is the Boltzmann constant and T the absolute temperature. The radii corresponding to each D_1 value from the FCS experiments (Table 3.1) have been calculated and presented in Table 3.2.

The radius obtained for apoNP7 alone (Table 3.2, grey) is in accordance with the expected value for a protein with the same size of apoNP7 (~2 nm) [106]. As expected from the FCS measurements with TOCL liposomes (Figure 3.5a), the interaction of apoNP7-Hyp with the lipid bilayers leads to the formation of big complexes with a size of several nanometers.

TOCL

	R_H (nm)
ApoNP7-Hyp (alone)	2.3 ± 0.6
Hyp + TOCL	7.1 ± 1.8
ApoNP7-Hyp + TOCL	342 ± 10

POPC

	R_H (nm)
ApoNP7-Hyp (alone)	2.1 ± 0.5
Hyp + POPC	12.5 ± 0.3
ApoNP7-Hyp + POPC	2.2 ± 0.5

Table 3.2: *Hydrodynamic radii calculated for each D_1 from Table 3.1.*

Alternatively, in the case of POPC liposomes the radii obtained offer a further consideration about apoNP7-Hyp lack of interaction with neutral membranes. Indeed, the R_H obtained for POPC together with apoNP7-Hyp (Table 3.2, right table, red) is similar to the one obtained for apoNP7-Hyp alone (Table 3.2, right table, grey). Eventually, the radii obtained from experiments with liposomes

loaded with just Hyp (Table 3.2, blue) are in the size range expected for such types of structures.

3.4 Targeting properties with imaging capabilities

It has been shown how NP7 is a suitable candidate for delivering the photosensitizer Hyp towards negatively charged membranes. ApoNP7-Hyp complex offers an effective structure to target bacteria, in the context of APDT applications as explained before. In a more generalized way, apoNP7-Hyp could prove to be a valuable solution also for PDT on cancer cells presenting an overall negative charge on the plasma membrane [107]. At this point, in order to precisely localize the PS-delivery system in live cells experiments, it is necessary to introduce a super-resolution imaging method, such as STED microscopy (Chapter 2, Section 2.4.1).

However, the exact localization of the photosensitizing compound within or around the cancer cell target is hampered by the disruptive photodynamic action of Hyp, which happens concomitantly with the high STED laser power needed to deplete the fluorescence and achieve super-resolution. This unwelcome effect dramatically affects the cells before it is even possible to localize the photosensitizer, making the visualization of uptake processes even harder [14].

Therefore, the second part of this work is focused on the introduction of imaging capabilities in NP7 via the labeling with a fluorescent dye spectrally distant from Hyp and good for super-resolution microscopy applications. The chosen probe is an ATTO647N-cadaverine which has been conjugated to NP7 through a zero-length crosslink, exploiting the presence of carboxylic acids (-COOH) naturally occurring on the protein external surface.

3.4.1 Labeling NP7: an alternative path

One of the most used procedures to label purified proteins with a fluorophore without altering their structure involves the direct chemical binding of primary amines (NH_2) through covalent formation with NHS (N-Hydroxysuccinimide) or sulfo-NHS ester. Within this framework, Lys residues are the easiest targets, not

only because they fulfill the chemical requirements needed in this type of approach but also because they are present in the majority of proteins occurring in nature [108],[109]. Nevertheless, in the specific case of NP7 this way is not practicable. The main reason lies in the fact that the extended cluster of Lys residues on the protein surface is involved in the crucial targeting activity of the PS carrier. An alternative but still effective labeling method is required.

An interesting class of bio-conjugations is the one involving the so-called zero-length cross-linkers. In this approach, the conjugation between two molecules happens with the formation of a short covalent bond, containing no additional atoms; this procedure then produces a direct linkage between two substances [110]. At the heart of this labeling procedure there is an amide linkage made by the condensation of a primary amine with a carboxylic acid (Figure 3.6). In order to create this bond, a carbodiimide is used to mediate the chemical reaction between carboxylates and amines. In a protein, the method exploits the carboxylate groups (-COOH) of glutamic and aspartic acid residues.

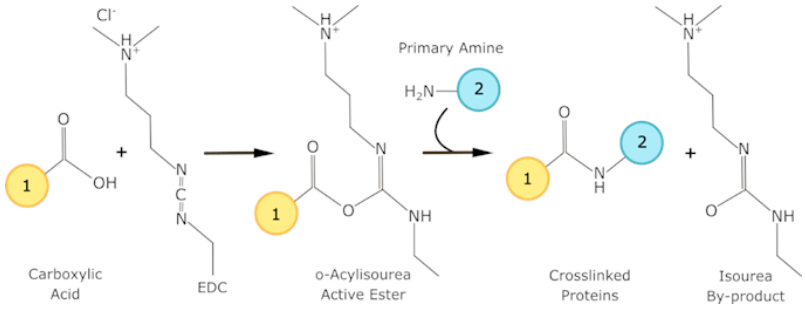

Figure 3.6: *Schematic diagram representing the chain reaction needed to create a zero-length crosslink between an amine and a carboxylic acid. 1 and 2 represents the side chains of two molecules.*

The chosen fluorescent dye for the labeling of NP7 is ATTO647N, a molecule efficiently excited in the range 625-660 nm and suitable for STED microscopy applications, conjugated with a compound called cadaverine, a molecule naturally produced by the putrefaction of animal tissue and providing the amino groups needed to perform this reaction (Figure 3.7).

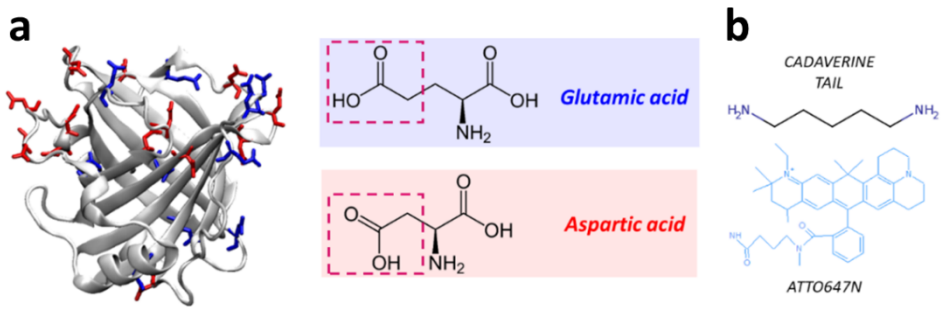

Figure 3.7: *(**a**) NP7 structural representation with glutamic acids and aspartic acids highlighted in blue and red (PDB entry: 4XME). (**b**) Representation of the main parts of Atto647N-cadaverine showing the presence of amines for performing the zero-length crosslinking.*

The carbodiimide for the experiment is EDC (1-ethyl-3-(3-dimethylaminopropyl) carbodiimide hydrochloride), a popular carbodiimide widely used for biological conjugates for its versatility and its water-solubility. Once put in the solution together with the protein of interest, EDC reacts with the carboxylic groups creating an active-ester intermediate (Figure 3.6, Active Ester) able to form an amide bound when an amine is present in the surroundings (Figure 3.6, introduction of the Primary Amine). The bound occurs with the formation of an isourea byproduct (Figure 3.6, last element on the right) [110]. In ATTO647N-cadaverine, the cadaverine tail provides the primary amine NH_2 in the zero-length crosslinking reaction. The carboxylic groups are provided by the glutamic acid and aspartic acid residues present on the protein surface (Figure 3.7a). In this way, the final results will be a mixed solution of NP7-ATTO647N-cadaverine and the isourea byproduct that can be easily removed via gel filtration. From now on, NP7 labelled with ATTO647N-cadaverine will be referred to as NP7-ATTO647N. The zero-length link is formed indeed via the direct binding of the amine on the cadaverine with one of the carboxyl group activated by EDC. Besides, cadaverine is remarkably small (~102.18 Da) and its length is negligible once the zero-length link is formed.

The choice of ATTO647N ($\varepsilon = 1.5 \times 10^5 M^{-1}cm^{-1}$) as the fluorescent probe lies in its spectral properties (Figure 3.8).

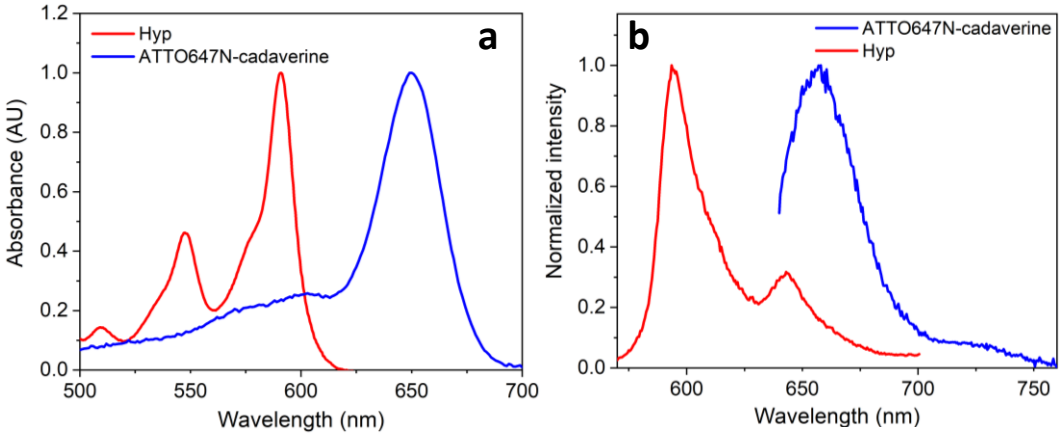

Figure 3.8: *Absorption (**a**) and emission (**b**) spectra of hypericin (red) and ATTO647N-cadaverine (blue), both substances are dissolved in DMSO. Excitation spectra are taken at λ_{ex} 550 nm for Hyp and 640 nm for ATTO647N.*

In facts, being the absorption spectrum of ATTO647N centered around 650 nm, it does not overlap with the absorption properties of Hyp and therefore it fulfills the requirement of separating the photosensitizing activity from the imaging capability of the delivery system. Different tests have been run in order to select a protocol allowing the maximization of the labeled protein, always following the procedure explained before for the zero-length crosslinking via EDC. The final selected protocol has led to a labeling ratio of 2:1 NP7 unit per ATTO647N-cadaverine molecule. This relative concentration has been calculated from the absorption spectrum of the compound (Figure 3.9b) applying the Beer-Lambert law.

Although the absorption spectrum is useful to gain an insight on the coexistence of the two compounds of interest and on their relative concentration, it does not provide a quantitative evaluation of the effectiveness of the labeling. More specifically, the absorption measurement alone is not adequate to state the effective bonding of NP7 with ATTO647N-cadaverine. Therefore, in order to assess the effective labeling of the multi-functional carrier, measurements of excitation fluorescence anisotropy (Figure 3.9a) were performed.

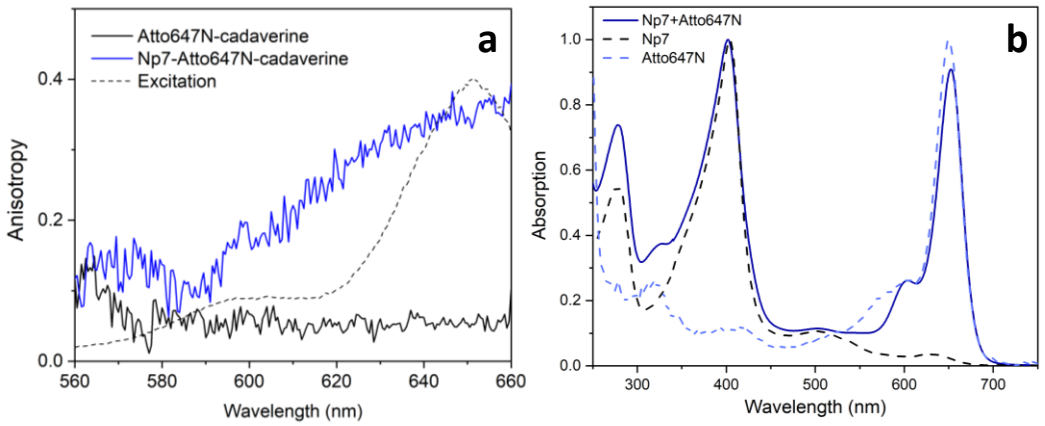

Figure 3.9. *Measurements for the preparation of NP7-ATTO647N-cadaverine complex according to the zero-length crosslink protocol. To assess the effectiveness of the labeling, excitation fluorescence anisotropy measurements were performed (**a**) comparing ATTO647N-cadaverine alone with the elute complex. The anisotropy signal of the fluorophore approaches the zero value, as expected for small dyes few Da in size. Conversely, the complex NP7-ATTO647N displays a higher anisotropy signal almost approaching 0.4, supporting the observation that the fluorophore is now linked to a bigger scaffold, i.e. protein NP7 (~ 21 kDa). In (**b**) absorption spectra of NP7 and ATTO647N-cadaverine before crosslinking are shown (dashed lines). The peaks in NP7 spectrum are due to the heme group (λ_{abs}= 403 nm) and the aromatic residues (λ_{abs}= 280 nm). The absorption spectrum of the complex after the gel filtration is also shown (solid line): the relative concentration between NP7 and ATTO647N-cadaverine has been estimated by considering heme concentration relative to ATTO647N concentration.*

Measurements of excitation fluorescence anisotropy are based on the excitation of the sample with polarized light: in this way, the emission from the sample itself is also polarized, where the extent of polarization is described in terms of the anisotropy, i.e. the differences in the emission intensity along different axes of polarization [67]. Fluorescence anisotropy measurement reveals the rotational displacement of the fluorophore that occurs between its excitation and subsequent fluorescence emission. The extent of this displacement depends on the viscosity of the solvent but also on the size and shape of the rotating molecule. A small fluorescent molecule, i.e. a dye, moves rapidly in the solvent and the polarization if its fluorescence emission will be difficult to detect. Conversely, when such a small fluorescent molecule is attached to a larger one, for example a protein, its rotational freedom will significantly decrease and a high anisotropy signal will be detected, i.e. rotational averaging is prevented. Excitation fluorescence anisotropy is an effective way to quantify protein association with

other molecules, in our case NP7 with ATTO647N-cadaverine. The comparison of the anisotropy signal between unbound ATTO647N-cadaverine (dissolved in DMSO) and NP7-ATTO647N (in PBS) is shown in Figure 3.9. Specifically, data plots in Figure 2.9b shows that NP7-ATTO647N presents a higher anisotropy signal than ATTO647N alone, approaching the maximum anisotropy value of r_0 = 0.4, the maximum theoretical value which coincides with the excitation and emission dipoles to be parallel. The minimum value is r_0 = -0.2, when the dipoles are perpendicular.

3.5 Preservation of the affinity for negatively charged membranes

The linking method described in the previous section was chosen for avoiding the saturation of the Lys cluster necessary for NP7 to target negatively charged membranes. In the interest of assessing the preservation of NP7 specificity, the complex has been furtherly tested via FCS experiments. NP7-ATTO647N interaction has been studied on two different model membranes and a potential biological target for APDT: neutral liposomes (POPC, phosphatidylcholine), negatively charged liposomes (TOCL, tetraoleyl cardiolipin) and *E. coli* bacterial cells (known to present an overall negative charge on their walls). For each model, the concentrations of NP7-ATTO647N used were 50, 100 and 200 nM (these concentration values were derived from ATTO647N absorption peak at 646 nm through Beer-Lambert law). ATTO647N fluorescence emission was collected for the FCS measurements (λ_{ex} = 635 nm), while in a parallel set of experiments on liposomes and Hyp, the emission of the latter one was used (as already done in Section 3.3). Experiments with NP7-ATTO647N and Hyp were not carried out at the same time. FCS curves of liposomes with Hyp were collected separately (λ_{ex} = 475 nm) and then plotted with the others to offer a visual comparison. Measurements with liposomes exposed to Hyp where performed as a control for the FCS measurements, in order to assess their correct formation.

The results obtained in this set of experiments demonstrated that NP7-ATTO647N selectivity remained untouched from the labeling procedure. Subsequently, both model membranes and bacterial cells have been used in imaging experiments. FCS results are now presented and discussed.

3.5.1 NP7-ATTO647N

The labeled protein was used in a first FCS experiment to check its diffusion coefficient and collect a G(τ) curve of the sole NP7-ATTO647N system. Measurements were performed at ATTO647N concentration of 50 nM. Diffusion coefficients and average diffusion times are shown in Table 3.3.

NP7-ATTO647N			
D_1 (μm²/s)	D_2 (μm²/s)	τ_1 (ms)	τ_2 (ms)
70 ± 9	266 ± 15	0.35 ± 0.05	0.09 ± 0.004

Table 3.3: *Diffusion coefficient and average diffusion time values of NP7-ATTO647N freely diffusing in solution. The introduction of a second species (D_2) allowed the distinction of free ATTO647N within the solution. Values are the mean of four different acquisitions.*

In contrast to what expected, FCS data analysis has shown the existence of two different diffusing species. D_1 ~70 μm²/s is compatible with NP7 (Section 3.3) while D_2 ~ 266 μm²/s highlights the presence of freely diffusing ATTO647N dye not attached to the protein [111]. These mixed conditions might preclude a correct evaluation of the selectivity of NP7-ATTO647N; generally, fluorescent dye tends to spontaneously establish hydrophobic interaction with the environment, hence lipid bilayers or biological membranes are at risk with nonspecific dye accumulation. Nevertheless, this problem should be moderated for ATTO647N, since the probe should be moderately hydrophilic [112].

FCS measurements performed on model membranes and subsequently on bacterial walls show that this mixed composition does not affect NP7-ATTO647N targeting, so that solid conclusions can be drawn on the specificity of the delivery system.

3.5.2 NP7-ATTO647 and neutral liposomes

Interaction with neutral liposomes (POPC) was tested in three sets of experiments with NP7-ATTO647N. ATTO647N concentration conditions and

corresponding diffusion parameters are listed in Table 3.4. In Figure 3.10, a representative FCS curve for each sample preparation is presented (representative measurements with an ATTO647N concentration of 100 nM). In the same figure, a measurement carried out on a sample of POPC liposomes and Hyp is also included.

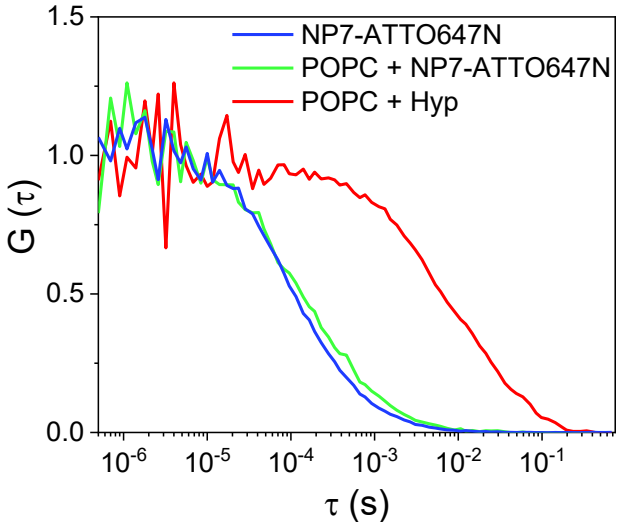

Figure 3.10: *Normalized FCS curves of NP7-ATTO647N alone (blue) and together with POPC liposomes (green). In both cases, ATTO647N concentration is 100 nM. An FCS measurement of POPC liposomes with Hyp is also presented (red).*

Already from a visual inspection of Figure 3.10, it is possible to notice a significant similarity between the diffusion dynamics of the sample with solely NP7-ATTO647N (blue) and the one including the molecule together with POPC liposomes (green). For all three ATTO647N concentrations (Table 3.4, on the left), the values interval for the diffusion coefficient *D* (~50-70 $\mu m^2/s$) is consistent with the one of freely diffusing NP7-ATTO647N.

POPC + NP7-ATTO647N			POPC + Hyp	
nM	**D** ($\mu m^2/s$)	**τ** (ms)	**D** ($\mu m^2/s$)	**τ** (ms)
50	52 ± 5	0.46 ± 0.04	4 ± 1	6 ± 2
100	53 ± 11	0.5 ± 0.2		
200	60 ± 14	0.4 ± 0.1		

Table 3.4: *On the right, diffusion coefficient and average diffusion time values of the sample NP7-ATTO647N with POPC liposomes. On the left, diffusion time of POPC liposomes loaded with Hyp. Values are the mean of 4 measurements.*

This might suggest that the protein is not interacting with neutral liposomes; indeed, if it were the case, a much smaller diffusion coefficient would be present. In support of this observation, the diffusion coefficient (Table 3.4, on the right) D ~4 ± 1 $\mu m^2/s$ obtained from the FCS curve of POPC liposomes and Hyp (Figure 3.10a, red) demonstrates the presence of objects tens of nanometers in size. This means that Hyp accumulates on POPC liposomes while NP7-ATTO647N does not, as demonstrated by the much bigger values of the diffusion coefficient of NP7-ATTO647N alone(Table 3.4, on the left).

3.5.3 NP7-ATTO647N and negatively charged liposomes

Interaction with negatively charged liposomes (TOCL) was tested again in three sets of experiments with NP7-ATTO647N. Another table (Table 3.5) containing ATTO647N concentration values and corresponding diffusion parameters is presented below. For the NP7-ATTO647N concentration of 100 nM, a FCS curve of the protein alone and with TOCL liposomes is presented in Figure 3.11. Also in this case, a measurement of liposomes loaded with Hyp is presented.

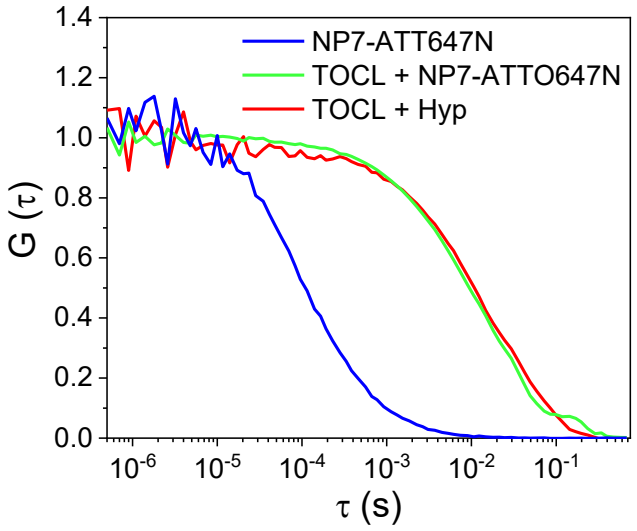

Figure 3.11:: *Normalized FCS curves of NP7-ATTO647N alone (blue) and together with TOCL liposomes (green). In both cases, ATTO647N concentration is 100 nM. An FCS measurement of TOCL liposomes with Hyp is also presented (red).*

TOCL + NP7-ATTO647N			TOCL + Hyp	
nM	**D** (μm²/s)	**τ** (ms)	**D** (μm²/s)	**τ** (ms)
50	3.6 ± 0.6	7 ± 1	1.8 ± 0.2	13 ± 2
100	3.4 ± 0.3	7.0 ± 0.5		
200	2.3 ± 0.7	11 ± 3		

Table 3.5: *On the right, diffusion coefficient and average diffusion time values of the sample NP7-ATTO647N with TOCL liposomes. On the left, diffusion time of TOCL liposomes exposed to Hyp. Values are the mean of 4 measurements.*

In this case, the values range of the diffusion coefficient *D* obtained in the measurements performed on the sample containing both NP7-ATTO647N and TOCL liposomes (*D* ~3–3.7 μm²/s) matches the one obtained from TOCL liposomes loaded with Hyp FCS curves (*D* ~1.8 ± 0.2). The labelled protein is loaded on the lipid bilayer of TOCL liposomes and the resulting diffusion dynamic is the same for all the three concentrations tested.

3.5.4 A potential APDT target: NP7-ATTO647N on *E.coli*

A final FCS measurement of the complex NP7-ATTO647N was performed on E.coli bacterial cells, known to possess an overall negative charge on their external walls. The measurements were run using a NP7-ATTO647N concentration of 100 nM and the resulting autocorrelation curves are presented in Figure 3.12.

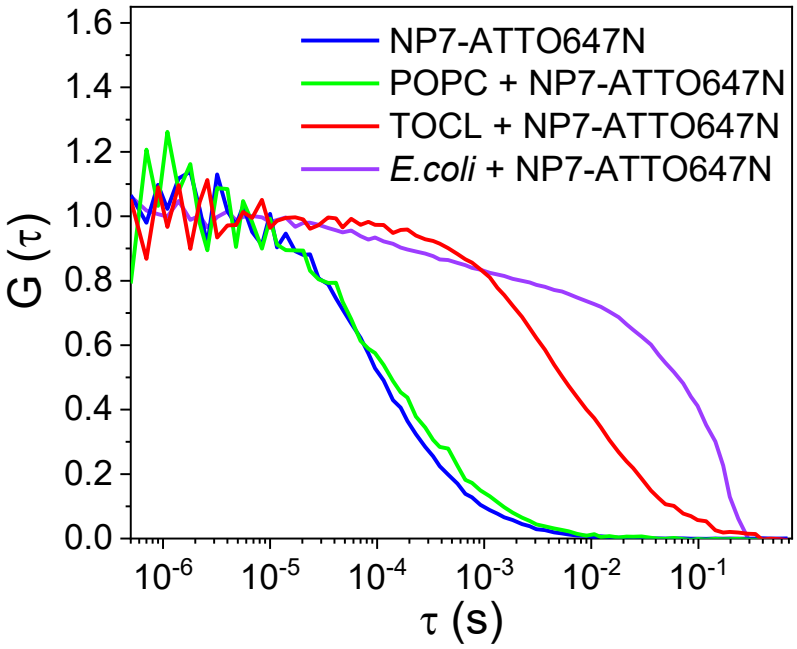

Figure 3.12. *Normalized FCS correlation curves of freely diffusing NP7-ATTO647N (blue), with neutral POPC liposomes (green), with negatively charged TOCL liposomes (red) and eventually with E.coli bacterial cells (purple). NP7-ATTO647N concentration is 100 nM for all the curves presented. Going from the freely diffusing protein to E.coli, it is possible to appreciate the increase in width of the autocorrelation curves.*

Observing the measurements collected in the figure, it is possible to see how big diffusive species appears in the FCS probing volume only when negatively charged surfaces (i.e. TOCL liposomes and *E. coli* cells) are present in solution together with the protein NP7-ATTO647N. In general, FCS measurements with bacterial cells are made more complex by the inherent inhomogeneity on the sample: *E.coli* specifically tends to aggregate quite easily, forming big clumped objects that take a lot of time to cross the FCS confocal volume. These objects contribute with their photons to extend the decay time of the autocorrelation curves, making the curve fitting quite complex to manage. In this case, it was not possible to generate a satisfying fitting function for quantifying the diffusion coefficient in the case of *E.*

coli. However, a visual inspection of Figure 3.12 might be considered enough to say that NP7-ATTO647N successfully interact with bacterial cells, proving to be a good candidate for been applied in PDT approaches where the targeting of negatively charged surfaces is needed.

3.6 Imaging properties tested on liposomes

In the previous section, the selectivity of NP7-ATTO647N towards anionic membranes has been successfully proved throughout FCS experiments. The step forward in the development of such type of delivery system is a set of measurements aimed to test its applicability in conventional and super-resolution imaging. In this new set of microscopy experiments, the protein complex has been tested on the same liposomes previously used (POPC and TOCL, liposomes). The biological targets are again *E.coli* cells, which in this case have been used in a dual-color STED experiment. The images presented in the next sections confirm the capabilities of NP7 both on liposomes and bacterial cells, while the spectral properties of ATTO647N allows to reach high spatial resolution when performing STED nanoscopy.

3.6.1 Confocal and STED microscopy on liposomes

The results on liposomes are presented in Figure 3.13 and Figure 3.14. Images have been acquired through the use of a confocal and a STED microscope respectively. In general, liposomes size can range from 30 nm to several micrometers. When their dimension is less than 200 nm, it is impossible to observe the spherical features of their lipid bilayer with a conventional microscope (Figure 3.13B) given the resolution limit which hinders the observation of objects below 200 nm (Chapter 2, Section 2.2.1). 200 nm is also the optical resolution of a confocal microscope. In order to overcome this limitation and observe the binding of NP7-ATTO647N on the liposomes membrane, images have also been taken using STED microscopy, which allows to resolve details down to few tens of nanometers.

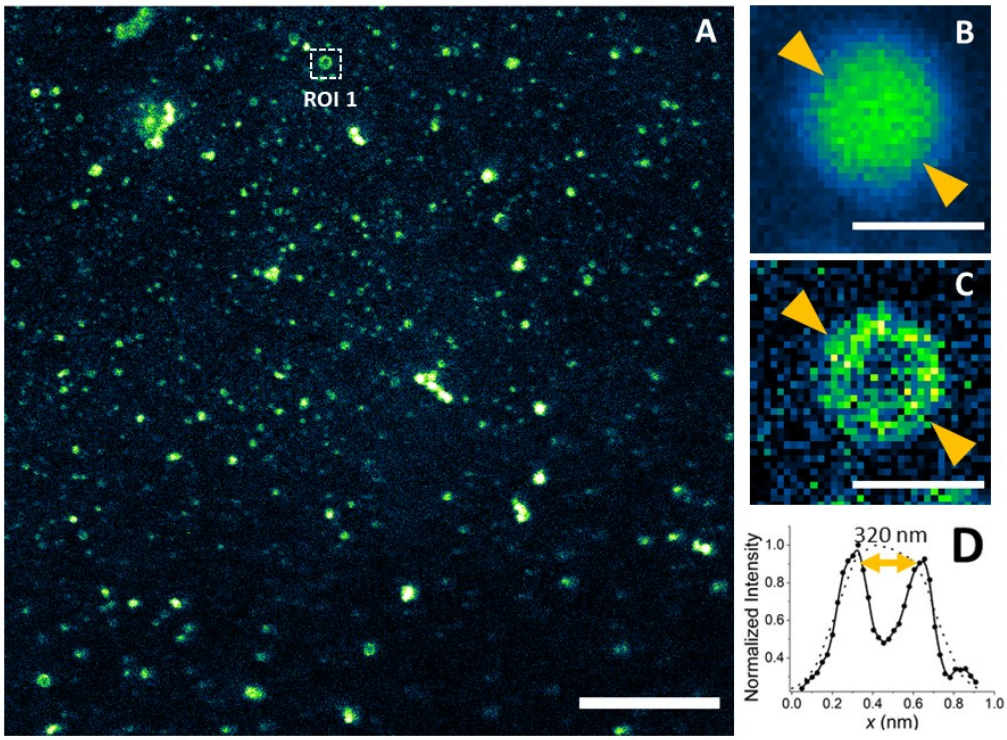

Figure 3.13: *(**A**) Image of liposomes (1024x1024 pixel) made up of negatively charged phospholipids, acquired using a STED microscope (depletion wavelength of 775 nm). The collected fluorescence signal is from NP7-ATTO647N (excitation wavelength 640 nm) bound to the model membranes in the sample. This measurement further confirms the results previously obtained from FCS. Scale bar 5 µm. The area marked with a yellow dashed line has been enlarged to show the gain in resolution when passing from confocal (**B**) to STED (**C**), demonstrating that super-resolution is needed to resolve the spherical shape of the bilayer. Scale bar 500 nm. (**D**) Line intensity profile on the right of the liposome showed in (**B**) and (**C**).*

As already mentioned before, ATTO647N is spectrally suitable for fluorescence depletion. Imaging with STED gives assess to morphological details as the one presented in Figure 3.13C. The spherical shape of TOCL liposomes is nicely resolved, while the intensity line profile displayed in Figure 3.13D provides a handy quantification of the liposomes dimension.

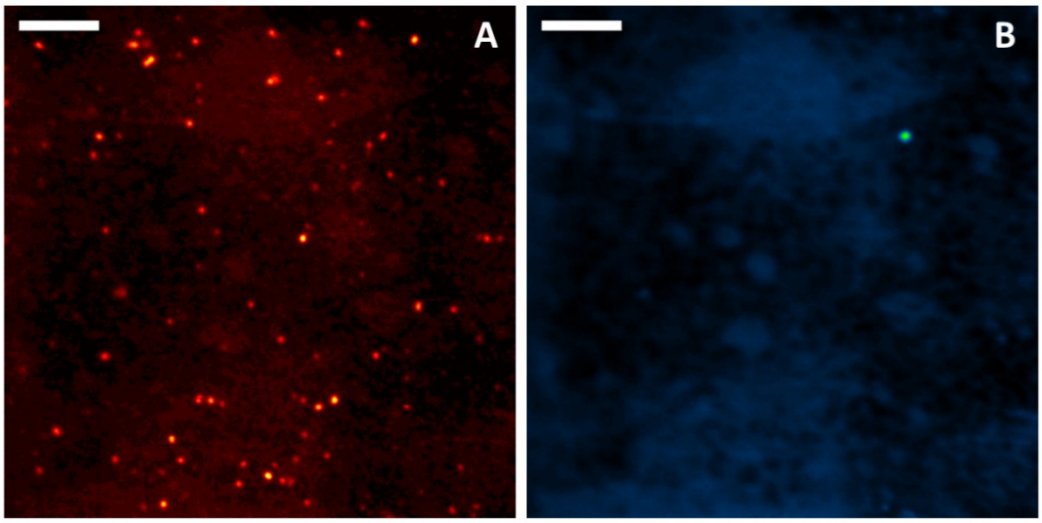

Figure 3.14: *Images of liposomes made up of neutral phospholipids, acquired using a confocal microscope. (**A**) In order to co-localize NP7-ATTO647N on the model membranes, liposomes were first loaded with Hyp (in red). Hyp was excited at 560 nm. Being an hydrophobic molecule, Hyp tends to accumulate on phospholipidic bilayers. Then, to the same sample of liposomes, NP7-ATTO647N has been added (**B**). The comparison of the two images clearly shows that the protein complex is not interacting with the neutral liposomes, as expected from the FCS experiments performed with the apoNP7-Hyp complex.*

The selective formation of an electrostatic interaction of NP7-ATTO647N with negatively charged membranes has also been demonstrated in a co-localization experiment using a confocal microscope. Images are presented in Figure 3.14. POPC liposomes were first loaded with Hyp and then exposed to NP7-ATTO647N, in order to perform a dual-color experiment. A visual comparison of the two channels is sufficient to state the absence of co-localization between Figure 3.14A and B. This result agrees with the previous FCS experiments, demonstrating that the selectivity of NP7-ATTO647N can be successfully used for imaging applications.

3.6.2 A biological model: imaging *E.coli* walls

E.coli is a Gram-negative bacterium. The bacterial cells are characterized by a cylindrical shape which is usually 1 to 2 µm long, with a radius of roughly 500 nm [113]. Their bacterial wall is made up of a thin peptidoglycan layer, surrounded by another outer layer containing lipopolysaccharide. Conversely to Gram-positive bacteria, Gram-negative bacteria walls are quite thin, being only few nanometers

in thickness [114]. Therefore, this particular biological structure challenges the spatial resolution achievable with modern super-resolution techniques.

Within this work, the localization of NP7-ATTO647N on the *E. coli* outer wall is a key point for stating the effectiveness of the complex as an efficient targeting delivery system. Moreover, using *E. coli* wall as a target gives also the possibility to investigate where exactly on the bacterial envelope NP7-ATTO647N is accumulated. To do so, it was first necessary to label bacterial walls with another dye suitable for STED microscopy, in order to quantify more accurately the co-localization of NP7 delivery system with the bacterial structure. *E.coli* envelope was then labelled using Nile Red (λ_{ex} = 560 nm, λ_{em} = 635 nm), an exchangeable fluorescent molecule. Nile Red was already been used in 3D STED imaging experiments on *E. coli* [115].

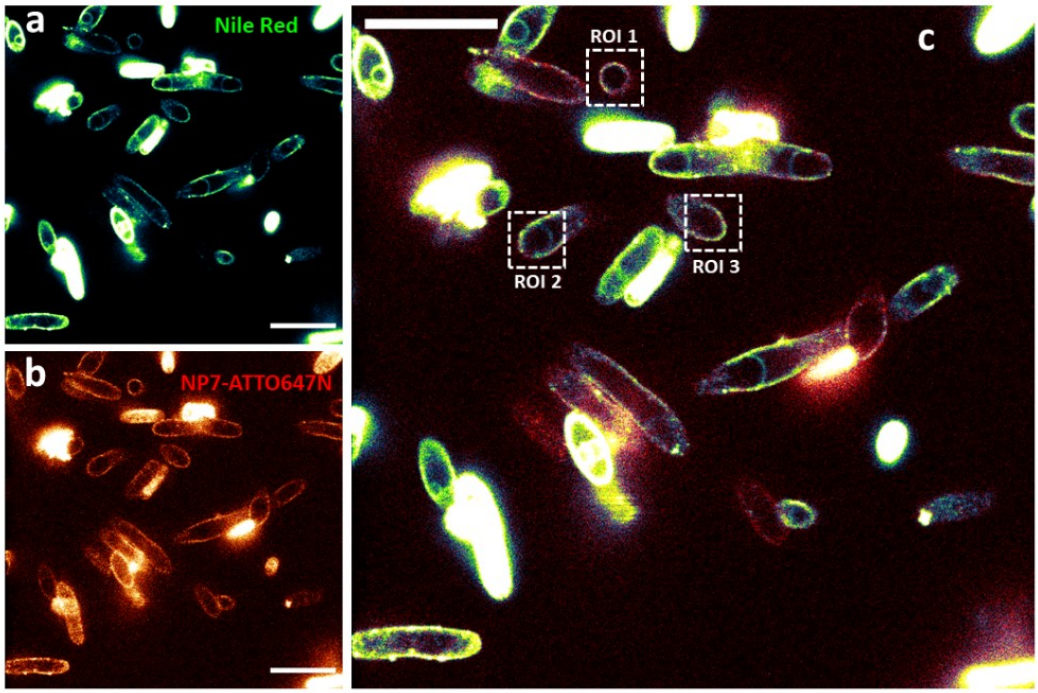

Figure 3.15: *Labeling of E.coli with Nile Red and subsequently incubated with NP7-ATTO647N (4 µM and 125 nM respectively). (**a**) STED acquisition of Nile Red excited at 561 nm depleted at 775 nm. The fluorescence signal is distributed on the bacterial wall. (**b**) STED image of NP7-ATTO647N acquired simultaneously with (**b**) with an excitation at 640 nm and same depletion beam. The protein complex accumulates on the bacterial envelope. (**c**), merge of (**a**) and (**b**). ROIs are highlighted with a white dashed line. Scale bar 5 µm for all the images.*

Its great advantage lies in its capability of reversibly bind to its target, in a continuous exchange with the imaging buffer: this peculiarity promote the replacement of the photo-bleached fluorescent molecules during the imaging process, allowing the fast exchange with intact label molecules. This contributes to have a higher signal-to-noise ratio and thus a higher resolution in the image. Since Nile Red fluorescence can be depleted at λ_{STED} = 775 nm, in can be easily combined with ATTO647N for collecting dual-color STED images.

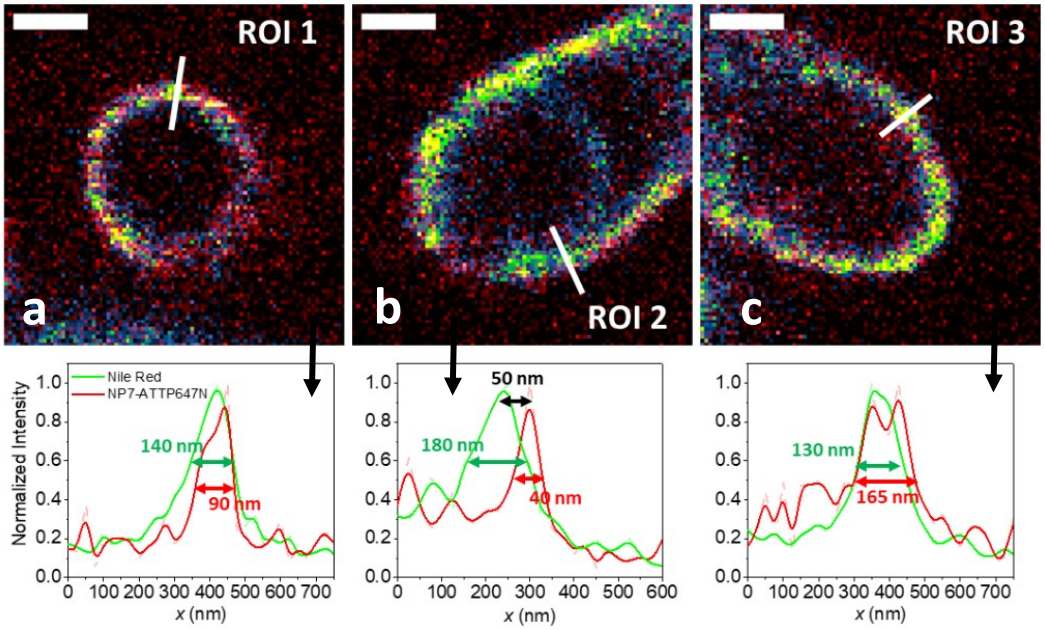

Figure 3.16: *Magnified images of ROIs from Figure 3.15: Labeling of E.coli with Nile Red and subsequently incubated with NP7-ATTO647N (4 µM and 125 nM respectively). (**a**) **STED** acquisition of Nile Red excited at 561 nm depleted at 775 nm. The fluorescence signal is distributed on the bacterial wall. (b) STED image of NP7-ATTO647N acquired simultaneously with (b) with an excitation at 640 nm and same depletion beam. The protein complex accumulates on the bacterial envelope. (c), merge of (**a**) and (**b**). ROIs are highlighted with a white dashed line. Scale bar 5 µm for all the images.*

STED images of *E. coli* bacterial cells labelled with Nile Red and subsequently loaded with NP7-ATTO647N is presented in Figure 3.15. Their typical rod-shape is clearly highlighted by Nile Red (Figure 3.15a) as expected from literature. Furthermore, also NP7-ATTO647N (Figure 3.15b) seems to accumulate on the bacterial envelopes. The merge of the two images is presented in Figure 3.15c. From the merge, three different region of interests (ROIs) have been zoomed and furtherly analyzed in Figure 3.16. Below each image crop is presented the corresponding line intensity profile traced on the images. The assessment on the

thickness of the bacterial envelope has been made via the calculation of the Full Width Half Maximum (FWHM) obtained applying a Gaussian fit for each of the peaks presented.

The enlarged images of Figure 3.16 offer the possibility of better visualize the distribution of Nile Red and the complex NP7-ATTO647N. Line profiles traced over different portions of the bacterial envelope show that it is possible to measure portion of the bacterial envelope down to 40 nm (Figure 3.16, ROI2). Furthermore, they show that the relative distribution of both fluorescent molecules is quite variegate. More specifically, in Figure 3.16, ROI1 it seems that Nile Red well co-localize with NP7-ATTO647N, with no significant displacement between the two peaks. Conversely, in Figure 3.16, ROI2 the two peaks corresponding to the line profiles do not perfectly overlap, showing a relative displacement of roughly 50 nm. Even if this length is excessively big for being identified as the separation between the two layers forming the bacterial wall, it is interesting to notice how in certain cases Nile Red can diffuse inside the inner envelope of the cell, while NP7-ATTO647N seems to remain localized on the outer layer. An optimization of the imaging procedure should be performed in order to collect images less saturated with Nile Red and more concentrate with NP7-ATTO647N. In addition to this, a more sustained image analysis for the quantification of the relative displacement of the two fluorescent signal should be performed. A good way to go could be the application of an image cross-correlation analysis [116]. This method might be useful to quantify the proximity of Nile Red and NP7-ATTO647N from the dual-color image of Figure 3.15.

This preliminary nanoscopy studies show how NP7-ATTO647N can perform as an effective targeted delivery system on negative bacterial walls. The combination of Nile Red and NP7-ATTO647N has also been tested on TOCL and POPC liposomes, with the aim of providing a complete study of the complex in all the different conditions tested. STED images on TOCL and POPC liposomes are shown in Figure 3.17 and Figure 3.18, respectively. In Figure 3.17, it is interesting to notice how Nile Red is located inside the liposomes structure, while NP7-ATTO647N can be nicely localized on the lipid bilayer. This difference might be due to the diverse size of the two fluorescent complexes: because of its small molecular size, Nile Red might be able to diffuse inside the liposome structure. On the opposite, ATTO647N is linked to a protein is way bigger compared to Nile Red and then not able to go through the liposomes membrane. Eventually, POPC liposomes (Figure 3.18) display the same properties already demonstrated in the previous sections.

Specifically, the absence of spatial co-localization between Nile Red and NP7-ATTO647N once again prove the selective activity of NP7 towards negatively charged membrane. As additional comparison, the line profiles for negative and neutral liposomes is presented in Figure 3.19. NP7 then is confirmed as a potential good delivery system for application in photodynamic therapy.

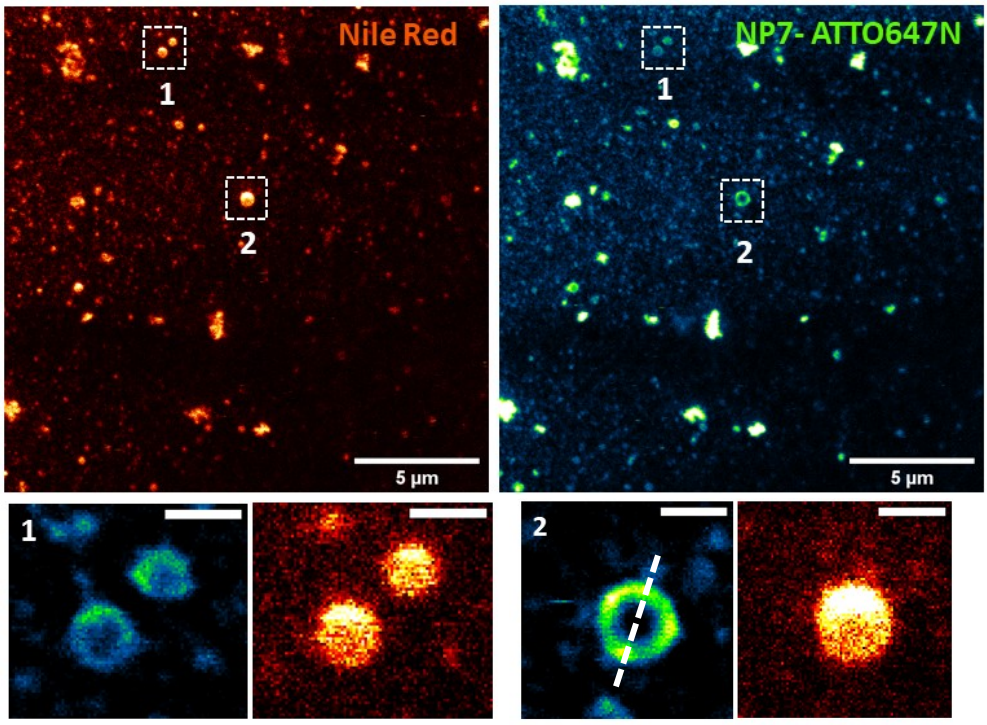

Figure 3.17: *TOCL liposomes labelled with Nile Red and incubated with NP7-ATTO647N (4 µM and 125 respectively). Imaging condition are the same as reported in Figure 3.15. Two ROIs are highlighted and presented in enlarged figures below. While Nile Red appears diffused all inside the liposomes, NP7-ATTO647N is nicely located on the lipid bilayer. Scale bar, where not indicated, are 500 nm.*

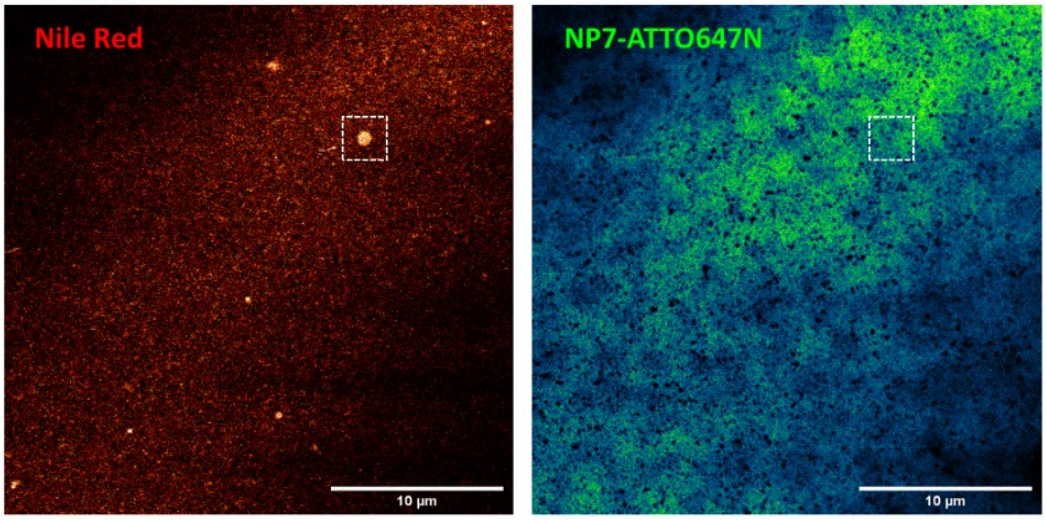

Figure 3.18: *POPC liposomes labelled with Nile Red and incubated with NP7-ATTO647N (4 µM and 125 respectively). Imaging condition are the same as reported in Figure 3.15. Nile Red is clearly visible on the liposomes membranes, while NP7-ATTO647N does not co-localize in the other channel.*

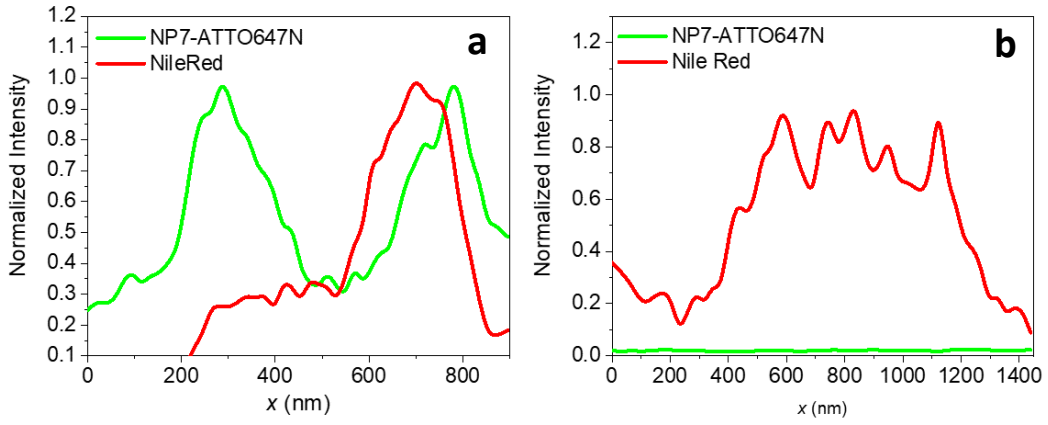

Figure 3.19: *Intensity line profiles of liposomes from Figure 3.17 (**a**) and Figure 3.18 (**b**). (**a**) is from ROI2, where from visual inspection it is possible to observe the presence of both NP7-ATTO647N and Nile Red, as expected for in the case of negatively charged liposomes. On the other hand, in (**b**) it is evident how NP7-ATTO647N is not found on the lipid bilayer of neutral liposomes, where the sole presence of Nile Red is highlighted.*

Chapter 4

4 Streptavidin-based delivery systems

The example previously offered by Nitrophorin 7 has shown the advantages of a protein-based carrier, being such type of molecular systems intrinsically biocompatible and highly versatile. Specifically, the use of hydrophobic interactions for assembling NP7 with the Hyp enabled the design of a delivery system with targeting capabilities towards negatively charged membranes, such as bacterial walls.

However, photosensitizers in self-assembled carriers are generally off-loaded to the membrane [117], because they do not covalently bind with the protein scaffold. Furthermore, the photosensitizing action hampers the exact spatial localization of the delivery system in the biological environment, because the cytotoxic activity is concurrent with the fluorescence emission and leads to a quick deterioration of the target in case of cancer cells [14]. More generally, a major step forward in designing an efficient delivery system is the development of a molecular carrier presenting a set of fundamental properties, distributed between targeting, imaging and photosensitizing capabilities. This array of features would allow the selective treatment of a specific target together with the possibility to spatially localize the compound in the physiological environment before inducing the photodynamic action. Such type of multifunctional system would be then endowed with all the properties needed to serve as an effective theranostic molecular platform.

In this section, it is presented the study of a protein-based scaffold with multifunctional capabilities that might be used in the future for theranostic applications. The proposed structure is based on the streptavidin-biotin complex where streptavidin (SAV) is a protein and biotin a water-soluble vitamin. The complex makes use of the natural, strong binding of SAV with biotin [118]. Such a peculiar affinity between the molecules can be exploited for combining up to four different biotinylated molecules to the main streptavidin core, in a modular approach. It would result in the introduction of a supramolecular assembly customizable with the desired specificity.

Within this framework, a SAV-based complex endowed with photosensitizing capabilities and targeting *S. aureus* has been developed. The complex was first thoroughly study from the photo-physical point of view and then used to target bacterial cells in *live cell* super-resolution microscopy experiments. The successful results obtained with the design of such multifunctional complex has led to the design of a similar SAV-based system for addressing melanoma cancer cells. In this case, the obtained preliminary results show that a different approach must be applied for the creation of a working delivery system in the cell environment.

4.1 The SAV-biotin complex

SAV is a protein of bacterial origin and structurally characterized by four subunits (Figure 4.1a). It possesses a molecular mass of ∼60 kDa and it presents exceptional affinity for biotin, a small molecule that can dissolve in water and it is involved in processes related to metabolism [119]. Biotin interaction with SAV is characterized by a selective and very strong noncovalent affinity, possessing a dissociation constant of $\sim 1.3 \times 10^{-15}$ M. This kind of stability is what has made the complex popular for a wide range of biotechnology applications, such as purification or detection of other proteins. Each SAV molecule can contain up to four biotin-binding sites, meaning that its functionalization can theoretically include up to four biotinylated compounds. SAV is soluble in water and it is extremely robust, being able to endure a wide range of buffer conditions and chemical modification processes [118]. These features make SAV-biotin an interesting building block tailored on the targeting, imaging and therapeutic properties of choice. However, the optimization of each of these functions is a crucial step for the development of a working multifunctional platform.

4.1.1 SAV functionalization with a PS

EITC was conjugated to SAV tetrameric structure exploiting the amine group. Indeed, the isothiocyanate group of EITC (Chapter 2, Section 2.1.3) can react with the N-terminal amino acid residue and the primary amines of Lys residue side-chains on SAV, creating a stable bound. The idea underlying this kind of conjugation lies in the enhancement of the photodynamic activity of the compound; in fact, the coordination of one SAV tetramer with several EITC

molecules could contribute to the increase of singlet oxygen and ROS generation in the site of interest, while the four biotin-sites are still available for any functionalization. This conjugation reaction is particularly efficient at alkaline pH. Each SAV monomer accommodates four potential reaction sites for binding a molecule of EITC, namely 3 Lys residues and the N terminal of the protein (residues are displayed in Figure 4.1a, magenta).

The absorbance spectra of SAV and EITC before and after the labeling procedure are presented in Figure 4.1b. EITC shows a characteristic absorption peak at 538 nm when dissolved in DMSO. This one shifts to 524 nm when EITC is in PBS buffer.

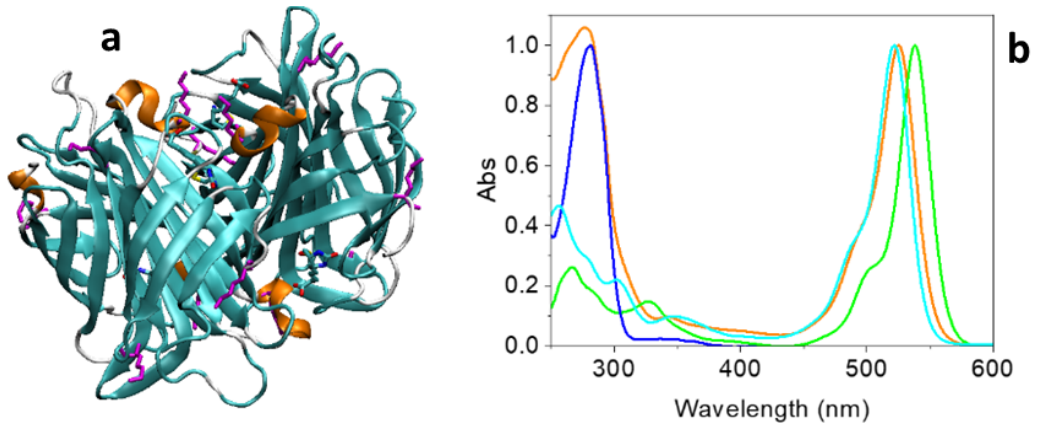

Figure 4.1: *(**a**) Three dimensional structure of strep from* Streptomyces avidinii *(PDB entry: 3wyp, solid ribbon) bound to 4 biotin molecules. The Lys residues on strep are shown as magenta sticks. The four biotin molecules bound to strep are shown as sticks. (**b**) Normalized absorption spectra of SAV in PBS buffer at pH = 7.4 (blue), EITC in DMSO (green), EITC in PBS buffer (cyan), and the complex SAV-EITC in PBS buffer at pH = 7.4 (orange). The absorption spectra were normalized at 280 nm (SAV), 538 (EITC in DMSO), 521 nm (EITC in PBS), or 525 nm (SAV-EITC in PBS).*

When the photosensitizer is bound to SAV, its absorption band is found at 525 nm. Spectra in Figure 4.1b are normalized to the absorbance of SAV at 280 nm, the distinctive peak of the aromatic rings in the protein structure. The proportion of EITC-to-SAV was estimated from the ration of the absorption peaks at 525 nm and 280 nm respectively using the Beer-Lambert law. Such proportion results in two molecules of EITC per SAV tetramer (2:1).

As in the case of NP7 (Chapter 3), absorption spectra are not enough to assess the effective labeling of SAV with EITC, since a significant percentage of photosensitizer could be free diffusing in solution. Therefore, FCS (Chapter 2, Section 2.3.1) and fluorescence anisotropy measurements have been performed

on SAV-EITC, exploiting the fact that SAV is not naturally fluorescent but EITC is. The autocorrelation curve of the experiment is presented in Figure 4.2.

The solid curve in Figure 4.2b results from a fitting made with a single diffusing species. The diffusion coefficient obtained from this measurement is D = 49 $\mu m^2/s$, with a triplet state contribution τ_T = 20 µs. This value compatible with SAV molecular weight and therefore confirming the effectiveness of the labeling procedure with EITC.

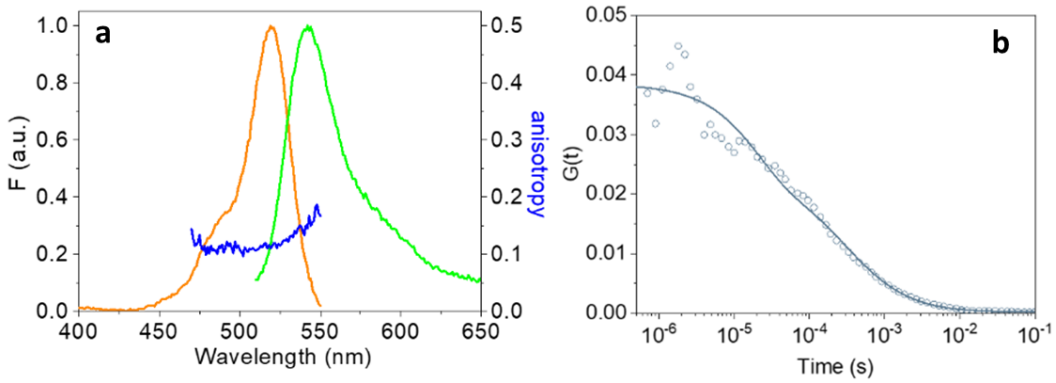

Figure 4.2: *(**a**) Normalized fluorescence excitation (orange, peak at 525 nm, emission detected at 580 nm) and emission (green, peak at 541 nm, excitation at 500 nm) for a SAV-EITC solution in PBS buffer at pH = 7.4. Fluorescence anisotropy is presented in blue (emission detected at 560 nm). (**b**) Autocorrelation curve for SAV-EITC (circles). Excitation was at 475 nm, collection of fluorescence at 550(20) nm. In the reported experiment, about 25 molecules were present on average in the confocal volume.*

In order to estimate the effects of EITC conjugation on the functional properties of SAV, it was important to determine the number of available biotin-sites on the SAV tetramer. This evaluation was carried out by taking advantage of the quenching of fluorescence emission by the biotinylated fluorescent probe STAR635 when bound to SAV. In this regards, it has been observed in a series of previous experiments (not shown in this current work) that, conversely to what would be expected for its labeling purposes, the fluorescence signal of biotinylated STAR635 dramatically decreases when interacting with SAV. The binding of the two compounds probably lead to the quenching of STAR635, making it unusable for fluorescence detection. However, this unexpected property has been indeed used for determining the available biotin-sites on SAV-EITC. Fluorescence emission spectra of biotinylated STAR635 are presented in Figure 4.3a. From visual inspection, it is possible to see how biotinylated STAR635 intensity decreases when SAV concentration progressively increases. From the

same spectra, it was possible to calculate the percentage decrement of the fluorescence emission. This quantity was then plotted as a function of SAV concentration Figure 4.3b (full orange squares).

The decrease of emission reaches its maximum when all biotinylated STAR635 have bond SAV. The quenching of the fluorescence signal comes with a small decrease in its lifetime (Figure 4.3c). The fact that the percentage decrease of fluorescence in Figure 4.3b (where the decrease is due to the quenching of STAR635 fluorescence following the binding of biotin with SAV) is linear means that biotinylated STAR635 binding to SAV is stoichiometric. Therefore, the SAV concentration at which the linear trend saturates can be used to evaluate the concentration of available biotin-sites. More specifically, the ratio between the biotinylated STAR635 and SAV-EITC concentrations constitutes a direct estimate of the number of available biotin-sites. Closely resembling results were obtained in titration experiments with biot-START and SAV-EITC (Figure 4.3b, circles): this indicates that all the biotin-site present in the conjugate are available and ready to be further functionalized with biotinylated molecules.

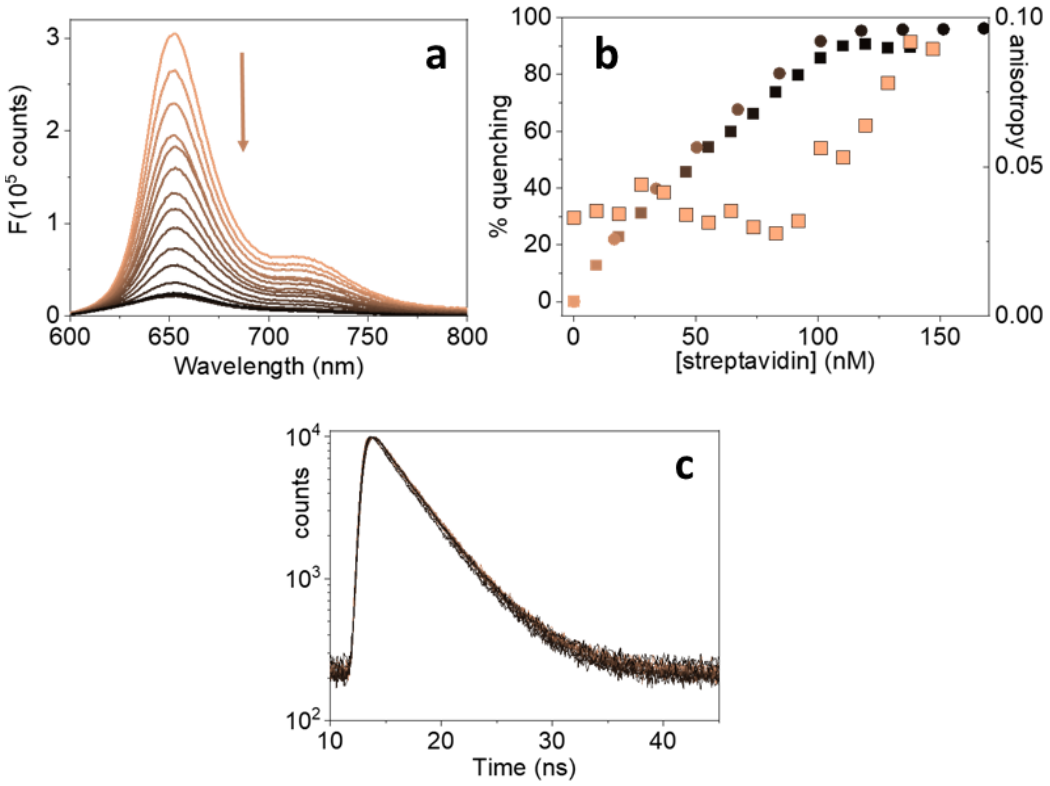

Figure 4.3: *(**a**) Fluorescence emission of biotinylated STAR635 (100 nM) as a function of SAV concentration from 0 (top) to 160 nM (bottom). The arrow indicates the direction of SAV concentration increase. The lower the fluorescence emission, the higher the SAV concentration. (**b**) Fluorescence emission intensity (integrated area) decrement of biotinylated STAR635 (100 nM) upon increasing SAV (shading squares) or SAV-EITC (circles) concentration. The concentration displayed in the figure refers to SAV monomers. In the same plot, the change in fluorescence anisotropy for the titration with SAV is also presented (full orange squares). (**c**) Fluorescence decay of biotinylated STAR635 (100 nM) as a function of SAV concentration.*

4.1.2 Targeting of *S. aureus* bacterial cells

After having characterized the SAV-EITC complex as a fully functional photosensitizer delivery system, it is now the case of providing it with effective targeting capabilities. Therefore, it is possible now to introduce a biotinylated immunoglobulin G (IgG) that specifically address protein A expressed on *S. aureus* outer envelope. The first thing to assess was the binding of the biotinylated IgG with the SAV-EITC complex throughout FCS measurements (Chapter 2, Section 2.3.1). The experimental trace of SAV-EITC is presented in Figure 4.4b (orange).

The autocorrelation curve that best describes the protein diffusion constitutes of only one diffusing species, with a diffusion coefficient D ~50 $\mu m^2/s$, as expected from a protein the size of SAV [120]. The addition of the biotinylated IgG to SAV-EITC has the effect of progressively slowing down the diffusion of SAV complex because of the binding between the two molecules.

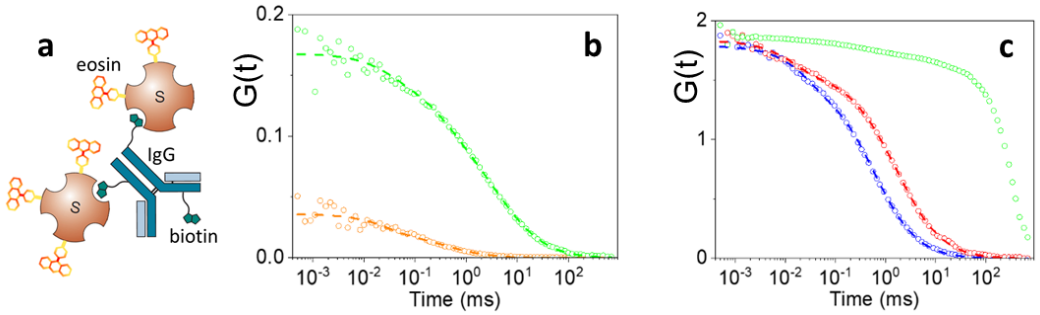

Figure 4.4: *(**a**) Drawing representing the interaction of SAV-EITC with biotinylated IgG. (**b**) Cross-correlation curves of SAV-EITC in PBS, concentration of 60 nM (orange) and SAV-EITC upon exposure to biotinylated IgG, in concentration of 32 nM (green). Dashed lines represent the fitting curves of each complex, comprising a triplet state and one (orange) or two (green) diffusing species. (**c**) FCS curves and corresponding fit curves of SAV-STAR635 alone (blue) and after incubation with the biotinylated IgG (red). A measurement with S. aureus cells and the complex IgG-SAV-EITC is also presented (green).*

FCS data are shown in Figure 4.4b (green), which are now best described by a autocorrelation function that includes two diffusive species, characterized by D = 50 $\mu m^2/s$, definitely corresponding to SAV-EITC, and by D ~5 $\mu m^2/s$. The second species could be easily identified as bigger complexes made up of multiple interaction points between SAV-EITC and the biotinylated IgG, as suggested in the sketch in Figure 4.4a. The fact that an effective recruitment of several SAV-EITC complexes for each biotinylated IgG is taking place is demonstrated by the increase of the amplitude in the FCS data (Figure 4.4b, green trace); the average number <N> of diffusing molecules is indeed given by 1/G(0) (Chapter 2, Section 2.3.1). Since <N> goes from 20 (orange) to 5 (green), it can be stated that each supra-molecular complex is made up of 4 SAV-EITC units per biotinylated IgG.

Eventually, FCS measurements of the IgG-SAV-EITC complex interacting with *Staphylococcus aureus* can be performed in order to conclude the full characterization of the delivery system. Nevertheless, the fluorescence emission from the complex IgG-SAV-EITC is quite dim. Therefore, in order to efficiently study the interaction of the complex on bacterial cells, SAV-EITC was replaced with

another SAV labelled with a brighter fluorophore emitting in the red, i.e. STAR635. Bacteria were first incubated with biotinylated IgG (like in the first step of an immunostaining procedure), in order to allow a solid interaction with protein A located on the bacteria external envelope. Subsequently, cells were exposed to SAV-STAR635 for an hour. FCS curves were then collected using an excitation wavelength of 635 nm. Experimental data are presented in Figure 4.4c. In this figure, FCS signals are normalized with SAV-STAR635 to permit and easier comparison between the different dynamics. The diffusion of SAV-STAR635 alone (blue trace) is well described with a single species characterized by D = 45 $\mu m^2/s$ and a triplet lifetime τ_T = 30 µs. On the other hand, the sample of SAV-635 incubated with the biotinylated IgG (red trace) can be well represented with a two-species fit. The first one is characterized by D ~45 $\mu m^2/s$, conforming to the value obtained previously for SAV-STAR635 alone. The second one is described by D = 12 $\mu m^2/s$, a value that can be assigned to some of the large supramolecular complexes previously discussed, encompassing several SAV-EITC and IgG molecules. When bacteria are incubated with the system IgG-SAV-EITC, the FCS curve (green trace) dramatically change in width, highlighting the presence of a dominant diffusive species with an average diffusion time of several milliseconds. Due to the high variability of the sample in terms of the formation of bacterial aggregates, a reliable quantification of the diffusion coefficient is quite difficult. Nevertheless, a visual inspection of Figure 4.4c is exhaustive enough to demonstrate that the complex IgG-SAV-EITC effectively target *S. aureus* cells.

4.1.3 Inactivation of S. aureus with IgG-SAV-EITC

Concerning the assessment of IgG-SAV-EITC as an effective system with photosensitizing capabilities, a series of *in vivo* photoinactivation on S. aureus cell suspension were performed in collaboration with the Institut Químic de Sarrià, Barcelona, Spain.

For this purpose, a suspension of *S. aureus* cells was incubated for 30 minutes with biotinylated IgG at a concentration of 100 nM, again to promote a solid interaction with the targeted protein A on the bacterial walls. Then, the complex SAV-EITC was added at increasing concentrations (in a range going from 125 nM to 1 µM), incubated 30 minutes with the cells to boost the binding with the biotinylated IgG already attached to protein A. Ultimately, bacterial cells were irradiated with green light at increasing exposure time, which corresponded to

light fluences (i.e. delivered irradiances) of 0 (no light), 10, 20 and 50 J/cm^2. The described photoinactivation measurements are presented in Figure 4.5 below.

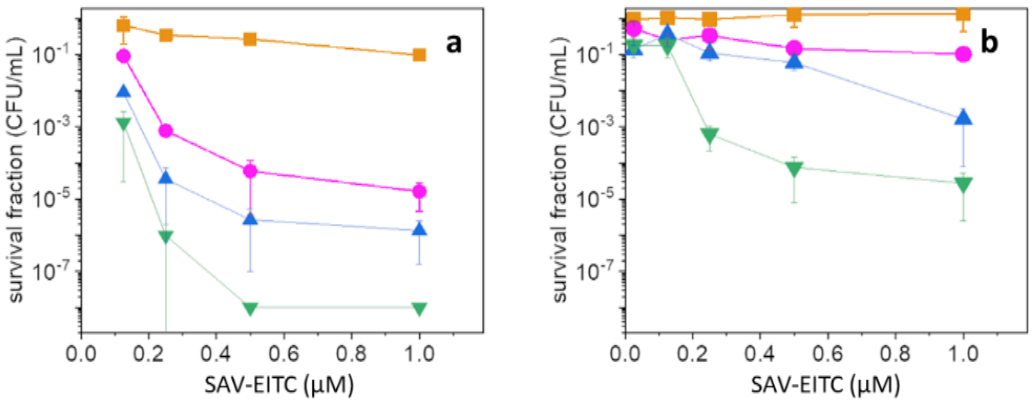

Figure 4.5: *Photoinactivation measurements demonstrate the dependence to light fluences and photosensitizer concentration in the inactivation of* S. aureus*. (**a**) Survival fraction (CFU/mL) as a function of SAV-EITC concentration (0.125, 0.25, 0.5 and 1 µM) at different increasing light fluences: 0 (dark control; orange), 10 (magenta), 20 (blue), and 50 (green) J/cm^2. Concentration of biotinylated IgG was 100 nM. (**b**) Control experiment. The same conditions of (**a**) were applied, but in this case* S. aureus *cells not pre-incubated with biotinylated IgG.*

The survival fraction CFU/mL indicates the colonial forming units per milliliters and it is used to indicate the survival fraction of bacterial cells subjected to light irradiance. In Figure 4.5a, different light fluences are represented with different colors, while SAV-EITC concentration is progressively increased. The plot clearly how shows how *S. aureus* inactivation (decrease of CFU/mL) correlates with SAV-EITC concentration and light irradiance. It is possible to observe a remarkable inactivation of 8 log in correspondence of SAV-EITC concentration 0.5 µM and a light irradiance of 50 J/cm^2. A control experiment (Figure 4.5b) in relation these photoinactivation assays was carried out without pre-incubating *S. aureus* cells with biotinylated IgG. Bacterial cells were exposed only to SAV-EITC before being again irradiated with light at different fluences. The increase of SAV-EITC concentration still slightly induces some photoinactivation, but it can be considered a residual effect due to a minor interaction between *S. aureus* and the SAV-EITC complex. The introduction of 0.5 µM concentration of the photosensitizing compound, combined with a light irradiation of 50 J/cm^2, reduces the CFU/ml of 4 log. This decrease can be compared with the 8 log reduction obtained previously in the same condition but in the presence of biotinylated IgG. The remarkable improvement shows that the introduction of a pre-incubation

with biotinylated IgG provides the great advantage of introducing a specific interaction between a targeted proteins, such as protein A, and the photosensitizing compound.

4.1.4 Imaging the IgG-SAV complex

So far, the selective binding of the IgG-SAV-EITC supramolecular complex has been thoroughly studied using different techniques, which have allowed the characterization of its photosensitizing and targeting capabilities. Speaking of the selectivity of the IgG-SAV system, its effective delivery property can be further examined using super-resolution STED microscopy (Chapter 2, Section 2.4.1).

A STED image of *S. aureus* are displayed in Figure 4.6. Bacterial cells were incubated with biotinylated IgG and then exposed to SAV-Chromeo488, a fluorophore suitable for STED imaging. In agreement with the results obtained in the previous sections, the fluorescence emission of Chromeo488 is concentrated on the outer bacterial wall, where protein A is located. The improvement resolution achievable with a STED microscope allows to discriminate between the different accumulations regions of the fluorescence signal. These ones indeed are unevenly distributed over the outer envelope. This visual observation is particularly interesting because it could support the fact that distribution of protein A is uneven on the bacterial walls, as reported in literature and discussed in relation to cellular division [121][122]. In Figure 4.6B and C present an enlarged view of ROI I and II of the STED image (A). The intensity profiles along the lines indicated in both ROIs are reported in the right part of the panel, where the intensity profiles of confocal (dashed) and STED (solid) are reported together with the fitting (orange) used to estimate the dimensions of the spots on the bacterial wall. These ones have a size on the order of 200 nm. These images unequivocally demonstrates that the supramolecular complex IgG-SAV targets *S. aureus* wall.

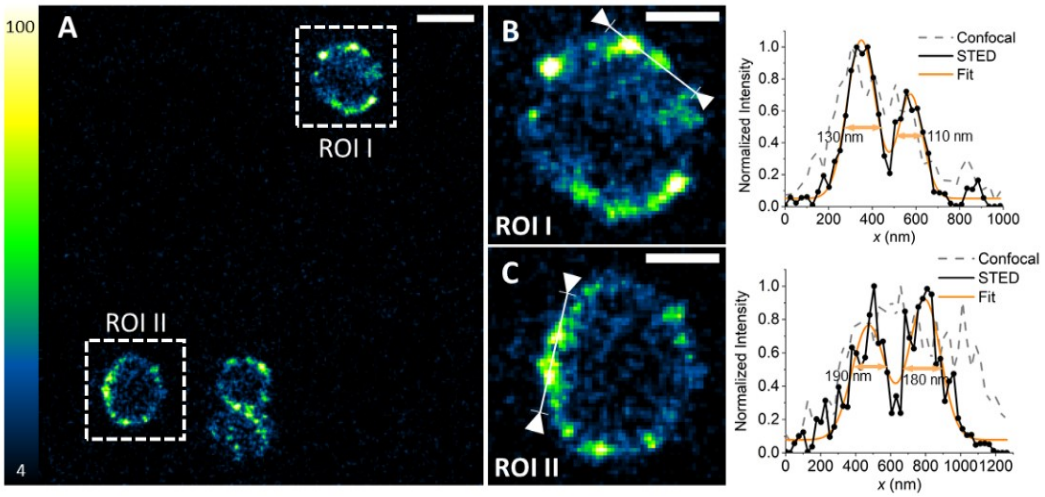

Figure 4.6: *Labeling of* S. aureus *with IgG-SAV-Chromeo488. Bacteria were incubated with IgG and Chromeo488-strep (0.5 µM and 1 µM, respectively). (**A**) STED image collected under excitation at 488 nm and detection 495-550 nm, using a depletion beam at 592 nm. The fluorescence signal is distributed on the bacterial wall. Scale bar 1 µm. (**B**) and (**C**) are magnified regions from the STED image. Scale bars 500 nm. Normalized intensity profiles measured across interesting domains on the bacterial wall are shown to the right of the corresponding magnified images. In the same intensity plots, the confocal profile is shown in comparison to the STED one (acquisition taken in a second sequential frame). A multi peak fit (orange line) has been used to assess the dimension of the domains. Estimated widths are reported in each plot.*

Besides possessing targeting capabilities, the SAV-based supramolecular structure has remarkable strain selectivity towards bacteria expressing protein A, as it is shown in Figure 4.7. In order to demonstrate the specificity of the complex, a mixed sample of *S. aureus* (expressing protein A) and *E. coli* (devoid of protein A) was prepared. The mixed sample was then incubated with biotinylated IgG for 30 minutes and exposed to SAV-chromeo488 for an additional time of 30 minutes. The confocal images reported in Figure 4.7B shows that the fluorescence signal coming from the complex is visible only in correspondence of *S. aureus* bacterial walls, whereas *E. coli* cells are devoid of any fluorescence emission. The corresponding rod-shaped bacteria can be easily identified in transmission (Figure 4.7A) and indicated by the boxes 1, 2 and 3.

In conclusion, this work demonstrated that is possible to create a multifunctional supramolecular complex using SAV as a protein scaffold. Indeed, SAV can be covalently bond to the photosensitizer EITC via the amino group on Lys residues, without hampering its capabilities of interacting with biotin (i.e. a further functionalization with biotinylated molecules of choice is fully accessible). In this

case, the conjugate has been provided with targeting capabilities towards *S. aureus* thank to the introduction of a biotinylated IgG that selectively address protein A (expressed only on *S. aureus* bacterial cells).

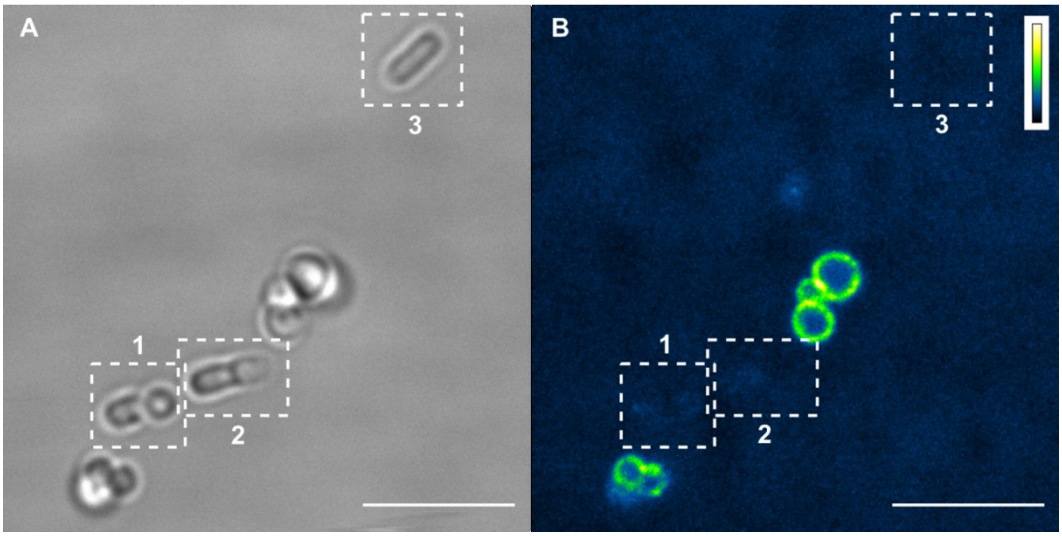

Figure 4.7: *Selective labeling of* S. aureus *with IgG-SAV-Chromeo488 in a mixed culture with* E. coli*. (**A**) Transmitted light image of bacterial cells showing the different morphology of* S. aureus *(spherical) and* E. coli *(rod-shaped). The latter ones are highlighted in boxes 1, 2 and 3. Scale bar 5 µm. (**B**) Confocal image collected under excitation at 488 nm and detection 495-550 nm. Scale bar 5 µm. Interestingly, the fluorescence signal is absent on* E. coli *walls (boxes 1, 2 and 3 in **B**).*

4.2 A SAV-based complex against cancer cells

In general, photodynamic action is not limited to antimicrobial applications, but it is also a widely used, non-invasive form of therapy applied for the treatment of non-oncological diseases as well as cancers of various types and areas [123]. Therefore, there is great interest in the development of increasingly effective PS-carriers which can strongly interact with specific cancer cells without harming the surroundings with the photosensitizer action.

The modular approach proposed in the previous section suggests that the same SAV-biotin strategy could be used to deliver photosensitizing molecules to other biological targets of interest simply replacing the biotinylated IgG with another biotinylated effector molecule. PDT against cancer cells could benefit a lot from

this strategy. For this reason, an alternative SAV-based complex for addressing a specific line of melanoma cancer cells have been investigated.

A375 is a melanoma cell line made up of adherent cells with an epithelial morphology. This line has been chosen because it shows overexpression of the Melanocortin 1 Receptor (MC1R), a seven pass transmembrane G protein coupled receptor that regulates skin pigmentation and it plays a crucial role in sun sensitivity [124]. MC1R is involved in different signaling cascades that are initiated upon interaction with different effector molecules. More specifically, human MC1R is known to interact with three major ligands [125]:

- The peptide α-MSH (melanocyte-stimulating hormone), which activates receptor signaling;
- The agouti-signaling protein (ASIP) that antagonizes the effects of α-MSH, acting as a MC1R inhibitor by preventing the binding of α-MSH with the receptor;
- The neutral antagonist β-defensin 3 (βD3).

Each of them seems to work as an inhibitor for the others and MC1R can interact with only one of them at a time. The case of α-MSH is particularly interesting; the peptide is made up of 13 amino acids [126] and it is involved in the signaling cascade that leads to the production of melanin. Interestingly, its affinity with MC1R has been determined in the A375 cell line, presenting a quite high dissociation constant of K_D = 410 ± 123 pM [127]. In the same study, it was also possible to determine the number of MC1Rs on A375 cell surface, with it being B_{max} = 608 ± 134, a value that demonstrates a moderate expression of the receptors.

Due to the encouraging preliminary study that assessed an effective interaction between α-MSH and MC1R in the cell line of choice, a biotinylated version of the hormone was selected to be in the targeting strategy of the SAV-based complex.

In order to evaluate the effectiveness of this targeting strategy, a set of *live cell* experiments using confocal microscopy was performed. For this study, the resolution limit of 200 nm does not limit the investigation of the interaction. Using SAV covalently labelled with fluorescein (FITC), different cell conditions have been tested for assessing the existence of a specific membrane interaction mediated by the biotinylated α-MSH. In Figure 4.8, the first set of measurements is presented.

Cells were first incubated with the biotinylated α-MSH for 30 minutes at 37 °C. Subsequently, cells were exposed to SAV-FITC for 10 minutes and imaged at the confocal microscope. Panel A, B and C are acquisition from three different slides, all prepared in the same way. The solution of SAV-FITC added in the second passage was gently removed and replaced with Live Cell Imaging solution (pH 7.4) in order to reduce the background.

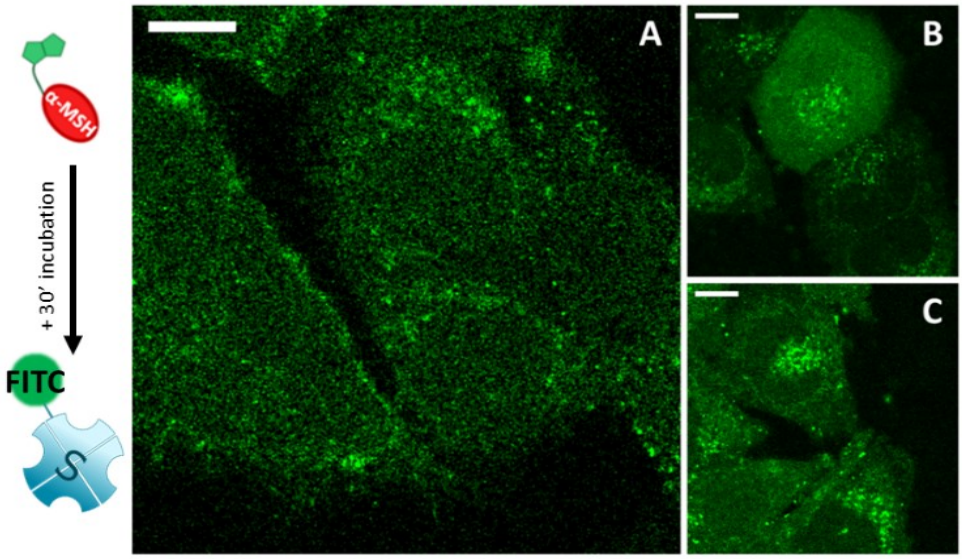

Figure 4.8: *Confocal live cell experiments with A375 melanoma cancer cells incubated 30 min with the biotinylated α-MSH peptide and subsequently exposed to SAV-FITC.The distribution of SAV-FITC (**A**, **B** and **C**) accumulates on the plasma membrane. Excitation wavelength 480 nm. Scale bar 10 µm.*

The fluorescence intensity localized on the cytoplasm membranes comes from SAV-FITC, and it seems that the complex is loaded on the cell surface, as it would be expected. However, a control experiment performed on another set of slides shows that this is not the case. In fact, this time cells were previously incubated with the non-biotinylated α-MSH peptide and then exposed to SAV-FITC. Results are displayed in Figure 4.9. It is evident from a visual inspection that a fluorescence signal similar to the one observed in Figure 4.8 is clearly present on all the cell surfaces (A, B and C are images from three different slides). From these imaging experiments it seems that no discernible difference exists between the incubation with the biotinylated α-MSH and the non-biotinylated one. Unfortunately, a second control experiment run again on live cells shows that the very same SAV-FITC complex alone establish a non-specific interaction with the plasma membrane, resulting in significant background (Figure 4.10). This could be the

result of an hydrophobic interaction between FITC and the cell membrane, as it has been reported in literature [128].

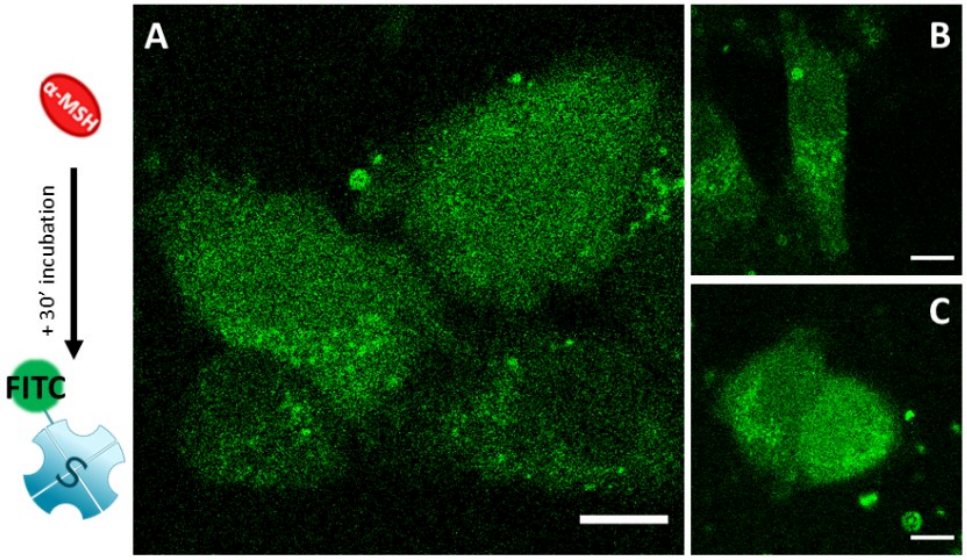

Figure 4.9: *Confocal live cell experiment with A475 melanoma cancer cells incubated 30 min with the complex SAV-FITC. In all cases (**A, B** and **C**), a significant fluorescence signal is distributed on the plasma membranes. Excitation wavelength 480 nm. Scale bar 10 µm*.

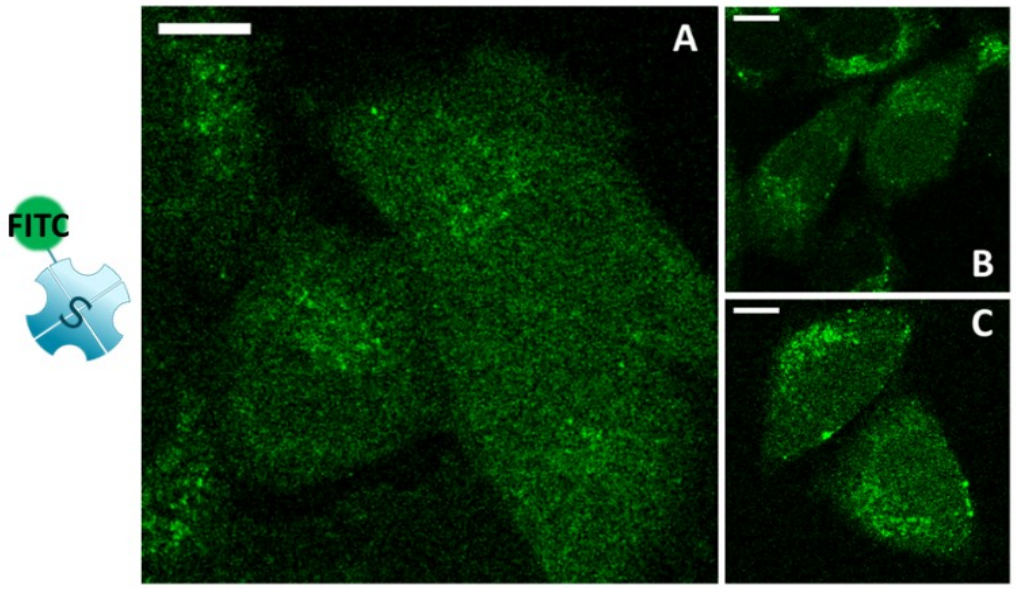

Figure 4.10: *Confocal live cell experiment with A475 melanoma cancer cells incubated 30 min with the complex SAV-FITC. In all cases (**A, B** and **C**), a significant fluorescence signal is distributed on the plasma membranes. Excitation wavelength 480 nm. Scale bar 10 µm.*

However, in order to complete the characterization of the complex with different administration methods, another experiment was performed. In this

case, cells were incubated for 30 minutes with the complex SAV-FITC pre-assembled with the biotinylated α-MSH peptide, hence removing the pre-incubation with the peptide alone. The resulting images are presented in Figure 4.11. Also in this case, the fluorescence intensity distribution is localized on the plasma membrane.

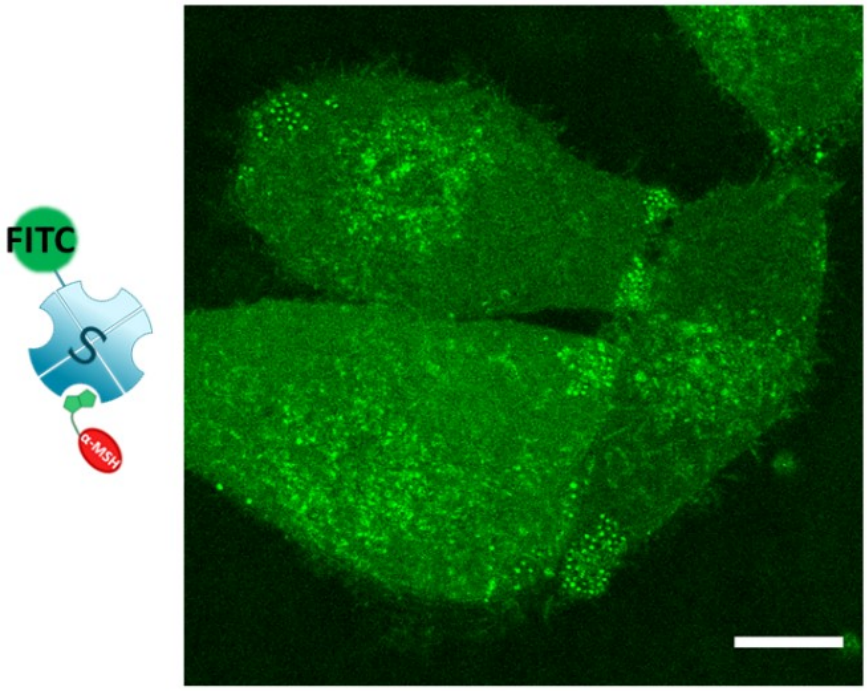

Figure 4.11: *Confocal live cell experiment with A475 melanoma cancer cells incubated 30 min with the complex SAV-FITC pre-assembled with the biotinylated α-MSH peptide. Once again, the fluorescence signal is distributed all over the cell membrane. Excitation wavelength 480 nm.*

Given the results obtained with the incubation of the solely SAV-FITC complex Figure 4.9, it could be concluded that the choice of a less hydrophobic fluorescent label would better suit this type of experiments. Moreover, the excitation of FITC at 480 nm also elicits a concomitant auto-fluorescence signal coming from the cell environment; a change of the spectral properties of the labeling molecules would be then ideal.

On the other hand, the interaction of α-MSH with MC1R and its subsequent internalization have been observed in different studies, both on human [129] and murine [130] MC1R models. Therefore, the biotinylated version of α-MSH should be able to selectively target MC1R proteins accessible on the cell membrane.

The incompatibility of the presented results with the data available in literature, suggests that there might be some underlying reasons related to the lack of targeting capabilities of the complex SAC-FIT with the biotinylated α-MSH peptide:

- The biotinylated α-MSH peptide is remarkably small (~1664 Da) compared to the SAV-FITC (60 kDa). Even if the peptide is linked to biotin, some kind of steric hindrance could impede the correct interaction of the biotin-tail with the SAV-FITC complex. In fact, it could be possible that the biotin-tail of the peptide does not protrude enough to promote the binding with SAV-FITC. One way to overcome this limitation, could be the introduction of a biotinylated antibody against MC1R, replacing the hormone peptide.

- The A375 cell line might not express enough MC1R on the plasma membrane. If the endogenous expression of MC1R in A375 is too low, another cell line could be taken in consideration, as suggested in [127]. However, the A375 cell line in use could have diverged, after several splitting passages, into a condition in which the MC1R is not over-expressed anymore. In this sense, performing an immunostaining could allow the localization of the receptors. In attempt in this direction has been made using the biotinylated α-MSH on A375 *fixed* cells, subsequently exposed to SAV-ATTO590. Results are shown in Figure 4.12. Cells have been fixed and subsequently incubated with the biotinylated α-MSH (Figure 4.12A) and SAV-ATTO590 alone (Figure 4.12B). They were then exposed to SAV-ATTO590. Unfortunately, there is no a significant difference between the two conditions, meaning that still some non-specific interaction is prevalent. Different cell fixation protocols could be tested in the future.

- The internalization of MC1R upon interaction with α-MSH might be too fast for the incubation protocols and imaging conditions applied in the presented experiments. In this case, the administration of the SAV complex should happen in a time window suitable for imaging the uptake dynamics of the system.

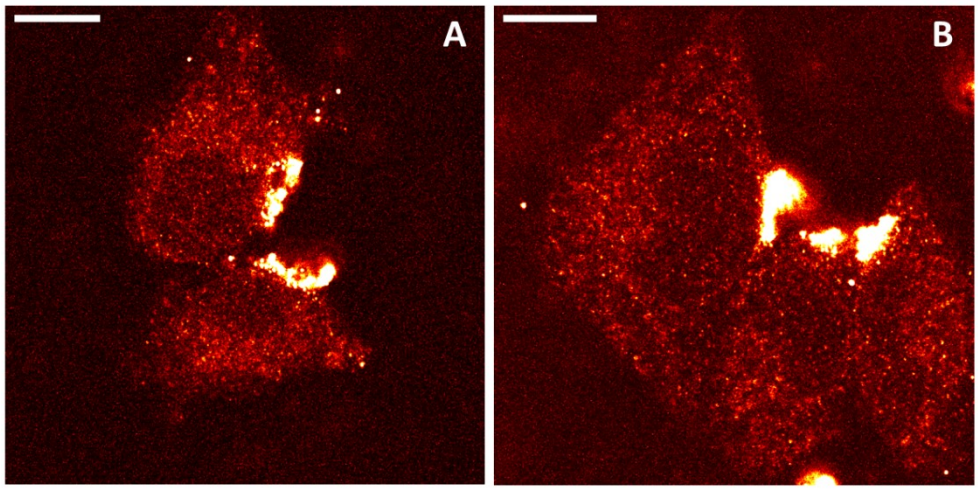

Figure 4.12: *Confocal imaging on fixed A375 melanoma cancer cells in two different experiments. (**A**) Fixed cells were incubated for 30 min with the biotinylated α-MSH and subsequently exposed to SAV-ATTO590. (**B**) Fixed cells were incubated for 30 min with SAV-ATTO590 alone. Excitation wavelength 560 nm. Scale bar 10 µm.*

All the experimental pathways listed above represent alternative solutions that can be applied in the future for the successful creation of a SAV-based complex to be used against a specific type of cancer cell. Besides, what emerges clearly from this study is that an in-depth spectroscopic characterization of a protein-based delivery system is of paramount importance for its correct functioning within a biological environment. Eventually, the outbreak of SARS-CoV-2 pandemic has considerably slowed down the experimental execution, limiting the time-window for designing new measurements.

4.2.1 Final remarks on SAV-based complexes

The strategy of using the SAV-biotin complex as a building block for creating different targeting molecules for the delivery of photosensitizer is certainly promising. As demonstrated in the previous sections, the approach offers a considerable advantage in terms of targeting flexibility, fluorescence and photosensitizer customization. SAV-based complex with the biotinylated IgG addressing protein A in *S. aureus* validates the model and sets the basis for the creation of other alike supra-molecular structures. Conversely, in the case of melanoma cancer cells, the use of a biotinylated peptide might not be a good solution since the effector molecule could not be a good anchor for the SAV-complex. However, more studies need to be carried out in order to clarify all the open question marks regarding this system.

Chapter 5

5 Hyp as an antiviral treatment

Besides bacterial infections and cancer, many of the existing human diseases are linked to viral infections. Nevertheless, despite the abundance of these conditions, few and extremely specific antiviral therapies have been approved, therapies that, more often than not, offer a slender spectrum of coverage. Unfortunately, these treatments cannot equip the global health systems with a suitable promptness and protection. In the attempt to sort out this limitation, some broad-spectrum drugs have been proposed, in response to this fast-paced world landscape [131].

A large amount of viral pathogens causing infectious diseases in a recurrent fashion is made up of membrane-envelope viruses: their infection mechanism is based on the fusion of cell and virus membranes, so that the virus can enter in the cell environment and start its replication. For this reason, strategies aimed at the targeting of this membrane fusion process are showing up as promising solutions for the creation of antivirals with a broad action [132]. Among these ones, photosensitizers represent viable antiviral tools [133]–[135].

In this scenario, a photosensitizer such as Hyp could be considered an auspicious candidate for antiviral applications, given its photosensitizing and photo-physical properties (Chapter 2, Section 2.1.1). Indeed, Hyp has already been used in studies performed on viruses, showing a remarkable viral inactivation when irradiated with light in the visible range and, in certain circumstances, also when kept in dark [136][137]. Interestingly, it has been showed that Hyp has a photosensitizing effect on viruses envelope-equipped but it is inactive when addressed against virus not having membranes [138]. Indeed, Hyp photosensitizing action dramatically depends on its aggregation state; its capabilities are quickly recovered if Hyp is bound to other structures such as membranes or proteins having proper hydrophobic clefts or pockets (Chapter 2, Section 2.1.4). Therefore, if the aim is to develop a treatment against enveloped-virus, the affinity of Hyp for the external phospholipidic structure is a crucial aspect when investigating its antiviral effectiveness.

Besides Hyp binding affinity, another key parameter to consider is the dependence of Hyp efficacy on the underlying heterogeneity of single viral

particles; these ones might present differences regarding surface and size accessibility, which might lead to a diversification in how Hyp is loaded. In facts, the need to investigate closely this variability has given to single-particle experimental approaches great momentum, in the attempt to overcome bulk information and to improve drug development against viral infections [139][140].

Hyp application in antiviral treatments has been proposed long ago [141], but little improvement has been done in the direction of knowing more about its binding affinity and loading with single viral particles. The need of addressing these questions using quantitative measurements could renovate the potential of this photosensitizing drug; it could provide a broad-spectrum effect against viruses possessing an envelope, including the severe acute respiratory syndrome coronavirus 2 (SARS-CoV-2). In fact, even if antiviral inactivation using photosensitizers has been proposed in different studies as an effective solution to stop the current pandemic [142]–[148], little experimental work has been presented so far [9].

Within this framework, the final part of this comprehensive project on photosensitizing systems regards the investigation of Hyp interaction with the viral envelope of SARS-CoV-2. More specifically, by means of an array of different techniques that include spectroscopy, fluorescence microscopy and viral assays, it has been demonstrated that Hyp is capable of inactivating the virus both when photo-activated and also in dark conditions. Since emphasis was previously put in assessing the lack of quantitative measurements on single viral particles, the experiments presented in the next sections aim to provide quantitative results on Hyp affinity for SARS-CoV-2 and its loading on single viral particles. Results regarding Hyp efficacy on the virus are discussed.

5.1 Imaging Hyp on SARS-CoV-2

Hyp comes with a hydrophobic core that is responsible for the formation of inactive aggregates once the molecule is put in water. When in this state, Hyp is incapable of inducing photosensitizing effect and the fluorescence emission is imperceptible (Chapter 2, Section 2.1.2). Since these properties are instantly recovered when Hyp binds to phospholipidic membranes, the study of the interaction of SARS-CoV-2 particles with Hyp can be carried out by looking at the

fluorescent signal emitted by the molecule (Figure 5.1a). With this purpose in mind, SARS-CoV-2 particles were fixed with formaldehyde, washed and subsequently ultra-centrifuged. In water, the interaction between Hyp and SARS-CoV-2 can be outlined as in Figure 5.1a: viral envelopes solubilize the aggregates of Hyp, in a way that restore Hyp photo-physical properties and makes SARS-CoV-2 bond with Hyp fluorescent if irradiated. Fluorescence can be appreciated in Figure 5.1b, where it has been exploited in fluorescence microscopy experiments to directly observe Hyp loading on SARS-CoV-2 particles.

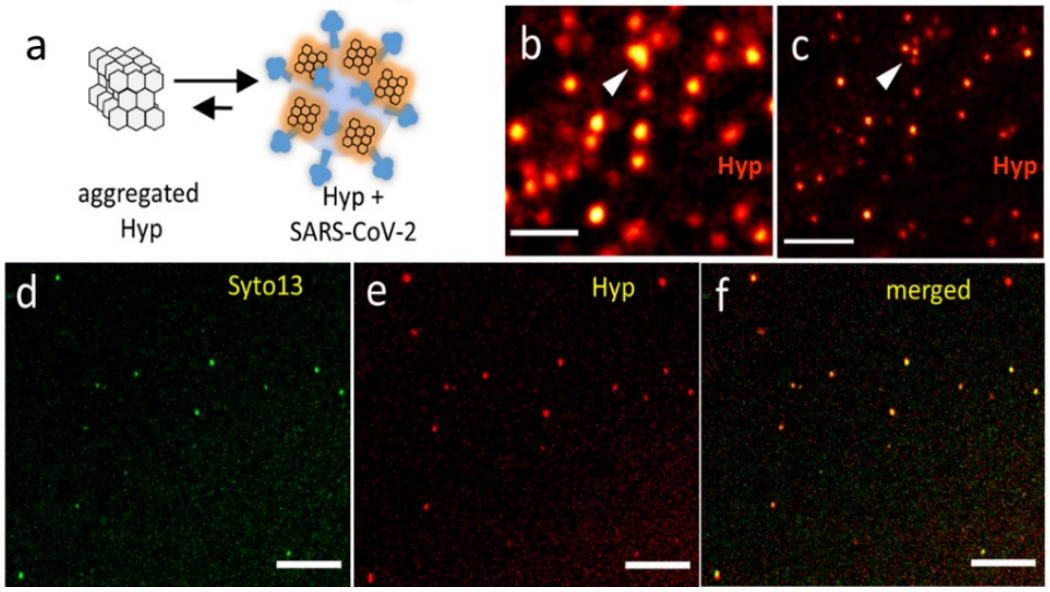

Figure 5.1: *(**a**) Cartoon representing the interaction between Hyp and SARS-CoV-2 in an aqueous environment: aggregated Hyp (left) is not able to emit any fluorescence, but the latter one is quickly recovered once Hyp bound to SARS-CoV-2 (right). (**b**) Confocal and (**c**) STED images of SARS-CoV-2 is exposed to Hyp. The arrow in each image indicates a cluster of viral particles told apart by to STED improved resolution. Scale bars 500 nm. (**d-f**) Confocal images of the same region of a SARS-CoV-2 sample labelled with Syto13 and subsequently exposed to Hyp. Syto13 (**d**, green) and Hyp (**e**, red) channels are presented separately, while the merge of the two is presented in (**f**). Scale bar 5 µm.*

One big advantage of using Hyp in biological samples for imaging experiments is that it has proved to be suitable for super-resolution applications with STED microscopy (Chapter 2, Section 2.4.1) on different studies [149][26]. Therefore, in a first set of experiments, SARS-CoV-2 particles were exposed to Hyp in a water-based buffer and seeded on a coverslip before images were taken with a confocal and a STED microscope. Images are presented in Figure 5.1b and Figure 5.1c respectively. In the first one, the bright fluorescence spots where Hyp is located

are clearly visible as diffracted-limited spots, which can be acknowledged as SARS-CoV-2 particles. However, because of the confocal limitation in spatial resolution, the particles appear as blurred objects and it is not possible to assess whether they are separated or clumped viral particles. To solve any indecision, a STED image of the same field of view is displayed (Figure 5.1c). The remarkable increase in resolution allows to tell apart the single viral particles even when clumped together. Still, the majority of them are detached from the others.

The proof that Hyp bounds to intact SARS-CoV-2 particles is provided via a co-localization experiment run using a confocal microscope. In this instance, the particles were stained using Syto13, a green fluorescent marker used for labeling nucleic acids. Subsequently, the sample was exposed to Hyp and then imaged on a glass coverslip. Images of the co-localization measurement are presented in Figure 5.1d-f, where Syto13 is represented in green and Hyp in red. Fluorescence emission for both Syto13 (Figure 5.1d) and Hyp (Figure 5.1e) localized in bright spots which, as expected, in large majority co-localize (∼80%) in the merge (Figure 5.1f) of the two channels. From this observation it can then be stated that Hyp predominantly bounds to intact SARS-CoV-2 particles; the lack of a complete co-localization might be explained with a partial staining of Styo13 or with the presence of viral shreds with which Hyp interact anyway.

5.2 Hyp affinity for SARS-CoV-2 membrane

Although fluorescence microscopy validates the integrity of the viral particles and allow to see the accumulation of Hyp, it does not provide any meaningful insight on the interaction existing between SARS-CoV-2 and the photosensitizer- However, a useful technique that can be used to investigate the bounding between the two is definitely FCS (Chapter 2, Section 2.3.1). For this purpose, SARS-CoV-2 particles were incubated with different concentrations of Hyp (in a range between 1 and 100 nM). Given that Hyp in the aggregated state is not fluorescent, the only fluorescent signal detected in this set of FCS experiments is the one of Hyp bound to the viral envelope of the particles. A representative autocorrelation curve is given Figure 5.2a. The measurement is best represented by a single slow-diffusing diffusing species, characterized by D = 2.4 ± 1.2 $\mu m^2/s$ and an hydrodynamic size of ∼150 nm, a value compatible with the expected

dimension of SARS-CoV-2 particles (the hydrodynamic radius can be calculated using Stokes-Einstein equation (Chapter 3, Section 3.3.2).

The amplitude of the FCS curves provided the overall concentration of viral particles loaded with Hyp, which resulted to be ~1 nM, with a considerable variability due to the presence of slower-diffusing envelope shreds or clumps that affected the final calculated value.

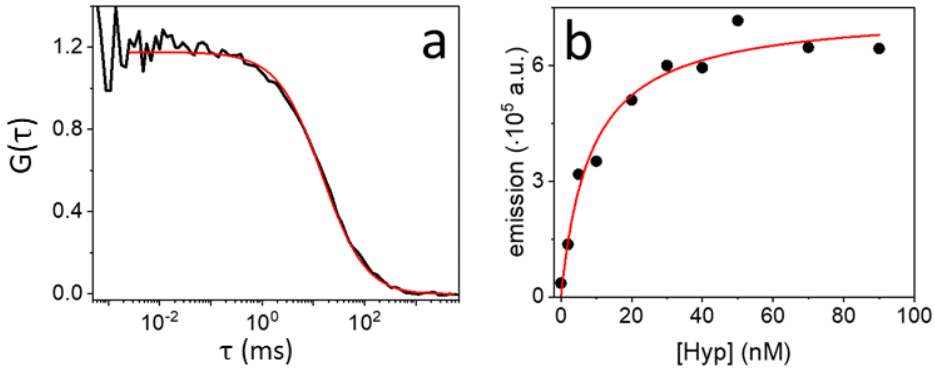

Figure 5.2: *(**a**) Representative FCS curve (black) measured on a suspension containing SARS-CoV-2 particles exposed to 5 nM of Hyp. The best fit obtained using a single diffusing species is displayed in red. (**b**) Integrated fluorescence emission of Hyp at different concentrations (black circles) but in the presence of the same quantity of viral particles (1 nM). Red line represents the fitting with a binding [148].*

Given different concentration values of Hyp while keeping a constant concentration of SARS-CoV-2 particles, the ensemble fluorescence emission of each suspension was measured using a fluorometer. The total emission was then obtained by integration of the whole spectrum, for increasing concentration of Hyp (in a range from 0 to 90 nM) and a fixed concentration of SARS-CoV-2 (~1 nM, as obtained from FCS experiments). The total emission for each Hyp concentration is displayed in Figure 5.2b. An abrupt increase in the emission of fluorescence is clearly present between 0 and 20 nM of Hyp, reaching a saturation condition around 30-40 nM. Apparently, at higher concentration of Hyp, SARS-CoV-2 particles cannot load any more molecules of the photosensitizer. Since Hyp is not fluorescent in aqueous solutions, the extra molecules form non-fluorescent aggregates in the solution. Interestingly, the molar ratio of saturation between Hyp and SARS-CoV-2 can be measured because the particles concentration is known: this one roughly corresponds to 30:1 (Hyp : SARS-CoV-2). Eventually, using a previously determined equation [150] it is possible to fit the data presented in Figure 5.2b (solid red) to quantify the value of an apparent equilibrium

dissociation constant. At a virus concentration of ∼1 nM, this constant results to be K_D = 8.5 nM.

5.2.1 Fluorescence decay of Hyp bound to membranes

As a comparison, Hyp fluorescence lifetime decay has been measured for Hyp bound on liposomes (as a reference model) and Hyp bound on the viral envelope. In Figure 5.3, the normalized fluorescence decays of Hyp in two different conditions are displayed. In red, the fluorescence decay for 5 nM Hyp bound to ∼1nM SARS-CoV-2 particles is presented, while in black it is showed the one for 10 nM Hyp bound to ∼2 nM DLPC (1,2-dilauroyl-sn-glycero-3-phosphocholine) liposomes (black).

Qualitatively, the curves presented in Figure 5.3 are quite similar, apart from a difference in the first part of the decays. In both cases, the decay curves are best fitted with a bi-exponential model, yielding two lifetimes which are reported in Table 5.1.

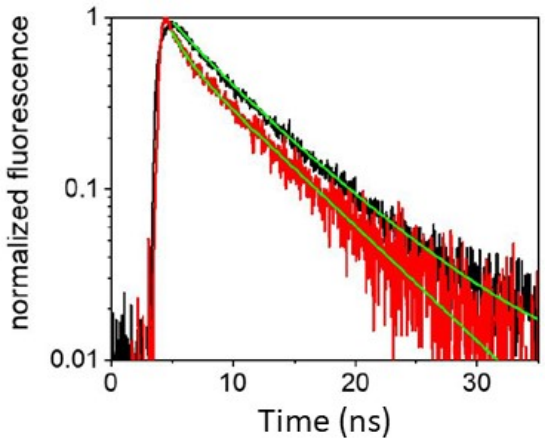

Figure 5.3: *Normalized time-resolved fluorescence decays observed for Hyp bound to DLPC liposomes (black) and SARS-CoV-2 particles (red). Green lines show the results of the fitting with a bi-exponential model for both decays.*

Comparing the obtained results, the longer lifetime (τ_2) show consistent values. On the other hand, the shorter lifetimes (τ_1) are different. The longer lifetime components are associated to a major population of Hyp molecules (larger amplitudes, Table 5.1) found in a local environment less polar than water (as a reference, τ = 5.5 ns in DMSO and τ = 6.0 ns in acetone [151]). Hence, the Hyp surroundings in both cases can be identified as a phospholipidic bilayer.

	τ_1 (ns)	τ_2 (ns)
Hyp + SARS-CoV-2	1.2 ± 0.1	6.3 ± 0.3
Hyp + DLPC	2.3 ± 0.5	6.8 ± 0.4

Table 5.1: *Fluorescence decay times yielded from the bi-exponential model used to fit the experimental data. For Hyp bound with SARS-CoV-2, τ_1 and τ_2 are associated with amplitudes 25% and 75% respectively. For the case of Hyp loaded on DLPC liposomes, τ_1 and τ_2 come with amplitudes 10% and 90% respectively.*

In conclusion, the results obtained from the measurement of Hyp fluorescence decay time strongly support the hypothesis that the viral membrane is the main target of Hyp, even though other binding sites (i.e. such as spike proteins) cannot be excluded a priori.

5.3 Hyp distribution on SARS-CoV-2 particles

Given the fact that Hyp fluorescence emission comes only from viral particles bound with it, it can be stated that the emission coming from a single viral particle is relatively proportional to the number of Hyp molecules loaded on that particle. This means that, in principle, relative differences on the number of Hyp molecules bound with a single viral particle can be collected throughout fluorescence microscopy measurements. With the aim of quantifying this difference, a set of confocal measurements were run. SARS-CoV-2 particles at a constant concentration ($\sim$1nM, the same of the FCS measurements) of SARS-CoV-2 particles was first incubated with Hyp at various concentrations (ranging from 5 to 90 nM). The particles so exposed to the photosensitizer where then seeded on a coverslip, without washing. Before collecting any image, the same amount of PBS was added to all the samples, in order to reach a sample volume suitable for and optimal visualization at the confocal microscope. In every case, the ratio Hyp : SarS-CoV-2 was preserved. A representative image is displayed in Figure 5.4. In order to extract the emission intensity from the single SARS-CoV-2 particles, images were analyzed following a simple routine described in the following section. Once obtained the intensity of each particle for every Hyp concentration investigated, these values have been binned for visualizing the probability distribution displayed in Figure 5.4b.

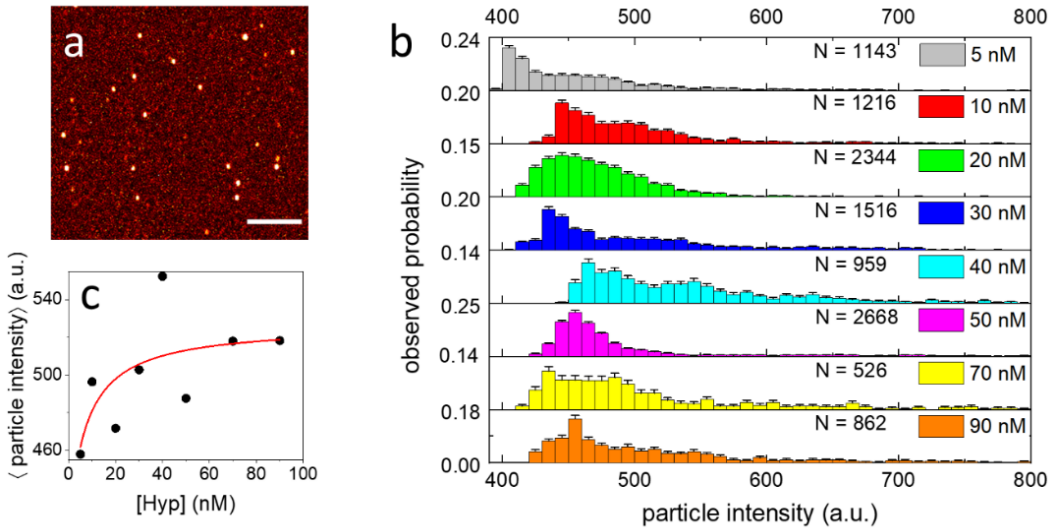

Figure 5.4: *(**a**) Representative image of SARS-CoV-2 particles loaded with Hyp imaged for the analysis of single particle intensity. Scale bar 5 µm. (**b**) Observed probability distributions of single viral particle fluorescence intensity obtained for 1 nM SARS-CoV-2 particles exposed to 5 nM (grey), 10 nM (red), 20 nM (green), 30 nM (blue), 40 nM (cyan), 50 nM (magenta), 70 nM (yellow), 90 nM (orange). N is the number of analyzed particles for each distribution. Bin width = 10 a. u. (**c**) Average values of single viral particle fluorescence intensity measured at increasing Hyp concentration. In red, the result of the fitting with the binding model used in Figure 5.2b is shown in red. Hyp concentration refers to the quantity SARS-CoV-2 was exposed with.*

Interestingly, the intensity distribution for all the Hyp concentrations investigated shows a majority of viral particles presenting values between 430 and 500 a.u., with a non-negligible tail at bigger intensity values. In addition to this, it should be given that it is not possible to discriminate SARS-CoV-2 particles presenting an intensity value lower than ~400 a.u., as at these intensity values it is really difficult to tell them apart from the background.

At the same time, particles just above this threshold and found with an intensity between 400 and 430 a.u. are more susceptible to image-to-image variability. Looking at the intensity values of Figure 5.4b, it is quite difficult to individuate a clear trend since data do not present a defined shape. However, this behavior is indicative of a major heterogeneity of the Hyp loading on the ensemble of viral particles. This inherent heterogeneity might be due to the differences existing from particle to particle: trivially, the extent of accessible membrane surface might not be the same for all SARS-CoV-2 particles and this could cause significant

differences in Hyp accumulation. Concomitantly, this diversity could be also an effect of the stochastic nature of binding.

This method for visualizing difference in Hyp loading on viral particles might also suffer from sensitivity limitations when Hyp concentration is very low (< 10 nM). Besides the aforementioned problem of having particles that are indistinguishable from the background, in case of low Hyp concentrations an important part of SARS-CoV-2 is likely to remained unlabeled and hence undetectable with the fluorescence microscope. A more accurate sampling of the fluorescence intensity varying with Hyp concentration should include methods which allow to detect also unlabeled particles, such as correlative light and electron microscopy [152].

However, in Figure 5.4c the average values of single particle intensity for each Hyp concentrations are plotted. From these measurements, a trend can be found, as there clearly is an increase in intensity at growing of Hyp concentration. And more interestingly, a fit of these values using the same binding model of Figure 5.2b leads to an apparent dissociation constant of K_D = 7 nM (the fit for the single molecules intensity is plotted in red in Figure 5.4c). This result is compatible with the one obtained from fluorescence emission measurements. The conclusion of this evaluation is particularly significant, since Hyp loading information at the level of the single viral particle are not accessible via performing ensemble experiments.

5.3.1 Particle intensity analysis

Since the fluorescence intensity values from different Hyp concentrations should be comparable, images acquired for the data showed Figure 5.4 were collected using always the same parameters and analyzed running the same analysis. In order to have a good estimation of the average intensity value for the single particles, for each Hyp concentration a set of 8-10 images was collected. Particle analysis was performed using the image analysis software ImageJ, following a routine that allowed to draw the intensity values for all the particles present in the field of view of a specific image.

A schematic visualization of the image analysis routine is presented in Figure 5.5; a crop of an original image at Hyp 50 nM is used as a sample. Before setting a threshold for analyzing the single viral particles, it is necessary to filter the image using a Gaussian blur of σ = 180 nm. This method helps removing uncorrelated

background noise before setting intensity threshold values. An optimal setting of the threshold is necessary to better discriminate the viral fluorescent particles.

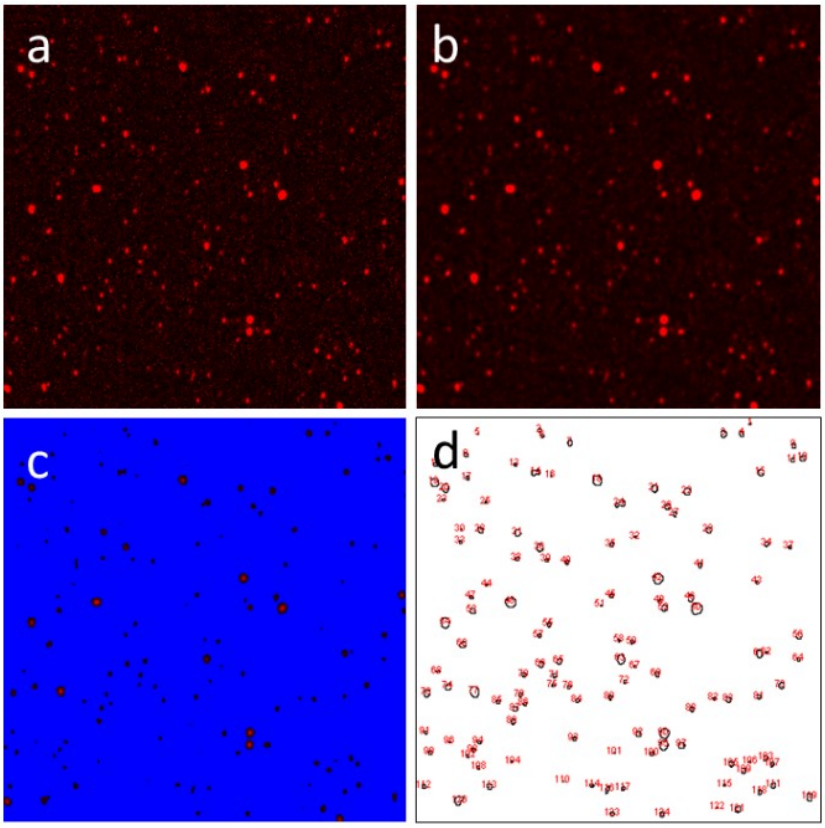

Figure 5.5: *(**a**) Image crop of SARS-CoV-2 particles exposed to 50 nM Hyp, used as a sample for the image analysis routine explained below. (**b**) Image (**a**) after the application of a Gaussian filter for reducing the background noise before the application of the threshold. (**c**) Mask of the threshold selected for (**b**). In general, the intensity values considered for the particles analysis were above 400-420 a.u. This allows to not include dim particles in the analysis, likely to be only viral shreds. Bright spots reaching saturation intensity levels were discarded manually after the selection with the analyze particle tool (**d**). The last one generates an outline for each particles included in the intensity analysis.*

After that, a threshold on the intensity was set, so that the only particles considered in the analysis were the ones possessing an intensity value above 400-420 a.u. and a minimum area of 8-10 pixels.

The selection of the elements that met these conditions was made through a particle analyzer tool. In a few cases, parts of the images that resulted clearly out of focus, e.g. due to irregularities of the glass surface, were excluded. Then, a particle analyzer tool was applied to automatically recognize particles having minimum intensity above a threshold value (400-420 a.u.) and a minimum area

(8-10 pixels). Results of the analysis were visually inspected and a few particles (< 1%) showing unrealistic features, e.g. corresponding to aggregates, were excluded. Finally, the mean intensity value of each of the selected particles was stored and used to build the distributions displayed in Figure 5.4b and calculate the average intensity value for single particles of Figure 5.4c.

5.4 Efficacy of Hyp against SARS-CoV-2

Even if microscopy measurements sheds some light on the molecular distribution of Hyp on the viral particles, they are definitely not sufficient for assessing the therapeutic value of the photosensitizer to inactivate SARS-CoV-2. Indeed, in order to be able to see if the activation of Hyp has remarkable effect on reducing the infectivity of the viral particles, it is necessary to perform crucial viability measurements in cell culture. In this last set of experiments, SARS-CoV-2 particles were incubated with Hyp at different concentrations (3, 30 and 300 nM). The samples so prepared were then irradiated with blue light or kept in the dark; in this way, it was possible to discriminate the inactivation between Hyp dark-toxicity and its photosensitizing action (activated with blue light). After this procedure, viral particles were diluted and incubated with Vero E6 cells.

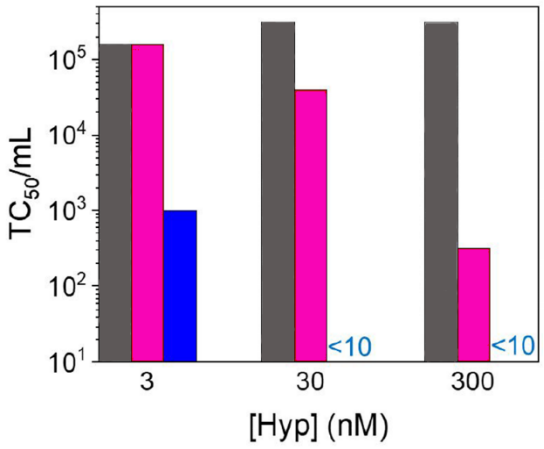

Figure 5.6: *Viral titer ($TCID_{50}$/mL) on Vero E6 cell infected with SARS-CoV-2 viruses previously exposed at increasing Hyp concentration. Samples were subject to two different light irradiation mode: dark (magenta) and irradiated with 20 J/cm^2 blue light (blue). As a reference, Vero E6 infected with SARS-CoV-2 not previously treated with Hyp are shown in dark grey.*

In this case, the parameter indicative of the infecting activity of the virus is called viral titer, which gives a quantification of the viral infected cells. It is expressed in terms of 50% tissue infective dose per milliliter ($TCID_{50}$/mL) and it corresponds to the dilution at which cell viability is reduced by 50% at the moment of the measurement. A summary of these cell viability is presented in Figure 5.6.

Looking at the results obtained, it is evident that an impressive decrease in viral infectivity exists when SARS-CoV-2 particles are treated with 300 nM and 30 nM Hyp irradiated ($TCID_{50}$/mL from $10^{5.5}$ to $< 10^{1}$). Incredibly, a clear antiviral action of the photosensitizer is observed also at 3 nM Hyp: upon light exposure, the reduction of the viral titer is about 2.2-log compared to virus not previously treated ($TCID_{50}$/mL from $10^{5.2}$ to 10^{3}). These results are extremely encouraging since they demonstrate that even low concentrations of photo-activated Hyp are enough to induce a significant reduce SARS-CoV-2 viral activity. Hyp induced a small amount of antiviral activity also for experiments run in dark conditions, even if with much lesser effect than in the photo-excited cases. Most importantly, no toxicity has been observed in control Vero E6 cells that were exposed to Hyp or DMSO, without viral particles and under dark conditions, confirming that cells are not directly damaged by Hyp or the small quantity of DMSO used to add Hyp in the cell medium.

Comparing the outcomes of these experiments with other photo-inactivation studies recently presented and in which methylene blue and radachlorin were used as photosensitizing agents [9]; the much lower Hyp concentration needed to inactivate the SARS-CoV-2 proves that Hyp can be potentially used as an antiviral agent effectively.

Hence, it is possible to strongly state the photo-activation of Hyp bound to viral particles is likely to induce a broad deterioration caused by reactive oxygen species as already observed in similar studies [133][135]. However, since this photosensitizing action is activated upon irradiation with light, the photo-damage cannot be induced under dark conditions; this suggests that there might be a second underlying process, complementary to the photo-activation, which is responsible of the decrease in viral activity when light is not presence. It could be that, once embedded in the viral envelope, Hyp acts on the stability of the lipid bilayer affecting its fluidity [153][154].

5.5 Final considerations on Hyp and SARS-CoV-2

The results obtained on the previously presented set of measurements demonstrate that Hyp binds to the membrane envelope of SARS-CoV-2 particles with a strong affinity (nanomolar K_D). The estimate of such dissociation constant also allowed to quantify the number of molecules per single virus. Although a more precise quantification on this number is limited by the heterogeneity among single viral particles, a maximum of 30 Hyp can be loaded on a single viral particle. From a therapeutic point of view, the photo-induced reduction of SARS-CoV-2 infectivity by Hyp on Vero E6 is remarkable. Once again, it demonstrates that Hyp has great potential for antiviral application. In addition to the photo-induced damage, the evidence of an existing complementary effect which reduced the viral activity under dark conditions suggest a multiple mechanism of action of Hyp.

More generally, these results highlight how the spectroscopic properties of Hyp can be successfully exploited for a quantitative investigation of its interaction with enveloped viruses, both at the bulk and single viral particles level. This constitutes an essential requirement to frame the minimal conditions necessary to investigate the antiviral mechanisms of this drug: an approach encompassing all the previously presented assays is indeed crucial for the development of more effective treatments. On this line of thought, further experiments will be run in order to correlate the amount of loaded Hyp molecules with the induced photo-damage on single viruses. Additionally, the effects of Hyp on the membrane fluidity and its structural integrity will be evaluated as potential complementary mechanisms of antiviral activity. The fact that Hyp antiviral activity relies primarily on the presence of the viral envelope, its mechanism could be exploited in a broad-spectrum fashion, against different viruses but always provided with an outer membrane.

Chapter 6

6 Conclusions and final remarks

This thesis work presented the development of different protein-based delivery systems specifically designed to transport photosensitizers (i.e. Hyp and EITC) on different biological targets. The complexes have been designed and subsequently characterized with a selection of techniques, necessary to assess reliable and repeatable results. From spectroscopy and fluorescence microscopy, to cell viability measurements, this comprehensive study aims to show that a completed biophysical description of such molecular carriers cannot prescind from a basic experimental toolkit made up of the aforementioned complementary approaches. Among these techniques, fluorescence microscopy is essential for investigating the correct functioning of the delivery systems close to natural, physiological environments.

The assembly of NP7 with Hyp and the subsequent introduction of imaging capabilities in the complex has proven an efficient PS-delivery system can rise from protein naturally endowed with targeting capabilities. Transport of Hyp on different model membranes have been studied with FCS measurements, demonstrating that the protein serves as an effective carrier of Hyp towards negatively charged membranes. NP7 also proved to be a useful imaging agent when labelled with ATTO647N, with great usability for microscopy experiments. However, to obtain a larger population of labelled NP7 (according to the results of Chapter 2, there is one ATTO647N molecule every two NP7 proteins) the labelling efficiency can be further improved. Preliminary results have been obtained in dual-color STED experiments on *E. coli* bacterial cells, combining NP7-ATTO647N with Nile Red for staining the external bacterial envelope. However encouraging, the images presented show bacterial cells saturated with Nile Red and displaying a weak ATTO647N signal on the outside: a new set of imaging experiments (on liposomes as well) must be considered for the future, for better appreciate the distribution of NP7-ATO647N on real biological targets.

In a further step, the introduction of a PS-delivery system highly customizable and presenting all-in-one targeting, imaging and photosensitizing properties has been materialized in a SAV-biotin based complex. Through different experiments,

it has been demonstrated that the direct binding between the protein scaffold and the photosensitizer EITC does not hamper the further introduction of up to four biotinylated molecules, so that a multi-functional delivery system can be designed using a modular approach. With the aim of applying it to *E.coli* bacterial cells, SAV-EITC was combined with a biotinylated IgG specific for protein A, expressed on the outer bacterial envelope. Its effectiveness in terms of cell photo-inactivation have been demonstrated by means of FCS measurements, super-resolution imaging and bioavailability assays respectively. The successful results obtained in bacteria have encouraged the further customization of such complex for addressing melanoma cancer cells. The targeted protein was the membrane receptor MC1R, which naturally interact with the small hormone α-MSH. The biotinylated version of α-MSH has been exploited to functionalize the SAV carrier, thus selectively targeting the melanoma cells. Unfortunately, even after implementing different administrations protocols and sample preparations, it has not been possible to present a functional delivery system. It could be argued that the prior and thorough characterization of the biot-α-MSH-SAV complex were not sufficient for the success of the imaging experiments. However, as already discussed in the final section of Chapter 3, the lack of progress could also be attributable to inherent constrains of the biophysical system, such as the mentioned steric hindrance between the peptide and SAV, or to a poor expression of the MC1R on the cell surface. Even so, the missed opportunities due to suspension of activities because of Covid-19 outbreak have considerably slowed down the experimental troubleshooting of the delivery system. Nevertheless, the results already obtained on *E.coli* fully support possibility of creating a SAV-based system against cancer cells. A lot of future experimental work needs to be carried out.

Eventually, the study carried out on SARS-CoV-2 have demonstrated the efficacy of Hyp as an adjuvant treatment to be potentially combined with other therapies against the infection. Its biophysical characterization on the viral particles gave access to important considerations on Hyp affinity for envelopes viruses. The strength of using Hyp as a broad-spectrum drug for treating viral infections lies in its efficacy in binding membrane envelopes, hence suggesting its usability towards viral particles sharing the same structural features. The study aims also to stress the importance of better understanding the molecular mechanisms between the photosensitizer and the outer envelope, at the level of the single viral particle.

In conclusion, fluorescence microscopy proves to be a fundamental tool for the observation of photosensitizers in a physiological environment; when endowed

with fluorescence properties, protein scaffold can as well serve as label to localize the PS-carrier without eliciting any photosensitizing effect. Besides, the introduction of fluorescent probes suitable for super-resolution microscopy gives access to more information on the distribution of such systems on the target. However, targeted selectivity via microscopy validation is not enough to assess the effective therapeutic functioning of the PS-carrier. It is for this reason that different approaches must be combined, to provide a capillary knowledge of the system under investigation and, in case, improve its design.

Acknowledgements and thanks

I would like to thank Prof. Stefania Abbruzzetti and Dr. Paolo Bianchini for the support and supervision they provided me along the past three years. Nothing would have been possible without their attention. I am deeply thankful also to Prof. Alberto Diaspro who gave me the priceless opportunity of carrying out my research project in his research line (Nanoscopy) at the Italian Institute of Technology in Genoa. This incredible experience helped me to grow both scientifically and personally. I am extremely grateful to Andrea Mussini, Dr. Pietro Delcanale and Prof. Cristiano Viappiani for all the expertise and work they shared with me and that largely contributed to this project.

In terms of life, this adventure would have not been the same without the amazing people I had the chance to meet and work with in the lab. Among them, my heartfelt thanks go to Alessandro Z. and Alessandro R., who have always believed in me and in my potential even in my lowest moments. I want to thank also the newest colleague and friend Matteo, who helped me to stay calm and persistent on my work. My gratitude also flies to Aymeric, amazing human being and passionate scientist who shared with me his wisdom in front of the wonderful sunset of Santa Monica.

I will always have a debt of gratitude for my father and brothers, their love and attention helped me navigate through these years away from home.

Eventually, my wholehearted gratitude goes to the two persons who radically changed my life. I want to thank Artemi for the unconditional strength, support and love she gave me since the very beginning of our alliance. She respected my inner nature and taught me how to make it blossom.

Finally, I want to thank Marco for being the most unexpected and yet most wonderful person I would ever wish to have by my side. His unshakable love and care made arriving at these last words possible. I cannot wait for the next adventure.

7 Bibliography

[1] M. D. Daniell and J. S. Hill, “A History of Photodynamic Therapy,” *Australian and New Zealand Journal of Surgery*, vol. 61, no. 5. pp. 340–348, 1991.

[2] L. B. Josefsen and R. W. Boyle, “Photodynamic Therapy and the Development of Metal-Based Photosensitizers,” *Met. Based. Drugs*, vol. 2008, 2008.

[3] R. Bonnett, “Photosensitizers of the Porphyrin and Phthalocyanine Series for Photodynamic Therapy,” vol. 13, no. 3, pp. 1–12, 1987.

[4] G. M. F. Calixto, J. Bernegossi, L. M. De Freitas, C. R. Fontana, M. Chorilli, and A. M. Grumezescu, “Nanotechnology-based drug delivery systems for photodynamic therapy of cancer: A review,” *Molecules*, vol. 21, no. 3. MDPI AG, 01-Mar-2016.

[5] Y. Liu, R. Qin, S. A. J Zaat, E. Breukink, and M. Heger, “Antibacterial photodynamic therapy: overview of a promising approach to fight antibiotic-resistant bacterial infections,” *J. Clin. Transl. Res.*, vol. 1, no. 3, pp. 140–167, 2015.

[6] Pr. Shankar, “Book review: Tackling drug-resistant infections globally,” *Arch. Pharm. Pract.*, vol. 7, no. 3, p. 110, 2016.

[7] S. Rywkin *et al.*, “New Phthalocyanines for Photodynamic Virus Inactivation in Red Blood Cell Concentrates,” *Photochem. Photobiol.*, vol. 60, no. 2, pp. 165–170, 1994.

[8] L. Nikolaeva-Glomb *et al.*, “Photodynamic effect of some phthalocyanines on enveloped and naked viruses,” *Acta Virol.*, vol. 61, no. 3, pp. 341–346, 2017.

[9] V. A. Svyatchenko, S. D. Nikonov, A. P. Mayorov, M. L. Gelfond, and V. B. Loktev, “Antiviral photodynamic therapy : Inactivation and inhibition of SARS-CoV-2 in vitro using methylene blue and Radachlorin,” no. January, 2020.

[10] S. Kwiatkowski *et al.*, “Photodynamic therapy – mechanisms, photosensitizers and combinations,” *Biomedicine and Pharmacotherapy*, vol. 106. Elsevier Masson SAS, pp. 1098–1107, Oct-2018.

[11] A. F. Dos Santos, D. R. Q. De Almeida, L. F. Terra, M. S. Baptista, and L. Labriola, “Photodynamic therapy in cancer treatment - an update review,” *J. Cancer Metastasis Treat.*, vol. 2019, 2019.

[12] P. M. R. Cruz, H. Mo, W. J. McConathy, N. Sabnis, and A. G. Lacko, “The role of cholesterol metabolism and cholesterol transport in carcinogenesis: A review of scientific findings, relevant to future cancer therapeutics,” *Front. Pharmacol.*, vol. 4 SEP, no. September, pp. 1–7, 2013.

[13] R. L. Lipson, E. J. Baldes, and M. J. Gray, “Hematoporphyrin derivative for detection and management of cancer,” *Cancer*, vol. 20, no. 12, pp. 2255–2257, Dec. 1967.

[14] P. Bianchini *et al.*, “Hypericin-Apomyoglobin: An Enhanced Photosensitizer Complex for the Treatment of Tumor Cells,” *Biomacromolecules*, vol. 20, no. 5, pp. 2024–2033, 2019.

[15] M. Cozzolino *et al.*, “Enhanced photosensitizing properties of protein bound curcumin,” *Life Sci.*, vol. 233, no. July, p. 116710, 2019.

[16] C.-T. Chen, C.-P. Chen, J.-C. Yang, and T. Tsai, “Liposome-Encapsulated Photosensitizers

Against Bacteria," *Recent Pat. Antiinfect. Drug Discov.*, vol. 8, no. 2, pp. 100–107, 2013.

[17] C. S. Jin and G. Zheng, "Liposomal nanostructures for photosensitizer delivery," *Lasers Surg. Med.*, vol. 43, no. 7, pp. 734–748, 2011.

[18] S. Ghosh, K. A. Carter, and J. F. Lovell, "Liposomal Formulations of Photosensitizers," *Physiol. Behav.*, vol. 176, no. 1, pp. 139–148, 2019.

[19] J. Comas-Barceló *et al.*, "A self-assembled nanostructured material with photosensitising properties," *RSC Adv.*, vol. 3, no. 39, pp. 17874–17879, 2013.

[20] P. Delcanale *et al.*, "Zinc-Substituted Myoglobin Is a Naturally Occurring Photo-antimicrobial Agent with Potential Applications in Food Decontamination," *J. Agric. Food Chem.*, vol. 64, no. 45, pp. 8633–8639, 2016.

[21] M. Cozzolino *et al.*, "Apomyoglobin is an efficient carrier for zinc phthalocyanine in photodynamic therapy of tumors," *Biophys. Chem.*, vol. 253, no. June, p. 106228, 2019.

[22] B. Rodríguez-Amigo *et al.*, "The complex of hypericin with β-lactoglobulin has antimicrobial activity with potential applications in dairy industry," *J. Dairy Sci.*, vol. 98, no. 1, pp. 89–94, 2015.

[23] M. L. Embleton, S. P. Nair, B. D. Cookson, and M. Wilson, "Selective lethal photosensitization of methicillin-resistant Staphylococcus aureus using an IgG-in (IV) chlorin e6 conjugate," *J. Antimicrob. Chemother.*, vol. 50, no. 6, pp. 857–864, 2002.

[24] J. P. Celli *et al.*, "Imaging and Photodynamic Therapy: Mechanisms, Monitoring and Optimization," *Early Hum. Dev.*, vol. 83, no. 4, pp. 255–262, 2007.

[25] H. Abrahamse and M. R. Hamblin, "New photosensitizers for photodynamic therapy," *Biochem. J.*, vol. 473, no. 4, pp. 347–364, 2017.

[26] D. Pezzuoli *et al.*, "Serum albumins are efficient delivery systems for the photosensitizer hypericin in photosensitization-based treatments against Staphylococcus aureus," *Food Control*, vol. 94, no. July, pp. 254–262, 2018.

[27] P. Bianchini, C. Peres, M. Oneto, S. Galiani, G. Vicidomini, and A. Diaspro, "STED nanoscopy: a glimpse into the future," *Cell Tissue Res.*, vol. 360, no. 1, pp. 143–150, 2015.

[28] E. Betzig, S. W. Hell, and W. Moerner, "The Nobel Prize in Chemistry," *Nobeprize.org*, 2014. [Online]. Available: https://www.nobelprize.org/prizes/chemistry/2014/summary/.

[29] A. P. Castano, T. N. Demidova, and M. R. Hamblin, "Mechanisms in photodynamic therapy: Part one - Photosensitizers, photochemistry and cellular localization," *Photodiagnosis and Photodynamic Therapy*, vol. 1, no. 4. Elsevier, pp. 279–293, 2004.

[30] T. Grune, L. O. Klotz, J. Gieche, M. Rudeck, and H. Sies, "Protein oxidation and proteolysis by the nonradical oxidants singlet oxygen or peroxynitrite," *Free Radic. Biol. Med.*, vol. 30, no. 11, pp. 1243–1253, 2001.

[31] W. Adam, C. R. Saha-Möller, and A. Schönberger, "Photooxiation of 8-oxo-7,8-dihydro-2'-deoxyguanosine by thermally generated triplet-excited ketones from 3-(hydroxymethyl)-3,4,4-trimethyl-1,2-dioxetane and comparison with type I and type II photosensitizers," *J. Am. Chem. Soc.*, vol. 118, no. 39, pp. 9233–9238, 1996.

[32] B. Epe, "DNA damage spectra induced by photosensitization," *Photochem. Photobiol. Sci.*, vol. 11, no. 1, pp. 98–106, 2012.

[33] J. Ghorbani, D. Rahban, S. Aghamiri, A. Teymouri, and A. Bahador, “Photosensitizers in antibacterial photodynamic therapy: An overview,” *Laser Ther.*, vol. 27, no. 4, pp. 293–302, 2018.

[34] et al. Agostinis P, Berg K, Cengel K., “Photodynamic Therapy of Cancer: An Update,” *Ca Cancer J Clin*, vol. 61, no. April, pp. 250–281, 2017.

[35] E. Cló, J. W. Snyder, P. R. Ogilby, and K. V. Gothelf, “Control and selectivity of photosensitized singlet oxygen production: Challenges in complex biological systems,” *ChemBioChem*, vol. 8, no. 5, pp. 475–481, 2007.

[36] A. E. O’Connor, W. M. Gallagher, and A. T. Byrne, “Porphyrin and nonporphyrin photosensitizers in oncology: Preclinical and clinical advances in photodynamic therapy,” *Photochemistry and Photobiology*, vol. 85, no. 5. John Wiley & Sons, Ltd, pp. 1053–1074, 01-Sep-2009.

[37] M. A. Calin and S. V. Parasca, “Photodynamic therapy in oncology,” in *Journal of Optoelectronics and Advanced Materials*, 2006, vol. 8, no. 3, pp. 1173–1179.

[38] A. Juzeniene, Q. Peng, and J. Moan, “Milestones in the development of photodynamic therapy and fluorescence diagnosis †,” vol. 1332, 2007.

[39] P. Agostinis, A. Vantieghem, W. Merlevede, and P. A. M. De Witte, “Hypericin in cancer treatment: More light on the way,” *Int. J. Biochem. Cell Biol.*, vol. 34, no. 3, pp. 221–241, 2002.

[40] N. Durán and P.-S. Song, “Hypericin and its photodynamic action,” *Photochem. Photobiol.*, vol. 58, no. 6, pp. 895–900, 1986.

[41] T. J. Deerinck *et al.*, “Fluorescence photooxidation with eosin: A method for high resolution immunolocalization and in situ hybridization detection for light and electron microscopy,” *J. Cell Biol.*, vol. 126, no. 4, pp. 901–910, 1994.

[42] E. Gandin, Y. Lion, and A. Van de Vorst, “Quantum Yield of Singlet Oxygen Production By Xanthene Derivatives,” *Photochem. Photobiol.*, vol. 37, no. 3, pp. 271–278, 1983.

[43] G. R. Fleming, A. W. E. Knight, J. M. Morris, R. J. S. Morrison, and G. W. Robinson, “Picosecond Fluorescence Studies of Xanthene Dyes,” *J. Am. Chem. Soc.*, vol. 99, no. 13, pp. 4306–4311, 1977.

[44] J. P. M. L. Rolim *et al.*, “The antimicrobial activity of photodynamic therapy against Streptococcus mutans using different photosensitizers,” *J. Photochem. Photobiol. B Biol.*, vol. 106, no. 1, pp. 40–46, 2012.

[45] K. Marinic *et al.*, “Repeated exposures to blue light-activated eosin Y enhance inactivation of E. faecalis biofilms, in vitro,” *Photodiagnosis Photodyn. Ther.*, vol. 12, no. 3, pp. 393–400, 2015.

[46] C. Hally, P. Delcanale, S. Nonell, C. Viappiani, and S. Abbruzzetti, “Photosensitizing proteins for antibacterial photodynamic inactivation,” *Transl. Biophotonics*, vol. 2, no. 1–2, pp. 1–11, 2020.

[47] P. Delcanale *et al.*, “Subdiffraction localization of a nanostructured photosensitizer in bacterial cells,” *Sci. Rep.*, vol. 5, pp. 1–9, 2015.

[48] J. D. Meyers, C. W. Reserve, S. Margevicius, C. W. Reserve, and C. W. Reserve, “Peptide-Targeted Gold Nanoparticles for Photodynamic Therapy of Brain Cancer,” vol. 32, no. 4,

pp. 448–457, 2015.

[49] H. Montaseri, C. A. Kruger, and H. Abrahamse, “Targeted photodynamic therapy using alloyed nanoparticle-conjugated 5-aminolevulinic acid for breast cancer,” *Pharmaceutics*, vol. 13, no. 9, 2021.

[50] N. W. N. Simelane, C. A. Kruger, and H. Abrahamse, “Targeted nanoparticle photodynamic diagnosis and therapy of colorectal cancer,” *Int. J. Mol. Sci.*, vol. 22, no. 18, 2021.

[51] T. Stuchinskaya, M. Moreno, M. J. Cook, D. R. Edwards, and D. A. Russell, “Targeted photodynamic therapy of breast cancer cells using antibody-phthalocyanine-gold nanoparticle conjugates,” *Photochem. Photobiol. Sci.*, vol. 10, no. 5, pp. 822–831, 2011.

[52] S. W. Hell, “Nanoscopy with Focused Light (Nobel Lecture),” *Angew. Chemie - Int. Ed.*, vol. 54, no. 28, pp. 8054–8066, 2015.

[53] B. N. G. Giepmans, S. R. Adams, M. H. Ellisman, and R. Y. Tsien, “The fluorescent toolbox for assessing protein location and function,” *Science (80-.).*, vol. 312, no. 5771, pp. 217–224, 2006.

[54] L. Schermelleh *et al.*, “Super-resolution microscopy demystified,” *Nat. Cell Biol.*, vol. 21, no. 1, pp. 72–84, 2019.

[55] S. J. Sahl, S. W. Hell, and S. Jakobs, “Fluorescence nanoscopy in cell biology,” *Nat. Rev. Mol. Cell Biol.*, vol. 18, no. 11, pp. 685–701, 2017.

[56] J. Vangindertael, R. Camacho, W. Sempels, H. Mizuno, P. Dedecker, and K. P. F. Janssen, “An introduction to optical super-resolution microscopy for the adventurous biologist,” *Methods Appl. Fluoresc.*, vol. 6, no. 2, 2018.

[57] K. Carlsson, “Imaging Physics,” *Prim. Diagnostic Imaging*, pp. 690–746, 2011.

[58] C. J. R. Sheppard, “The development of microscopy for super-resolution: Confocal microscopy, and image scanning microscopy,” *Appl. Sci.*, vol. 11, no. 19, 2021.

[59] S. R. S. Lord Rayleigh, “On the theory of optical images, with special reference to the microscope,” no. 2, 1874.

[60] E. Abbe, “Bieträge zur Theorie des Mikroskops und der mikroskopischen Wahrnehmung.”

[61] M. Chalfie, Y. Tu, G. Euskirchen, W. W. Ward, and D. C. Prasher, “Green fluorescent protein as a marker for gene expression,” *Science (80-.).*, vol. 263, no. 5148, pp. 802–805, 1994.

[62] M. A. Hink *et al.*, “Structural dynamics of green fluorescent protein alone and fused with a single chain Fv protein,” *J. Biol. Chem.*, vol. 275, no. 23, pp. 17556–17560, 2000.

[63] A. D. Elliott, “Confocal Microscopy: Principles and Modern Practices,” *Curr. Protoc. Cytom.*, vol. 92, no. 1, pp. 1–11, 2020.

[64] M. Gu and C. J. R. Sheppard, “Confocal fluorescent microscopy with a finite-sized circular detector,” *J. Opt. Soc. Am. A*, vol. 9, no. 1, p. 151, 1992.

[65] L. Yu *et al.*, “A Comprehensive Review of Fluorescence Correlation Spectroscopy,” *Front. Phys.*, vol. 9, no. April, pp. 1–21, 2021.

[66] R. Macháň and T. Wohland, “Recent applications of fluorescence correlation spectroscopy in live systems,” *FEBS Lett.*, vol. 588, no. 19, pp. 3571–3584, 2014.

[67] J. R. Lakowicz, *Principles of fluorescence spectroscopy*. 2006.

[68] PicoQuant, "Time-Resolved Fluorescence Wiki." [Online]. Available: https://www.tcspc.com/doku.php/general:fluorescence_correlation_spectroscopy-_a_short_introduction.

[69] V. Buschmann, B. Krämer, F. Koberling, R. Macdonald, and S. Rüttinge, "Quantitative FCS: Determination of the Confocal Volume by FCS and Bead Scanning with the MicroTime 200," *AppNote Quant. FCS*, pp. 1–8, 2007.

[70] S. W. Hell and J. Wichmann, "Breaking the diffraction resolution limit by stimulated emission: stimulated-emission-depletion fluorescence microscopy," *Opt. Lett.*, vol. 19, no. 11, p. 780, 1994.

[71] S. W. Hell, "Microscopy and its focal switch," *Nat. Methods*, vol. 6, no. 1, pp. 24–32, 2009.

[72] G. Vicidomini, P. Bianchini, and A. Diaspro, "STED super-resolved microscopy," *Nat. Methods*, vol. 15, no. 3, pp. 173–182, 2018.

[73] J. Keller, A. Schönle, and S. W. Hell, "Efficient fluorescence inhibition patterns for RESOLFT microscopy," vol. 15, no. 6, pp. 3361–3371, 2007.

[74] T. A. Klar, S. Jakobs, M. Dyba, A. Egner, and S. W. Hell, "Fluorescence microscopy with diffraction resolution barrier broken by stimulated emission," vol. 97, no. 15, 2000.

[75] R. Schmidt, C. A. Wurm, S. Jakobs, J. Engelhardt, A. Egner, and S. W. Hell, "Spherical nanosized focal spot unravels the interior of cells," *Nat. Methods*, vol. 5, no. 6, pp. 539–544, 2008.

[76] G. Donnert *et al.*, "Macromolecular-scale resolution in biological fluorescence microscopy," *Proc. Natl. Acad. Sci. U. S. A.*, vol. 103, no. 31, pp. 11440–11445, 2006.

[77] L. Meyer *et al.*, "Dual-color STED microscopy at 30-nm focal-plane resolution," *Small*, vol. 4, no. 8, pp. 1095–1100, 2008.

[78] H. Blom *et al.*, "Nearest neighbor analysis of dopamine D1 receptors and Na +-K +-ATPases in dendritic spines dissected by STED microscopy," *Microsc. Res. Tech.*, vol. 75, no. 2, pp. 220–228, 2012.

[79] K. I. Willig, B. Harke, R. Medda, and S. W. Hell, "STED microscopy with continuous wave beams," *Nat. Methods*, vol. 4, no. 11, pp. 915–918, 2007.

[80] G. Vicidomini *et al.*, "Sharper low-power STED nanoscopy by time gating," *Nat. Methods*, vol. 8, no. 7, pp. 571–575, 2011.

[81] G. Vicidomini, I. Coto Hernández, M. D'Amora, F. Cella Zanacchi, P. Bianchini, and A. Diaspro, "Gated CW-STED microscopy: A versatile tool for biological nanometer scale investigation," *Methods*, vol. 66, no. 2, pp. 124–130, 2014.

[82] R. Laxminarayan *et al.*, "Antibiotic resistance — the need for global solutions," vol. 13, no. December, 2013.

[83] W. Wang *et al.*, "Antibiotic resistance : a rundown of a global crisis," pp. 1645–1658, 2018.

[84] R. I. Aminov, M. Otto, and A. Sommer, "A brief history of the antibiotic era : lessons learned and challenges for the future," vol. 1, no. December, pp. 1–7, 2010.

[85] M. Wainwright *et al.*, "Photoantimicrobials—are we afraid of the light?," *The Lancet*

Infectious Diseases, vol. 17, no. 2. Lancet Publishing Group, pp. e49–e55, 01-Feb-2017.

[86] A. P. Therapy, "Design of Photosensitizing Agents for Targeted," 2020.

[87] T. Maisch, "Photoantimicrobials — An update," no. December 2019, pp. 1–9, 2020.

[88] E. Polat and K. Kang, "Natural photosensitizers in antimicrobial photodynamic therapy," *Biomedicines*, vol. 9, no. 6, pp. 1–30, 2021.

[89] J. F. Andersen and J. M. C. Ribeiro, "Recognition of Anionic Phospholipid Membranes by and Antihemostatic Protein from a Blood-Feeding Insect," *NIH Public Access*, vol. 43, no. 22, pp. 6987–6994, 2004.

[90] M. Knipp, F. Yang, R. E. Berry, H. Zhang, M. N. Shokhirev, and F. A. Walker, "Spectroscopic and Functional Characterization of Nitrophorin 7 from the Blood-Feeding Insect Rhodnius prolixus Reveals an Important Role of Its Isoform-Specific N-Terminus for Proper Protein Function," *Bone*, vol. 23, no. 1, pp. 1–7, 2007.

[91] J. F. Andersen, N. P. Gudderra, I. M. B. Francischetti, J. G. Valenzuela, and J. M. C. Ribeiro, "Recognition of anionic phospholipid membranes by an antihemostatic protein from a blood-feeding insect," *Biochemistry*, vol. 43, no. 22, pp. 6987–6994, 2004.

[92] M. Hermansson, S. Kjelleberg, T. K. Korhonen, and T. A. Stenström, "Hydrophobic and electrostatic characterization of surface structures of bacteria and its relationship to adhesion to an air-water interface," *Arch. Microbiol.*, vol. 131, no. 4, pp. 308–312, 1982.

[93] F. A. Walker, "Nitric oxide interaction with insect nitrophorins and thoughts on the electron configuration of the {FeNO}6 complex," *J. Inorg. Biochem.*, vol. 99, no. 1, pp. 216–236, 2005.

[94] D. E. Champagne, R. H. Nussenzveig, and J. M. C. Ribeiro, "Purification, partial characterization, and cloning of nitric oxide-carrying heme proteins (nitrophorins) from salivary glands of the blood-sucking insect Rhodnius prolixus," *J. Biol. Chem.*, vol. 270, no. 15, pp. 8691–8695, 1995.

[95] D. A. Kondrashov, S. A. Roberts, A. Weichsel, and W. R. Montfort, "Protein functional cycle viewed at atomic resolution: Conformational change and mobility in nitrophorin 4 as a function of pH and NO binding," *Biochemistry*, vol. 43, no. 43, pp. 13637–13647, 2004.

[96] D. R. Flower, A. C. T. North, and C. E. Sansom, "The lipocalin protein family: Structural and sequence overview," *Biochim. Biophys. Acta - Protein Struct. Mol. Enzymol.*, vol. 1482, no. 1–2, pp. 9–24, 2000.

[97] S. Abbruzzetti *et al.*, "Electrostatic Tuning of the Ligand Binding Mechanism by Glu27 in Nitrophorin 7," *Sci. Rep.*, vol. 8, no. 1, pp. 1–12, 2018.

[98] M. Knipp *et al.*, "Structure and dynamics of the membrane attaching nitric oxide transporter nitrophorin 7," *F1000Research*, vol. 4, no. 0, 2015.

[99] M. Knipp, H. Zhang, R. E. Berry, and F. A. Walker, "Overexpression in Escherichia coli and functional reconstitution of the liposome binding ferriheme protein nitrophorin 7 (NP7) from the blood sucking bug Rhodnius prolixus," *Bone*, vol. 23, no. 1, pp. 1–7, 2008.

[100] A. Allegri, "Structural basis for the reactivity of Nitrophorin 7 with diatomic ligands and its interaction with membranes," 2014.

[101] J. F. Andersen *et al.*, "Kinetics and equilibria in ligand binding by nitrophorins 1-4: Evidence

for stabilization of a nitric oxide-ferriheme complex through a ligand-induced conformational trap," *Biochemistry*, vol. 39, no. 33, pp. 10118–10131, 2000.

[102] A. Pavlou *et al.*, "Probing the ligand recognition and discrimination environment of the globin-coupled oxygen sensor protein YddV by FTIR and time-resolved step-scan FTIR spectroscopy," *Phys. Chem. Chem. Phys.*, vol. 17, no. 26, pp. 17007–17015, 2015.

[103] K. M. Matera *et al.*, "Oxygen and one reducing equivalent are both required for the conversion of α-hydroxyhemin to verdoheme in heme oxygenase," *J. Biol. Chem.*, vol. 271, no. 12, pp. 6618–6624, 1996.

[104] F. Lenci *et al.*, "Spectroscopic and Photoacoustic Studies of Hypericin Embedded in Liposomes As a Photoreceptor Model," *Photochem. Photobiol.*, vol. 62, no. 1, pp. 199–204, 1995.

[105] C. W. Mullineaux, A. Nenninger, N. Ray, and C. Robinson, "Diffusion of green fluorescent protein in three cell environments in Escherichia coli," *J. Bacteriol.*, vol. 188, no. 10, pp. 3442–3448, 2006.

[106] "Dynamic Biosensor," 2021. [Online]. Available: https://www.dynamic-biosensors.com/project/list-of-protein-hydrodynamic-diameters/. [Accessed: 14-Jan-2021].

[107] B. Chen *et al.*, "Targeting negative surface charges of cancer cells by multifunctional nanoprobes," *Theranostics*, vol. 6, no. 11, pp. 1887–1898, 2016.

[108] C. Obermaier, A. Griebel, and R. Westermeier, "Principles of Protein Labeling Techniques," vol. 1295, pp. 1–519, 2015.

[109] C. P. Toseland, "Fluorescent labeling and modification of proteins," *J. Chem. Biol.*, vol. 6, no. 3, pp. 85–95, 2013.

[110] G. T. Hermanson, "Zero-Length Crosslinkers," *Bioconjugate Tech.*, pp. 259–273, 2013.

[111] C. Eisner *et al.*, "Measurement of plasma volume using fluorescent silica-based nanoparticles," *J. Appl. Physiol.*, vol. 112, no. 4, pp. 681–687, 2012.

[112] ATTO-TEC, "ATTO647N." [Online]. Available: https://www.atto-tec.com/ATTO-647N.html?language=en.

[113] K. C. Huang, R. Mukhopadhyay, B. Wen, Z. Gitai, and N. S. Wingreen, "Cell shape and cell-wall organization in Gram-negative bacteria," *Proc. Natl. Acad. Sci. U. S. A.*, vol. 105, no. 49, pp. 19282–19287, 2008.

[114] W. Vollmer, D. Blanot, and M. A. De Pedro, "Peptidoglycan structure and architecture," *FEMS Microbiol. Rev.*, vol. 32, no. 2, pp. 149–167, 2008.

[115] C. Spahn, J. B. Grimm, L. D. Lavis, M. Lampe, and M. Heilemann, "Whole-Cell, 3D, and Multicolor STED Imaging with Exchangeable Fluorophores," *Nano Lett.*, vol. 19, no. 1, pp. 500–505, 2019.

[116] M. Oneto *et al.*, "Nanoscale Distribution of Nuclear Sites by Super-Resolved Image Cross-Correlation Spectroscopy," *Biophys. J.*, vol. 117, no. 11, pp. 2054–2065, 2019.

[117] C. Hally, P. Delcanale, S. Nonell, C. Viappiani, and S. Abbruzzetti, "Photosensitizing proteins for antibacterial photodynamic inactivation," *Transl. Biophotonics*, no. November 2019, pp. 1–11, 2020.

[118] G. T. Hermanson, *Bioconjugate Techniques*. 2008.

[119] M. Zhang, S. Biswas, W. Deng, and H. Yu, "The Crystal Structure of Monovalent Streptavidin," *Nat. Publ. Gr.*, pp. 1–7, 2016.

[120] S. Lee and H. Kim, "Crosslinking of Streptavidin–Biotinylated Bovine Serum Albumin Studied with Fluorescence Correlation Spectroscopy," *Bull. Korean Chem. Soc.*, vol. 42, no. 1, pp. 80–86, 2021.

[121] L. A. Marraffini, A. C. DeDent, and O. Schneewind, "Sortases and the Art of Anchoring Proteins to the Envelopes of Gram-Positive Bacteria," *Microbiol. Mol. Biol. Rev.*, vol. 70, no. 1, pp. 192–221, 2006.

[122] A. C. DeDent, M. McAdow, and O. Schneewind, "Distribution of protein A on the surface of Staphylococcus aureus," *J. Bacteriol.*, vol. 189, no. 12, pp. 4473–4484, 2007.

[123] S. Kwiatkowski *et al.*, "Photodynamic therapy – mechanisms, photosensitizers and combinations," *Biomed. Pharmacother.*, vol. 106, no. June, pp. 1098–1107, 2018.

[124] J. L. Rees, "The melanocortin 1 receptor (MC1R): More than just red hair," *Pigment Cell Res.*, vol. 13, no. 3, pp. 135–140, 2000.

[125] E. M. Wolf Horrell, M. C. Boulanger, and J. A. D'Orazio, "Melanocortin 1 receptor: Structure, function, and regulation," *Front. Genet.*, vol. 7, no. MAY, pp. 1–16, 2016.

[126] M. Singh and K. Mukhopadhyay, "Alpha-melanocyte stimulating hormone: An emerging anti-inflammatory antimicrobial peptide," *Biomed Res. Int.*, vol. 2014, 2014.

[127] W. Siegrist *et al.*, "Characterization of Receptors for α-Melanocyte-stimulating Hormone on Human Melanoma Cells," *Cancer Res.*, vol. 49, no. 22, pp. 6352–6358, 1989.

[128] L. C. Zanetti-Domingues, C. J. Tynan, D. J. Rolfe, D. T. Clarke, and M. Martin-Fernandez, "Hydrophobic Fluorescent Probes Introduce Artifacts into Single Molecule Tracking Experiments Due to Non-Specific Binding," *PLoS One*, vol. 8, no. 9, 2013.

[129] B. L. Sánchez-Laorden, C. Jiménez-Cervantes, and J. C. García-Borrón, "Regulation of human melanocortin 1 receptor signaling and trafficking by Thr-308 and Ser-316 and its alteration in variant alleles associated with red hair and skin cancer," *J. Biol. Chem.*, vol. 282, no. 5, pp. 3241–3251, 2007.

[130] W. Wong and R. F. Minchin, "Binding and internalization of the melanocyte stimulating hormone receptor ligand [Nle4, D-Phe7]α-MSH in B16 melanoma cells," *Int. J. Biochem. Cell Biol.*, vol. 28, no. 11, pp. 1223–1232, 1996.

[131] E. Bekerman and S. Einav, "Combating emerging viral threats," *Physiol. Behav.*, vol. 176, no. 1, pp. 100–106, 2016.

[132] F. Vigant, N. C. Santos, and B. Lee, "Broad-spectrum antivirals against viral fusion," *Nat. Rev. Microbiol.*, vol. 13, no. 7, pp. 426–437, 2015.

[133] F. Vigant *et al.*, "A Mechanistic Paradigm for Broad-Spectrum Antivirals that Target Virus-Cell Fusion," *PLoS Pathog.*, vol. 9, no. 4, 2013.

[134] A. Hollmann, M. A. R. B. Castanho, B. Lee, and N. C. Santos, "Singlet oxygen effects on lipid membranes: Implications for the mechanism of action of broad-spectrum viral fusion inhibitors," *Biochem. J.*, vol. 459, no. 1, pp. 161–170, 2014.

[135] H. Jeong, J. J. Lee, J. Lee, and K. Na, “A Multiligand Architectural Photosensitizer That Targets Hemagglutinin on Envelope of Influenza Virus for Photodynamic Inactivation,” *Small*, vol. 16, no. 20, pp. 1–11, 2020.

[136] J. B. Hudson, I. Lopez-Bazzocchi, and G. H. N. Towers, “Antiviral activities of hypericin,” *Antiviral Res.*, vol. 15, no. 2, pp. 101–112, 1991.

[137] J. B. Hudson, L. Harris, and G. H. N. Towers, “The importance of light in the anti-HIV effect of hypericin,” *Antiviral Res.*, vol. 20, no. 2, pp. 173–178, 1993.

[138] A. Kubin, F. Wierrani, U. Burner, G. Alth, and W. Grunberger, “Hypericin - The Facts About a Controversial Agent,” *Curr. Pharm. Des.*, vol. 11, no. 2, pp. 233–253, 2005.

[139] B. Kiss, D. Mudra, and G. Csík, “Single-particle virology,” pp. 1141–1154, 2020.

[140] M. Arista-Romero, S. Pujals, and L. Albertazzi, “Towards a Quantitative Single Particle Characterization by Super Resolution Microscopy: From Virus Structures to Antivirals Design,” *Front. Bioeng. Biotechnol.*, vol. 9, no. March, pp. 1–17, 2021.

[141] A. Wiehe, J. M. O’brien, and M. O. Senge, “Trends and targets in antiviral phototherapy,” *Photochem. Photobiol. Sci.*, vol. 18, no. 11, pp. 2565–2612, 2019.

[142] C. A. Jiménez-ruiz, D. López-padilla, A. Alonso-arroyo, and R. Aleixandre-benavent, “A systemic review of photodynamic therapy as an antiviral treatment: Potential guidance for dealing with SARS-CoV-2,” *www.archbronconeumol.org Orig.*, no. January, 2020.

[143] N. Kipshidze, N. Yeo, and N. Kipshidze, “Photodynamic therapy for COVID-19,” *Nat. Photonics*, vol. 14, no. 11, pp. 651–652, 2020.

[144] K. Khorsandi, S. Fekrazad, F. Vahdatinia, and A. Farmany, “Nano Antiviral Photodynamic Therapy : a Probable Biophysicochemical Management Modality in Nano Antiviral Photodynamic Therapy : a Probable Biophysicochemical Management Modality in SARS-CoV-2,” *Expert Opin. Drug Deliv.*, vol. 18, no. 2, pp. 265–272, 2021.

[145] A. Almeida, M. A. F. Faustino, and M. G. P. M. S. Neves, “Antimicrobial Photodynamic Therapy in the Control of COVID-19,” pp. 1–10, 2020.

[146] R. Fekrazad, “Photobiomodulation and Antiviral Photodynamic Therapy as a Possible Novel Approach in COVID-19 Management,” *Photobiomodulation, Photomedicine, Laser Surg.*, vol. 38, no. 5, pp. 255–257, 2020.

[147] H. M. Weber, Y. Z. Mehran, A. Orthaber, H. H. Saadat, R. Weber, and M. Wojcik, “Successful Reduction of SARS-CoV-2 Viral Load by Photodynamic Therapy (PDT) Verified by QPCR – A Novel Approach in Treating Patients in Early Infection Stages,” *Med. Clin. Res.*, vol. 2, no. 11, 2020.

[148] S. Law, C. Lo, J. Han, A. W. Leung, and C. Xu, “Photodynamic therapy with curcumin for combating SARS-CoV-2,” *Photodiagnosis Photodyn. Ther.*, vol. 34, no. April, p. 102284, 2021.

[149] P. Delcanale *et al.*, “Subdiffraction localization of a nanostructured photosensitizer in bacterial cells,” *Sci. Rep.*, vol. 5, pp. 1–9, 2015.

[150] O. Vilanova *et al.*, “Understanding the Kinetics of Protein-Nanoparticle Corona Formation,” *ACS Nano*, vol. 10, no. 12, pp. 10842–10850, 2016.

[151] T. Yamazaki, N. Ohta, I. Yamazaki, and P. S. Song, “Excited-state properties of hypericin:

Electronic spectra and fluorescence decay kinetics," *J. Phys. Chem.*, vol. 97, no. 30, pp. 7870–7875, 1993.

[152] T. Andrian, P. Delcanale, S. Pujals, and L. Albertazzi, "Correlating Super-Resolution Microscopy and Transmission Electron Microscopy Reveals Multiparametric Heterogeneity in Nanoparticles," *Nano Lett.*, vol. 21, no. 12, pp. 5360–5368, 2021.

[153] N. D. Weber, B. K. Murray, J. A. North, and S. G. Wood, "The antiviral agent hypericin has in vitro activity against HSV-1 through non-specific association with viral and cellular membranes," *Antivir. Chem. Chemother.*, vol. 5, no. 2, pp. 83–90, 1994.

[154] R. Chaloupka, T. Obšil, J. Plášek, and F. Sureau, "The effect of hypericin and hypocrellin-A on lipid membranes and membrane potential of 3T3 fibroblasts," *Biochim. Biophys. Acta - Biomembr.*, vol. 1418, no. 1, pp. 39–47, 1999.

[155] G. P. Smith, "Kinetics of amine modification of proteins," *Bioconjug. Chem.*, vol. 17, no. 2, pp. 501–506, 2006.

[156] X. F. Zhang, J. Zhang, and L. Liu, "Fluorescence properties of twenty fluorescein derivatives: Lifetime, quantum yield, absorption and emission spectra," *J. Fluoresc.*, vol. 24, no. 3, pp. 819–826, 2014.

Appendix

Chapter 3 – *Nitrophorin 7*

Liposomes

TOCL and POPC (both purchased from Avanti Polar Lipids) used for FCS measurements in Figure *3.5*, Figure 3.10, Figure 3.11 and imaging in Figure 3.13, Figure 3.14, Figure 3.17 and Figure 3.18 liposomes were prepared according to the injection method. DLPC (4mg/mL) dissolved in ethanol (500 µL) was slowly injected into 5 mL of PBS phosphate buffer, pH 7. The solution was kept at 50°C and magnetically stirred. In Figure 3.5, liposomes where then exposed to Hyp (50 nM) or the complex apoNP7-Hyp previously assembled (50 nM, refer to Hyp concentration), incubated at RT for ~ 10 min and used to perform FCS measurements (a volume of 50 µl for each solution was used). In Figure 3.10 and Figure 3.11, liposomes were exposed to NP7-ATTO647N and incubated for 30 min at RT and subsequently used to perform FCS measurements at different concentrations (50, 100, 200 nM) of the compound, where ATTO647N ε(646 nm) = 150000 M^{-1} cm^{-1} was used to measure the concentration. NP7 concentration was measured using heme extinction coefficient ε(403 nm) = 81000 M^{-1} cm^{-1}.

Labeling NP7 with ATTO647N-cadaverine

Main guidelines for the procedure were taken from [110]. A solution of ATTO647N-cadaverine (from Atto-Tech) at 75 µM in DMSO was inserted in a solution containing NP7 at a concentration of 15 µM (the protein was kept in MES buffer 0.1 M at pH 5.5). Thereafter, EDC (from Sigma-Aldrich/Merck) at a concentration of 150 µM was added to the solution containing NP7 and ATTO647N-cadaverine (the ratio between the three compounds should be 1:5:10, NP7:ATTO647N-cadaverine-EDC). The solution so prepared was incubated for 2 hours at 4°C mild agitation. After this incubation time, PD Minitrap™ G-25 from Cytiva (Marlborough, MA, USA), were used to collect the labelled protein. The assessment of the effective labeling was tested via fluorescence anisotropy measurements. The protocol allowed to have 1 molecule of ATTO647N (6 µM) every 2 NP7 proteins (13 µM), for a 1:2 ratio.

E. coli for imaging

Vegetative *E.coli* DH5α cells were grown in 5 ml of sterile LB Broth at 37°C, overnight. A volume of 1 ml of this cell suspension was then washed 4 times in

PBS buffer by means of centrifugation (10 minutes at 4000 rpm) and suspended again. *S. aureus* washed cells were subsequently diluted 6 times in a final volume of 1 ml. For microscopy measurements in Figure 3.15, a dilution of 1:6 was used to perform FCS measurements and FCS. In FCS experiments of Figure 3.12, *E.coli* cells were exposed to NP-ATTO647N 200 nM and incubated RT for 1 hour. 40 µl of the so prepared solution were then used.

Fluorescence Correlation Spectroscopy (FCS)

FCS experiments were performed using a Microtime 200 system from PicoQuant, based on an inverted confocal microscope (Olympus IX71) and equipped with two SPADs (Single Photon Avalanche Diodes) used in the cross-correlation mode. Excitation was achieved by a 475 nm (Hyp) or a 635 nm (ATTO647N) picosecond diode laser operated at 20 MHz. Fluorescence emission by Hyp was collected through a bandpass filter (555/20 nm) and split with a 50/50 splitter between the two detection channels. Fluorescence from ATTO647N was collected through a bandpass filter (670/20 nm).

Confocal Microscopy and STED nanoscopy

Imaging experiments of Figure 3.13 and Figure 3.14 were performed on a Leica TCS SP5 gated-CW-STED microscope, using a HCX PL APO 100x 100/1.40/0.70 oil immersion objective lens (Leica Microsystems, Mannheim, Germany). Emission depletion of ATTO647N was accomplished with a coupled pulsed STED laser at 775 nm (Onfive Katana Pulsed Laser). Excitation was provided by a white laser at the desired wavelength for each sample. ATTO647N was excited at 640 nm and its fluorescence emission detected at 650-710 nm, using a hybrid detector (Leica Microsystem). Hyp was excited at 560 nm and detected at 570-610 nm, again using a hybrid detector. Sequential scanning mode was used for Figure 3.14. In both cases, 1024 x 1024 pixel images were acquired with a pixel size of 25 nm, with a 16 scans average per pixel line.

Images in Figure 3.15, Figure 3.17 and Figure 3.18 were acquired on a Leica Stellaris 8 Tau-STED microscope, using an HC PL APO CS2 100x/1.40 oil immersion objective lens (Leica Microsystem, Mannheim, Germany). Emission depletion was accomplished with a 775 nm STED laser. Excitation was provided by a white laser at the desired wavelength for each sample. For Figure 3.15, *E.coli cells* were seeded on a coverslip previously treated with poly-L-lysine and imaged using a 18 imaging chamber (total volume 200 µl). Nile Red was excited at 561 nm and emission detected at 570-610 nm. NP7-ATTO647N was subsequently added to the

bacterial cells in the imaging chamber and excited at 640 nm. The fluorescence was collected at 650-700 nm. In both cases, fluorescence was collected using an hybrid detector (Leica Microsystem). 1024 x 1024 were acquired with a pixel size of 20 nm. Same imaging conditions were used for Figure 3.17 and Figure 3.18.

Chapter 4 – Streptavidin-based delivery systems

IgG from normal human serum, streptavidin (SAV) from *Streptomyces avidinii* (salt-free, lyophilized powde)r, see Figure 4.1a for the three-dimensional structure of the complex between the tetramer and biotin, PDB code 3wyp), and Eosin 5-isothiocyanate were from Sigma-Aldrich. The Biotin Protein Labeling Kit was from Biotium, Inc. (Fremont, CA, USA). Biotinylated STAR635 and STAR635 labelled streptavidin were from Abberior GmbH (Göttingen, Germany). Strep labelled with Chromeo488 was from Active Motif, Inc.

Concentrations were estimated from the molar extinction coefficients of the compounds: ε(280 nm) = 41,326 M^{-1} cm^{-1} for streptavidin monomers, ε(538 nm) = 95,000 $cm^{-1}M^{-1}$ and ε(280 nm) = 26,766 $cm^{-1}M^{-1}$ for EITC (in DMSO), and ε(280 nm) = 210,000 $cm^{-1}M^{-1}$ for IgG. The SAV concentration in EITC-strep complexes was estimated from the absorbance at 280 nm after correcting for the EITC contribution at this wavelength. It is assumed that the molar extinction coefficient of the visible absorption band of EITC is not affected by binding to strep.

PD Minitrap™ G-25 were from Cytiva (Marlborough, MA, USA).

IgG biotinylation

Biotinylation of IgG was performed using a biotin protein labeling kit based on a succinimidyl ester biotin derivative [155] (Biotin SE Protein Labeling Kit, Biotium, Inc., Fremont, CA, USA). The overall yield in protein after purification exceeded 50%.

EITC-streptavidin conjugate

The conjugate between EITC and strep was prepared using a standard protocol. EITC was dissolved in DMSO at 9 mM. The concentrated EITC solution in DMSO (125 μL) was added to a 100 μM (monomer concentration) strep solution (1 mL) in 0.1 M sodium carbonate buffer (pH > 9) or in PBS (pH < 9) to a final EITC concentration of 900 μM. The solution was stirred at 4°C overnight. The protein conjugate was purified using a Sephadex G25, PD-10 column, equilibrated with PBS buffer at pH = 7.4.

Each strep monomer contains 4 potential reaction sites for EITC (Lys80, Lys121, Lys132 and the N terminal) (residues displayed as blue sticks in Figure 4.1a) The labeling reaction was performed at pH values between 7.5 and 10.5, obtaining the highest yield for the most alkaline conditions.

Photoinactivation of S. aureus suspensions

Vegetative *S. aureus* ATCC 25923 cells were grown in sterile Tryptic Soy Broth at 37 °C until an optical density of 0.4 at 600 nm, corresponding to an initial concentration of bacteria of 10^7 CFU/mL. Cell suspensions were then washed three times in PBS by means of centrifugation and resuspension. In one type of experiment, cells were first incubated in the dark with the biotinylated IgG at 100 nM for 30 min at room temperature, then incubated for 30 more minutes with EITC-strep (at strep tetramer concentrations of 0.125, 0.25, 0.5, and 1 μM). In a control experiment, cells were incubated for 30 minutes with EITC-strep (at strep tetramer concentrations of 0.125, 0.25, 0.5, and 1 μM), in the absence of the antibody.

Photoinactivation experiments were performed as previously described. Suspensions were placed in 96-wells plates and irradiated with green light using a LED light source (SORISA Photocare) for which the green output at 521±19 nm (27.5 mW/cm^2) was selected.

Irradiation was performed for 12, 24, or 60 min (corresponding to light fluences of 10, 20 and 50 J/cm^2, respectively). Suspensions were then serially diluted until 10^{-6} times the original concentration and then plated on Tryptic Soy agar plates. Colony forming units (CFUs) were counted after 24 h incubation in the dark at 37 °C to calculate the survival fraction. Three independent assays were conducted, with 6 replicates within each assay. Survival fractions are expressed as means ± standard deviation.

Spectroscopy

Absorption spectra were collected using a Jasco V-650 (Jasco Europe) spectrophotometer. Steady state fluorescence excitation, emission and anisotropy spectra were measured with a SF5 spectrofluorometer (Edinburgh Instruments Ltd., Livingston, UK). Fluorescence decays were recorded by a FLS920 time-correlated single photon counting system (TCSPC) (Edinburgh Instruments Ltd., Livingston, UK) with pulsed LED excitation at 500 or 600 nm, operated at 5 MHz repetition rate. The quality of the fitting was evaluated through the value of

the reduced χ^2 (~1.0-1.5) and visual inspection of residuals and the autocorrelation of residuals.

Fluorescence quantum yields were determined with a comparative method [67] using Eosin in aqueous solution as a reference compound (Φ_F = 0.24) [156].

All experiments were performed at 20 °C.

Fluorescence Correlation Spectroscopy (FCS)

FCS experiments were performed using a Microtime 200 system from PicoQuant, based on an inverted confocal microscope (Olympus IX71) and equipped with two SPADs (Single Photon Avalanche Diodes) used in the cross-correlation mode. Excitation was achieved by a 475 nm or a 635 nm picosecond diode laser operated at 20 MHz. Fluorescence emission by EITC-strep was collected through a bandpass filter (555/20 nm) and split with a 50/50 splitter between the two detection channels. Fluorescence from STAR635 was collected through a bandpass filter (670/20 nm).

Sample preparation for imaging

Vegetative *S. aureus* ATCC 25923 cells were grown in 5 ml of sterile LB Broth at 37°C, overnight. A volume of 1 ml of this cell suspension was then washed 4 times in PBS buffer by means of centrifugation (10 minutes at 4000 rpm) and suspended again. *S. aureus* washed cells were subsequently diluted 6 times in a final volume of 1 ml. A sample in a final volume of 500 µl of bacteria cells was prepared with 0.5 µM concentration of IgG, undergoing an incubation time of 30 min at 37°C and a 10 min centrifugation cycle at 4000 rpm. Supernatant was discarded and bacteria cells were suspended in 500 µl of PBS buffer with a 1 µM concentration of Chromeo488-Strep, followed by an incubation time of 30 min at 37°C and a 10 min centrifugation cycle at 4000 rpm. Supernatant was discarded and bacteria cells suspended in 500 µl of PBS buffer. Imaging measurements were performed using a live-cell imaging culture chamber (compatible with 18 mm round coverslips). 18 mm coverslips were prepared with poly-D-lysine and subsequently used after a PBS buffer wash. The prepared bacteria cells stock of 500 µl was diluted 10 times in the imaging chamber, where 30 µl of the stock solution were added to 270 µl of PBS buffer for a total volume of 300 µl.

Confocal Microscopy and STED nanoscopy on S.aureus

Images in Figure 4.6 and Figure 4.7 were acquired on a Leica TCS SP5 gated-STED microscope, using an HCX PL APO 100x 100/1.40/0.70 oil immersion objective lens (Leica Microsystems, Mannheim, Germany). Emission depletion was accomplished with a 592 nm STED laser. Excitation was provided by a white laser at the desired wavelength for each sample. SAV-Chromeo488 was excited at 488 nm and it fluorescence emission was detected at 495-550 nm, with 1.5 -10 ns time gating using a hybrid detector (Leica Microsystem). Filters used were a notch filter 488/561/633 and one 594 nm. 512 x 512 pixel images were acquired with a pixel size of 25 nm. The STED image was acquired with 96 scans average per pixel.

Melanoma Cell Culture

A375 human malignant melanoma cells were purchased from Sigma Aldrich/Merck). Cells were grown in DMEM and supplemented with 1% antibiotic solution, 1% glutamine, and 10% FBS. Medium and supplements were purchased from Thermo Fisher. The cell line was maintained in a humidified atmosphere of 95% air, 5% CO_2 at 37 °C.

Streptavidin-FITC from *Streptomyces avidinii* (salt-free, lyophilized powder), [Nle^4, $DPhe^7$]-Biotinyl-α MSH and [$D\text{-}Phe^7$]-α MSH were purchased from Sigma Aldrich/Merck. SAV-FITC and hormones were dissolved in PBS buffer pH = 7.4. For imaging experiments, cells were seeded on a 18 mm coverslip subsequently mounted in a microscope chamber with suitable size. Cells were then covered with 200 µl of Live Cell Imaging solution. In Figure 4.8, cells were incubated with biot-α-MSH at 4 µM for 30 minutes at 37°C. Then, cells were exposed to 1 µM of SAV-FITC for ~ 10 min. The imaging solution was then removed from the chamber and substitute with fresh Live Cell Imaging solution for reducing fluorescence background signal. The same preparation was done for cells in Figure 4.9, but the α-MSH was not biotinylated in this case. In Figure 4.10, cells were incubated with 1 µM SAV-FITC for 30 min. The imaging solution was then removed and replaced with fresh Live Cell Imaging. Eventually, for Figure 4.12 the SAV-FITC complex with biot-α-MSH was assembled before in PBS buffer pH = 7.4 in a solution of 500 µl with 5 µM biot-α-MSH and 1 µM SAV-FITC. The complex was subsequently administered to the cells kept in incubation for 10 min a 37°C and subsequently imaged.

Chapter 5 – Hyp as an antiviral treatment

Hypericin was obtained from HWI pharma services GmbH, and dissolved in DMSO to obtain a concentrated stock solution. Concentration was measured spectroscopically. Syto 13 was obtained from ThermoFisher Scientific and dissolved in PBS buffer pH = 7.4 to obtain a stock solution (250 nM). All samples were store in the dark and used fresh.

Microscopy

Co-localization (Figure 5.1d-f) and single particle intensity (Figure 5.4) measurements were obtained with a Nikon TiE inverted confocal microscope equipped with three excitation lasers (405, 488, 561 nm) and three alkaline PMTs. Hyp and Syto13 were excited at 561 and 488 nm, respectively. The 561 nm laser was a CW diode pump solid-state laser (Melles Griot) while the 488 nm laser was a CW diode semiconductor laser (Coherent). Fluorescence emission was collected through two bandpass filters (Hyp, 605/70 nm and Syto13, 515/30 nm). STED nanoscopy (Figure 5.1) was performed using the Leica Mycrosystems STELLARIS 8 STED equipped with a supercontinuum White Light Laser (WLL) where 561 nm excitation wavelength was selected by an AOBS. The depletion wavelength was 775 nm.

FCS

FCS experiments were performed using a Microtime 200 system from PicoQuant, based on an inverted confocal microscope (Olympus IX71) and equipped with two SPADs (Single Photon Avalanche Diodes) used in cross-correlation mode. Hyp excitation was achieved by a 475 nm picosecond diode laser operated at 20 MHz. Fluorescence emission was collected through a bandpass filter (675/25 nm) and split with a 50/50 splitter between the two detection channels. The setup allowed the simultaneous acquisitions of correlation curves and time-resolved fluorescence decays, measured by time-correlated single photon counting (TCSPC).

Spectroscopy

Absorption spectra were collected using a Jasco V-650 (Jasco Europe) spectrophotometer. Steady state fluorescence excitation, emission and anisotropy spectra were measured with the SF5 spectrofluorometer (Edinburgh

Instruments Ltd., Livingston, UK). The instrument is equipped with excitation and emission polarizers, enabling fluorescence anisotropy detection.

Sample preparation for fluorescence spectroscopy, FCS and lifetimes

The stock suspension of fixed viral particles was preliminary centrifuged (3 min, 5000 rpm) to remove the largest aggregates. Viral particles were then diluted 50 times in PBS buffer pH = 7.4 and a small volume of concentrated Hyp in DMSO (50x the desired final concentration) was added. The final concentration of DMSO was 2%. After incubation of 5 min at room temperature in the dark, the solution (50 µL) was placed in the fluorometer using a quartz cuvette (l = 0.3 cm). Emission spectra (Figure 5.2b) were acquired collecting the emission at 650 nm. Directly after, ~40 µL of the same solution were placed on the FCS system for the simultaneous measurement of correlation curves (Figure 5.2a) and time-resolved fluorescence (Figure 5.3), with an acquisition time of 5 min, and 3-5 repetitions for each sample All samples were prepared in the same way and measured under the same conditions. The fitting of measured correlation curves and fluorescence decays was performed with the SymphoTime software from PicoQuant.

DLP liposomes were prepared according to the injection method. DLPC (7mg/mL) dissolved in ethanol (700 µL) was slowly injected into 10 mL of a 10 mL phosphate buffer, pH 7. The solution was kept at 30°C and magnetically stirred. Liposomes were exposed to Hyp as described above for viral particles and were placed on the FCS system for measurement of time-resolved fluorescence Figure 5.3.

Imaging

The stock solution of fixed viral particles was preliminary centrifuged (3 min, 5000 rpm) to remove the largest aggregates and viral particles were diluted 50 times in PBS buffer pH = 7.4.

For single particle intensity measurements (Figure 5.4), pre-diluted viral particles were mixed with Hyp (concentrations: 5, 10, 20, 30, 40, 50, 70, 90 nM) and 20 µL of each solution were seeded on a sterile cell culture dish with glass bottom. After 10 min incubation, 100 µL of PBS were were added, without intermediate washing, to reach the optimal volume for imaging, that allows complete and homogeneous coverage of glass without the solution. The sample was finally sealed to avoid evaporation and imaged immediately. The very same procedure was followed for all the solutions to enable comparison.

For co-localization measurements (Figure 5.1d-f), pre-diluted viral particles were mixed with Hyp (final concentration: 50 nM), seeded on a sterile cell culture dish and subsequently mixed with Syto13 (final concentration: 50 nM). The sample was then imaged immediately without intermediate washings. A sequential scanning mode was used to exclude bleed-through during the acquisition procedure. In all the samples, the final concentration of DMSO is negligible (<2%).

Single particle intensity analysis

Single particle intensity data of Figure 5.4 were acquired using the same parameters: 1024 x 1024 image size, pixel dwell time 6.2 µs, pixel size 80 nm, line average x4; and with a comparable axial position of the focal plane. Acquired images (8-10 for each sample) were analyzed using ImageJ. First, a Gaussian filter (σ = 180 nm) was applied to reduce uncorrelated background noise and better discriminate the fluorescent particles. In a few cases, parts of the images that resulted clearly out of focus, e.g. due to irregularities of the glass surface, were excluded. Then, a particle analyzer tool was applied to automatically recognize particles having minimum intensity above a threshold value (400-420 a.u.) and a minimum area (8-10 pixels). Results of the analysis were visually inspected and a few particles (<1%) showing unrealistic features, e.g. corresponding to aggregates, were excluded. Finally, the mean intensity values of each selected particle were stored and used to reconstruct distributions.